THE SOLAR NEIGHBORHOOD. XXXVII. THE MASS–LUMINOSITY RELATION FOR MAIN-SEQUENCE M DWARFS*

G. F. BENEDICT[1], T. J. HENRY[2,10], O. G. FRANZ[3], B. E. MCARTHUR[1], L. H. WASSERMAN[3], WEI-CHUN JAO[4,10],
P. A. CARGILE[5], S. B. DIETERICH[6,10], A. J. BRADLEY[7], E. P. NELAN[8], AND A. L. WHIPPLE[9]

[1] McDonald Observatory, University of Texas, Austin, TX 78712, USA
[2] RECONS Institute, Chambersburg, PA 17201, USA
[3] Lowell Observatory, 1400 West Mars Hill Road, Flagstaff, AZ 86001, USA
[4] Dept. of Physics & Astronomy, Georgia State University, Atlanta GA 30302, USA
[5] Harvard-Smithsonian Center for Astrophysics, 60 Garden Street, Cambridge, MA 02138, USA
[6] NSF Astronomy and Astrophysics Postdoctoral Fellow, Carnegie Institiution of Washington, Washington, DC 20005, USA
[7] Spacecraft System Engineering Services, P.O. Box 91, Annapolis Junction, MD 20701, USA
[8] Space Telescope Science Institute, 3700 San Martin Drive, Baltimore, MD 21218, USA
[9] Conceptual Analytics, LLC, Greenbelt, MD 20771, USA

ABSTRACT

We present a mass–luminosity relation (MLR) for red dwarfs spanning a range of masses from $0.62\,\mathcal{M}_\odot$ to the end of the stellar main sequence at $0.08\,\mathcal{M}_\odot$. The relation is based on 47 stars for which dynamical masses have been determined, primarily using astrometric data from Fine Guidance Sensors (FGS) 3 and 1r, white-light interferometers on the *Hubble Space Telescope (HST)*, and radial velocity data from McDonald Observatory. For our *HST*/FGS sample of 15 binaries, component mass errors range from 0.4% to 4.0% with a median error of 1.8%. With these and masses from other sources, we construct a *V*-band MLR for the lower main sequence with 47 stars and a *K*-band MLR with 45 stars with fit residuals half of those of the *V* band. We use GJ 831 AB as an example, obtaining an absolute trigonometric parallax, $\pi_{abs} = 125.3 \pm 0.3$ mas, with orbital elements yielding $\mathcal{M}_A = 0.270 \pm 0.004\,\mathcal{M}_\odot$ and $\mathcal{M}_B = 0.145 \pm 0.002\,\mathcal{M}_\odot$. The mass precision rivals that derived for eclipsing binaries. A remaining major task is the interpretation of the intrinsic cosmic scatter in the observed MLR for low-mass stars in terms of physical effects. In the meantime, useful mass values can be estimated from the MLR for the ubiquitous red dwarfs that account for 75% of all stars, with applications ranging from the characterization of exoplanet host stars to the contribution of red dwarfs to the mass of the universe.

Key words: astrometry – binaries: close – stars: distances – stars: late-type – techniques: interferometric – techniques: radial velocities

Supporting material: machine-readable tables

1. INTRODUCTION

With the exception of the Hertzsprung–Russell (HR) diagram, the main-sequence mass–luminosity relation (MLR) is perhaps the single most important "map" of stellar astronomy because the entire evolution of an individual star depends on its mass. The MLR allows astronomers to convert a *relatively* easily observed quantity, luminosity, to a more revealing characteristic, mass, providing a better understanding of the object's nature. When considering populations of stars, an accurate MLR permits luminosity functions to be converted into mass functions and drives estimates of the stellar contribution to the mass of the Galaxy.

Basic observations of stars include measurements of apparent magnitudes, colors, surface temperatures (T_{eff}), and metallicities. From these attributes we can derive luminosities and radii, given combinations of distance measurements or directly measured angular sizes from long-baseline interferometry. Yet the crucial masses remain elusive, typically only measured dynamically in binary systems. Thus, when stellar

modelers compare their theoretical results with real stars to test the accuracy of their efforts, they often assume masses for their test stars. For example, at a mass of $0.3\,\mathcal{M}_\odot$, models from Allard et al. (2000), Baraffe et al. (2015), and Dotter (2016) predict M_V values of 11.42, 11.61, and 11.25, respectively. An accurate MLR allows choices to be made between various modeling approaches, such as the treatment of stellar ages, convection, turbulent mixing, rotation, magnetic activity, and mass loss (Andersen 1991). Furthermore, the need for accurate mass estimates for the smallest stars has come to the forefront with the discovery of exoplanets associated with M dwarf stars (see Lurie et al. 2014 for a recent list of the nearest M dwarfs with planets). More accurate estimates of host-star masses translate directly into more reliable companion-planet masses and, consequently, more accurate bulk compositions for planets that transit.

The first robust MLR for M dwarf stars was reported in Henry & McCarthy (1993), who provided relations at *VJHK* for 37 stars, of which 26 had masses less than $0.6\,\mathcal{M}_\odot$. Early results from the project described here can be found in Henry et al. (1999), where an improved MLR at *V* was pivotal. A modest update was presented in Delfosse et al. (2000), which included many of the same stars. Torres et al. (2010) summarized the entire stellar MLR using eclipsing systems as of a few years ago, outlining how few M dwarf stars have accurate masses because these tiny stars rarely eclipse.

Table 1
Identifications and Coordinates[a]

ID	Giclas	HIP	LHS	Other	R.A.	Decl.
GJ 1005 AB	266-076	1242	1047	L722-22	00 15 27.994	−16 08 01.83
GJ 22 AC	⋯	⋯	⋯	ADS 433	00 32 29.586	+67 14 03.65
GJ 54 AB	⋯	5496	1208	L87-59	01 10 22.903	−67 26 41.85
GJ 65 AB	272-061	⋯	⋯	L726-8	01 39 01.453	−17 57 02.05
GJ 1081 AB	096-045	⋯	⋯	LTT 17822	05 33 19.151	+44 48 57.71
GJ 234 AB	106-049	30920	⋯	Ross 614	06 29 23.404	−02 48 50.37
G 250-029 AB	⋯	33142	221	GJ 3412	06 54 04.237	+60 52 18.36
G 193-027 AB	⋯	⋯	224	GJ 3421	07 03 55.655	+52 42 07.60
GJ 469 AB	012-038	60910	2565	Wolf 414	12 28 57.486	+08 25 31.26
GJ 473 AB	012-043	⋯	333	Wolf 424	12 33 17.383	+09 01 15.77
GJ 623 AB	202-045	80346	417	⋯	16 24 09.325	+48 21 10.46
GJ 748 AB	022-018	94349	472	Wolf 1062	19 12 14.676	+02 53 10.71
GJ 1245 AC	208-044	⋯	3494	V1581 Cyg	19 53 54.469	+44 24 53.09
GJ 791.2 AB	144-008	⋯	3556	HU Del	20 29 48.385	+09 41 20.36
GJ 831 AB	026-007	106255	511	Wolf 922	21 31 18.643	−09 47 26.41

Note.

[a] HIP—*Hipparcos*, LHS—Luyten Half Second. R.A., Decl. epoch 2000.0.

Here we present astrometry from the *Hubble Space Telescope (HST)* and other sources, in combination with ground-based radial velocities (RVs), to improve the low-mass region of the MLR that is complicated by age, metallicity, and magnetic effects. This is the realm of the red dwarfs, typically of spectral type M, that slowly descend to the main sequence along a nearly vertical Hayashi track in the HR diagram (Palla 2012). This results in an M dwarf population that in the solar neighborhood spans a wide range of ages (Riedel et al. 2014). In addition, M dwarf luminosities are affected by composition (metallicity), which is a function of the mixing of the interstellar medium (with sources internal and external to the Galaxy), star-formation rate, and birth date within the Galaxy (e.g., Sneden et al. 2002). To complicate matters even further, a more poorly understood factor affecting M dwarf luminosity is magnetism, which induces short- and long-term photometric variability (Hosey et al. 2015).

In this paper, we model *HST* Fine Guidance Sensor (FGS) astrometric, and, if available, RV measurements simultaneously to obtain parallaxes, proper motions, orbits, and component masses for 15 systems containing 30 M dwarfs (Table 1). Our resulting masses have a median precision of 1.8%, which constitutes a significant advance from previous efforts. The derived parallaxes, which take into account the orbital motions of the binaries, are usually marked improvements—typically by factors of 5–10 over available parallaxes in the Yale Parallax Catalog (van Altena et al. 1995, hereafter YPC) and *Hipparcos* (van Leeuwen et al. 2007)—and are key in deriving the high-accuracy masses. We derive the first masses for stars in six systems, improve masses over previous efforts by others for seven systems, and improve upon our own *HST* efforts for two systems: GJ 748 AB in Benedict et al. (2001) and GJ 791.2 AB in Benedict et al. (2000). Our reductions and analyses for the latter two systems include a few new *HST*/FGS measurements and have improved RV measurements, yielding more precise masses.

In Sections 2 and 3 we describe the various sources of astrometric and RV data that were used in our modeling. In Section 4 we discuss in detail the data and modeling process for GJ 831 AB, as an example of our technique to obtain masses. Section 5 summarizes modeling notes and resulting masses for

the other 14 systems. In Section 6 we describe the measurements for the M_V and M_K values used to create the MLRs. Section 7 describes additional systems in which red dwarfs with high-quality masses are available for use in the MLRs. In Section 8 we construct a V-band MLR from the set of 47 stars and a K-band MLR using 45 stars. We discuss our results in Section 9 and conclude with a summary in Section 10.

2. ASTROMETRIC DATA

2.1. HST FGSs

An *HST* FGS provides two types of astrometric data. Like all interferometers, an FGS produces a fringe that we interrogate either by tracking the fringe position (POS mode) or by scanning to build up a fringe image (TRANS mode). TRANS mode yields the structure of the fringe from which it is possible to derive the separation and position angle of a secondary relative to a primary in a binary system, essential in establishing the relative orbit. POS mode permits the measurement of the position of the primary star (brighter component) relative to a local frame of reference stars, essential for determining proper motion, parallax, and mass fraction. Franz et al. (1998) and Benedict et al. (2011) contain details of *HST* FGS's TRANS- and POS-mode reduction and analysis, respectively. Detectability and measurement precisions for a given binary star's components critically depend on star brightnesses, component brightness differences, and the binary angular separation. All *HST*/FGS astrometry also depends on the Optical Field Angle Distortion (OFAD) calibration (McArthur et al. 2002). This calibration reduces as-built *HST* telescope and FGS distortions with magnitude ∼1″ to below 2 mas over much of the FGS field of regard. The present work benefits from a POS mode OFAD revision more recent (2012) than reported in McArthur et al. (2006). The 15 red dwarf systems targeted in this program and discussed in the following sections rely on *HST* TRANS- or POS-mode measurements and are listed in Tables 1 and 2.

For binary stars, the FGS transforms images of the two components into two overlapping fringes, sometimes called the "S curves." For perfect fringes and component separations greater than the resolution of *HST* at $\lambda = 580$ nm, about 40 mas, the presence of a companion should have little effect

Table 2
System Spectral Types and Photometry

ID	Sp.T.[a]	U	B	ref[b]	V	R	I	ref[b]	J[c]	H[c]	K[c]
GJ 1005 AB	M3.5V	14.49	13.19	K07	11.48	10.27	8.70	*	7.22	6.71	6.39
GJ 22 AC	M1.5V	...	11.88	W96	10.28	9.24	7.97	W96	6.84	6.27	6.04
GJ 54 AB	M2.5V	12.51	11.36	K07	9.82	8.70	7.32	*	6.00	5.41	5.13
GJ 65 AB	M5.0V	...	13.95	B90	12.06	10.40	8.34	*	6.28	5.69	5.34
GJ 1081 AB	M3.0V	14.99	13.79	D88	12.21	11.06	9.58	W84	8.20	7.59	7.34
GJ 234 AB	M4.0V	13.94	12.76	K07	11.14	9.78	8.04	*	6.38	5.75	5.49
G 250-029 AB	M2.5V	...	12.51	W96	10.95	9.86	8.48	W96	7.13	6.60	6.35
G 193-027 AB	M5.0V	...	15.14	D82	13.29	11.94	10.15	W96	8.54	8.09	7.78
GJ 469 AB	M3.0V	14.83	13.62	K10	12.05	10.85	9.30	*	7.84	7.20	6.96
GJ 473 AB	M5.0V	...	14.33	B90	12.47	10.90	8.92	*	7.00	6.40	6.04
GJ 623 AB	M2.0V	...	11.78	W96	10.28	9.25	7.95	W96	6.64	6.14	5.92
GJ 748 AB	M3.0V	13.72	12.66	K10	11.10	9.95	8.47	*	7.09	6.57	6.29
GJ 1245 AC	M5.0V	...	...	...	13.41	11.81	9.78	W96	7.79	7.19	6.85
GJ 791.2 AB	M4.5V	...	14.76	B90	13.13	11.73	9.97	*	8.23	7.67	7.31
GJ 831 AB	M4.0V	14.91	13.68	K10	12.02	10.70	9.00	*	7.32	6.70	6.38

Notes.
[a] Spectral type for combined flux, except for GJ 65 AB, which is for primary only.
[b] References for *UB* photometry and *VRI* photometry: *—this paper, B90—Bessell (1990), D82—Dahn et al. (1982), D88—Dahn et al. (1988), K07—Kilkenny et al. (2007), K10—Koen et al. (2010), W84—Weis (1984), W96—Weis (1996).
[c] From the Two Micron All Sky Survey (2MASS).

on the component-A position obtained from the fringe-zero crossing. For separations smaller than 40 mas, the measurement of the position of the brighter component of a blended image will be biased toward the fainter component (van de Kamp 1967), possibly requiring a photocenter correction. Because an FGS has two orthogonal axes, the separation along each interferometer axis, not the total separation on the sky, determines the photocenter correction. For any arbitrary *HST* orientation, components A and B can have separations along the FGS axes from 0.0 mas to the actual full separation.

During this project we observed with two FGS units: FGS 3 from 1992 to 2000, and FGS 1r from 2000 to 2009. FGS 1r replaced the original FGS 1 during *HST* Servicing Mission 3A in late 1999. Our original analysis of GJ 748 AB (Benedict et al. 2001) incorporated POS-mode photocenter corrections, as does the present reanalysis. These corrections, ranging from −3.2 to +2.3 mas, are for the FGS 3 *X* axis a complicated function of separation because FGS 3 delivered far from perfect fringes with substantial instrumental structure (Franz et al. 1991). FGS 1r produces higher-quality fringes (Nelan 2012), and corrections are similar along both axes and similar in size to the *Y*-axis correction seen in Benedict et al. (2001) for GJ 748 AB. These corrections (typically a maximum of 2 mas) are negligible for systems with component $\Delta V \geqslant 2.3$ (ΔV values listed in Table 10). The systems with $\Delta V \leqslant 2.3$ and typically smaller separations are GJ 469 AB, GJ 748 AB, GJ 831 AB, GJ 1081 AB, and G 250-029 AB. Generally, only a few measurements require photocenter corrections.

2.2. Additional Astrometry Measurements

2.2.1. Traditional Ground-based Methods

We included visual, photographic, and CCD observations of separations and position angles from Geyer et al. (1988) for our analysis of GJ 65 AB (Section 5.13). These (relative to *HST*) low-precision measurements are primarily from the USNO 61 in reflector and stretch to nearly twice the full period of

GJ 65 AB, proving extremely useful for this long-orbital-period system.

2.2.2. Adaptive Optics

We include a single observation of G 193-027 AB from Beuzit et al. (2004), who used the Adaptive Optics Bonnette system on the Canada–France–Hawaii Telescope (CFHT). For GJ 65 AB we include five VLT/NACO measures of position angle and separation (Kervella et al. 2016).

2.2.3. Aperture Masking Interferometry

For our analysis of GJ 623 AB (Section 5.4), we included astrometric observations (Martinache et al. 2007) performed with the PHARO instrument on the Palomar 200 in (5 m) telescope and with the NIRC2 instrument on the Keck II telescope. Separations have typical errors of 2 mas. Position angle errors average 0°.5.

2.2.4. Speckle Interferometry

Measurements are included for GJ 22 AC from McCarthy et al. (1991) and for GJ 473 AB from Henry et al. (1992) and Torres et al. (1999), who used a two-dimensional infrared speckle camera containing a 58×62 pixel InSb array on the Steward Observatory 90 in telescope. We also include infrared speckle observations by Woitas et al. (2003), who obtained fourteen separation and position angle measurements for GJ 22 AC with the near-infrared cameras MAGIC and OMEGA Cass at the 3.5 m telescope on Calar Alto. These instruments are capable of taking fast sequences of short time exposures ($t_{exp} \sim 0.1$ s) that enable speckle interferometry observations at the infrared wavelengths where red dwarfs emit significant flux and where atmospheric turbulence is reduced compared to visual wavelengths. We also include a few speckle observations at optical wavelengths from the Special Astrophysical Observatory 6 m BTA and 1 m Zeiss (Balega et al. 1994), from the CFHT (Blazit et al. 1987) and from the DSSI (Differential Speckle Survey Instrument) on the WIYN Observatory 3.5 m (Horch et al. 2012).

Table 3
Radial Velocities[a]

ID	mJD[b]	Primary (km s^{-1})	Secondary (km s^{-1})
GJ 22 AC	49962.9	-5.86 ± 0.22	...
	50405.7	-5.52 0.38	...
	50723.8	-6.12 0.26	...
	51136.8	-5.74 0.24	...
	52809.9	-2.52 0.58	...
	53936.4	-3.93 0.30	...
	54305.9	-4.48 0.29	...
	54875.3	-5.27 0.29	...
GJ 234 AB	50418.425	14.31 ± 0.21	...
	50872.199	13.30 0.14	...
	53405.268	18.16 0.28	...
	53802.188	17.63 0.44	...
	54482.211	16.57 0.23	...
	54875.227	16.59 0.34	...
GJ 469 AB	50090.947	-9.0 ± 0.5	-2.6 ± 1.4
	50213.681	-8.1 0.1	...
	50584.711	-4.2 0.2	-12.3 1.1
	50871.807	-2.5 0.1	-12.6 0.6
	51192.948	-3.0 0.1	-13 0.5
	52328.860	-6.2 0.1	...
	52807.660	-7.9 0.1	...
	53194.648	-9.6 0.4	-3.3 0.9
	53801.735	-10.4 0.1	-0.4 0.7
	54481.941	-7.3 0.1	...
	54874.877	-4.0 0.2	-12.2 1.0
GJ 623 AB	49961.404	-27.44 ± 0.17	...
	50091.543	-25.16 0.11	...
	50214.024	-25.39 0.07	...
	50365.105	-25.79 0.11	...
	50528.213	-26.38 0.06	...
	50584.990	-26.39 0.07	...
	50871.952	-27.29 0.19	...
	51022.759	-27.88 0.17	...
	51026.746	-27.90 0.06	...
	51078.640	-28.19 0.12	...
	51191.773	-28.63 0.07	...
	51311.600	-27.84 0.08	...
	51315.589	-27.89 0.04	...
	51466.361	-24.97 0.08	...
	52052.320	-26.59 0.09	...
	52808.250	-25.29 0.06	...
	53935.700	-29.34 0.07	...
	54305.320	-25.74 0.02	...
	54484.500	-25.88 0.03	...
	54874.470	-26.73 0.04	...
	HET	...	...
	52301.509	-7.330 0.020	...
	52328.434	-7.415 0.013	...
	52328.442	-7.417 0.014	...
	52437.141	-7.967 0.009	...
	52440.154	-7.975 0.010	...
	52442.354	-7.985 0.010	...
	52443.355	-7.988 0.009	...
	52447.330	-8.020 0.008	...
	52514.142	-8.499 0.009	...
	52517.140	-8.524 0.008	...
	52523.133	-8.565 0.009	...
	52526.142	-8.588 0.009	...
	52537.102	-8.675 0.010	...
	52552.055	-8.809 0.013	...
GJ 748 AB	46627.500	-42.42 ± 0.30	...
	46665.500	-42.41 0.30	...
	46899.500	-41.75 0.30	...
	49960.650	-33.96 0.16	-50.49 0.77

Table 3
(Continued)

ID	mJD[b]	Primary (km s^{-1})	Secondary (km s^{-1})
	50214.420	-41.81 0.06	-34.21 0.39
	50364.960	-42.64 0.05	-33.75 0.64
	50403.590	-42.64 0.11	-33.55 0.82
	50530.010	-41.73 0.14	-35.58 0.36
	50584.560	-41.1 0.06	-36.69 0.22
	50723.090	-38.74 0.09	-40.98 0.09
	51028.800	-39.54 0.07	...
	51079.690	-41.37 0.06	-36.21 0.42
	51138.580	-42.22 0.12	-34.25 0.93
	51313.700	-42.53 0.06	-33.88 0.49
	51466.120	-41.43 0.05	-35.94 0.22
	54305.755	-39.95 0.07	-39.95 0.07
GJ 791.2 AB[c]	49963.710	-30.23 ± 1.49	-44.39 ± 3.72
	50216.912	-38.08 3.71	-30.30 2.50
	50366.323	-35.10 1.81	...
	50405.597	-32.90 1.00	-38.77 3.50
	50723.541	-36.85 0.52	-30.44 0.55
	51027.856	-29.44 2.65	-45.81 5.28
	51078.684	-33.96 0.86	-34.89 1.29
	51081.702	-33.17 0.36	-34.10 0.36
	51138.031	-35.96 0.73	-31.36 2.14
	51316.892	-37.26 2.25	-30.08 2.42
	52948.094	-36.23 0.44	-30.92 0.20
	53196.559	-30.19 0.72	-43.28 0.59
GJ 831 AB	49962.714	-64.47 ± 1.56	-58.00 ± 2.80
	50214.958	-64.21 6.24	-58.70 6.32
	50365.663	-58.11 1.14	-66.44 1.62
	50404.616	-56.28 0.48	-70.47 1.06
	50424.611	-54.57 1.14	-70.99 1.46
	50722.793	-65.00 1.14	-56.51 1.14
	51028.850	-61.47 1.00	-61.47 1.00
	51136.640	-54.73 0.36	-72.74 2.36
	52052.910	-63.69 2.22	-57.50 4.00
	52807.990	-63.92 1.68	-57.24 4.62
	53195.080	-57.55 1.44	-67.53 2.50
	53935.040	-55.57 0.54	-70.70 2.66
	54305.980	-64.71 1.14	-55.92 1.52

Notes.
[a] All velocity units in km s^{-1}.
[b] mJD = JD-2400000.0.
[c] Velocities from Hα line only.

(This table is available in machine-readable form.)

2.2.5. Other HST Astrometry

Where available, we use astrometric observations from *HST* instruments other than the FGSs, including the Faint Object Camera (FOC) (Barbieri et al. 1996), the Faint Object Spectrograph (FOS) (Schultz et al. 1998), the Near-Infrared Camera and Multi-Object Spectrometer (NICMOS) (Golimowski et al. 2004), and the Wide-Field Planetary Camera 2 (WFPC2) (Schroeder et al. 2000; Dieterich et al. 2012).

3. RADIAL VELOCITIES

Adding RVs to the astrometry allows us to completely sample the motion of a binary system; in tandem, the two data sets improve the accuracies of the final component masses. RVs have particular value for the longer-period systems lacking consistent astrometric coverage of the entire orbit (GJ 22 AC, GJ 234 AB, GJ 469 AB, and GJ 623 AB). We have RVs for 11 system

Table 4
Results from Radial Velocities[a]

ID	V	ΔV	K_A	K_B	γ	#A	$A \langle|res|\rangle$	#B	$B \langle|res|\rangle$
GJ 22 AC	10.05	3.08	1.92	⋯	−4.45	8	0.21	⋯	⋯
	⋯	⋯	0.02	⋯	0.05	⋯	⋯	⋯	⋯
GJ 234 AB	11.99	3.08	2.28	⋯	16.18	6	0.23	⋯	⋯
	⋯	⋯	0.01	⋯	0.04	⋯	⋯	⋯	⋯
GJ 469 AB	12.06	1.59	3.82	6.77	−6.62	11	0.17	7	0.56
	⋯	⋯	0.03	0.06	0.02	⋯	⋯	⋯	⋯
GJ 623 AB	10.28	5.28	2.20	⋯	−26.79	14	0.01	(HET)	⋯
	⋯	⋯	0.02	⋯	0.01	14	0.10	(CE)	⋯
GJ 748 AB	11.12	1.81	5.07	10.03	−39.61	16	0.10	12	0.17
	⋯	⋯	0.04	0.09	0.02	⋯	⋯	⋯	⋯
GJ 791.2 AB	13.37	3.27	4.09	8.54	−34.24	12	0.70	11	0.66
	⋯	⋯	0.08	0.13	0.07	⋯	⋯	⋯	⋯
GJ 831 AB	12.06	2.10	5.17	9.64	−61.37	13	0.39	13	0.96
	⋯	⋯	0.06	0.10	0.11	⋯	⋯	⋯	⋯

Note.

[a] All velocity units in km s^{-1}. Errors for RV amplitudes K_A, K_B, and system velocity, γ, are just below each entry. #A and #B are numbers of unique epochs of RV measurements. $A \langle|res|\rangle$ and $B \langle|res|\rangle$ are average absolute-value RV residuals in km s^{-1}.
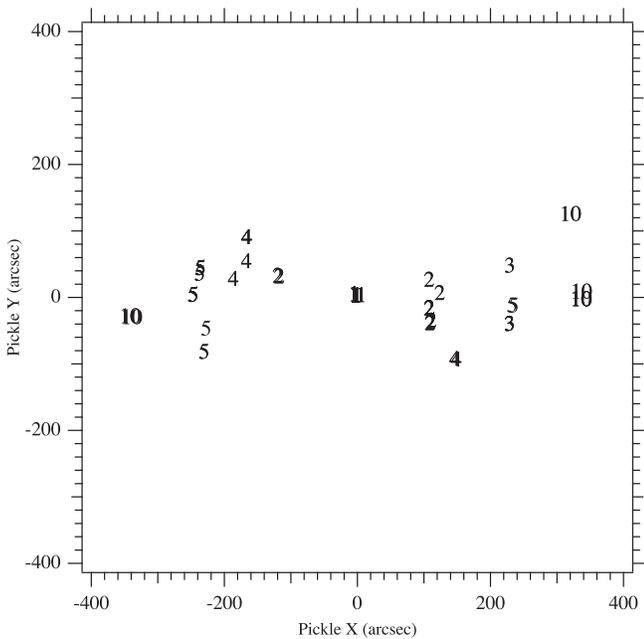

Figure 1. Positions within FGS 3 of GJ 831 AB and reference stars (ID numbers from Table 5) for all 10 observation sets. The "1" indicates the location of the GJ 831 AB photocenter. Reference stars 6–9, identified in the original *HST* Phase 2 submission, were never observed, either due to faintness or placement within the FGS field of view (FOV).

Figure 2. $J−K$ vs. $V−K$ color–color diagram for GJ 831 AB and reference stars described in Table 5. The dashed line is the locus of dwarf (luminosity class V) stars of various spectral types; the dot-dashed line is for giants (luminosity class III) from Cox (2000). The reddening vector indicates $A_V = 1.0$ for the plotted color systems. For this field at Galactic latitude $\ell^{II} = −40°$, we estimate $\langle A_V \rangle = 0.00 \pm 0.06$ magnitude with a maximum of 0.11 (Schlafly & Finkbeiner 2011).

components out of the 30 for which we present new masses. The value of the RV data sets depends on the brightnesses and magnitude differences of the components in each binary, given in Tables 2 and 10. Our RV measurements, listed in Table 3, are from two sources, described next. RV orbit semiamplitudes and systemic velocities for the 11 stars in seven systems are given in Table 4.

3.1. McDonald Cassegrain Echelle Spectrograph

We obtained most RV data with the McDonald 2.1 m Struve telescope and the Sandiford Cassegrain Echelle spectrograph (McCarthy et al. 1993), hereafter CE. The CE delivers a
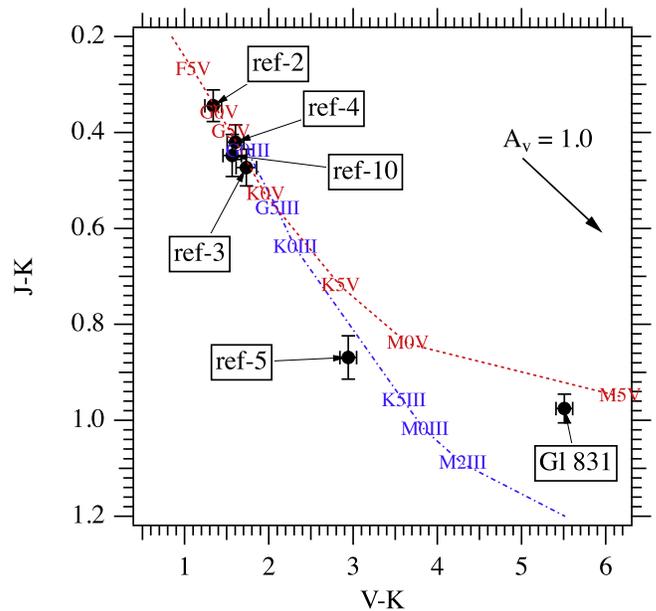
dispersion equivalent to 2.5 km s^{-1}/pix ($R = \lambda/\Delta\lambda = 60,000$) with a wavelength range of $5500 \leqslant \lambda \leqslant 6700$ Å spread across 26 orders (apertures). The McDonald data were collected during 33 observing runs from 1995 to 2009 and reduced using the standard IRAF (Tody 1993) echelle package tools, including the cross-correlation tool fxcorr. We visually inspected the resulting cross-correlation functions (CCF) to select the better of the 26 apertures, typically using half for each binary. Four systems (GJ 469 AB, GJ 748 AB, GJ 791.2 AB, GJ 831 AB) had detectable double peaks in their CCF; these have $\Delta V = $ 1.59–3.27. For these we used an IRAF script to average the lower-noise CCF. We then used a Gaussian multipeak fitting
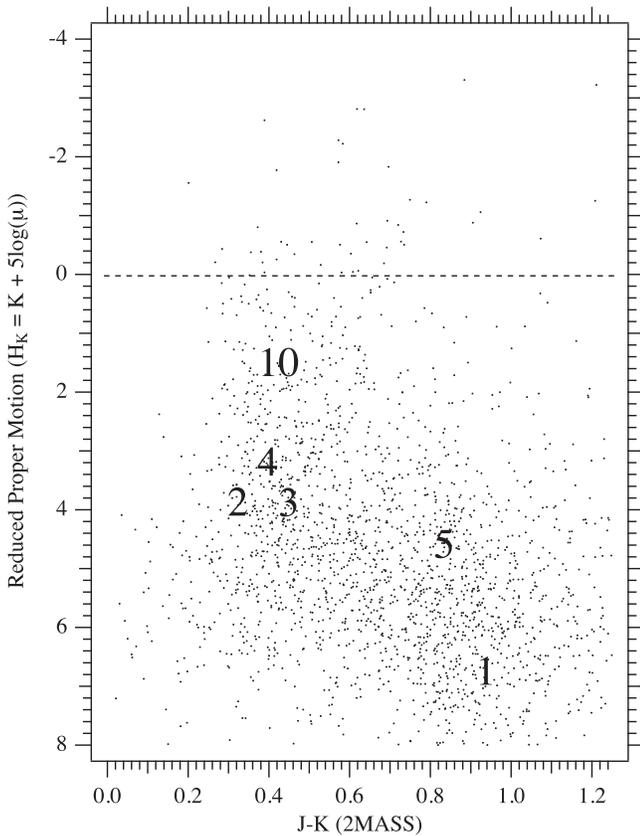
Figure 3. Reduced proper-motion diagram for 2378 stars taken from a 2° × 2° field centered on GJ 831 AB. Star identifications are shown for astrometric reference stars 2, 3, 4, 5, and 10 in Table 5. Star "1" is GJ 831 AB. The H_K for all numbered stars is calculated using proper motions from the PPMXL and K magnitude from 2MASS. See Section 4.3 for a discussion of ref-5 and ref-10.

routine in the GUI-based commercial package IGOR[11] to derive component ΔRVs. We obtained the RVs for the three single-peak CCF systems (GJ 22 AC, GJ 234 AB, and GJ 623 AB) through a weighted average of the `fxcorr` output velocities. For all systems, we averaged the velocities derived from observations taken during the span of a few days (our typical observing run lasted four nights) to form average absolute heliocentric velocities at the epochs plotted in Sections 4.6 and 5.

3.2. HET and Other Sources

Some GJ 623 AB velocities came from the Hobby–Eberly Telescope (HET) using the Tull Spectrograph, as did our high-resolution, high signal-to-noise spectrum of GJ 623 AB used as a template for all cross-correlations. We identify a few other sources of RVs in the individual object modeling notes below (Section 5). The HET became fully functional about halfway through our CE campaign, so we decided to remain with the McDonald 2.1 m CE system for the entire data sets for the six other systems with RVs.

4. AN ANALYSIS OF GJ 831 AB

As a guideline for all 15 systems for which we determine masses, the following sections provide details of the analysis path leading to the determination of component masses for

---

[11] https://www.wavemetrics.com

GJ 831 AB. Section 5 provides summary information for the other 14 systems, indicating where the mass derivations differ from GJ 831 AB.

Ségransan et al. (2000) summarizes previous knowledge of the orbit and mass of this system.

4.1. The GJ 831 AB Astrometric Reference Frame

Figure 1 shows the distribution in FGS coordinates of the 10 sets of five reference-star (numbers 2, 3, 4, 5, and 10) POS-mode measurements for the GJ 831 AB reference frame, where 1 indicates GJ 831 AB. The elongated pattern is affected by the pickle-like shape of the FGS field of regard and the requirement that *HST* roll to keep its solar panels fully illuminated throughout the year. Not all reference stars were measured at each epoch, nor were all stars measured by the same FGS. We acquired the first six POS data sets with FGS 3 and the last four sets with FGS 1r. We obtained a total of 71 reference-star observations and 29 observations of GJ 831 AB. We note in Table 6 that we have more position angle and separation TRANS-mode measurements (18) over 6.61 years than we have for component-A POS-mode measurements (10) over 4.07 years.

4.2. GJ 831 AB RVs

We have a single source of RV data for this system, including 13 measurement epochs spanning 11.9 years (Table 3) obtained with the McDonald 2.1 m telescope and the Sandiford Casse-grain Echelle spectrograph (McCarthy et al. 1993). Treating GJ 831 AB as a double-lined spectroscopic binary, we obtained velocities for both components at orbital phases $0.3 \leqslant \phi \leqslant 0.98$ (Figure 5, right). Unfortunately, our monitoring missed a critical phase, periastron.

4.3. Prior Knowledge and Modeling Constraints

4.3.1. Reference Stars

As for of our previous parallax projects, for example Benedict et al. (2007, 2009, 2011) and McArthur et al. (2011), we include as much prior information as possible for our modeling. Quantities that inform the modeling include estimates of reference-star absolute parallaxes, various color indices for the reference stars, and proper motions from the PPMXL (Roeser et al. 2010) and FGS lateral color calibrations (e.g., Benedict et al. 1999, Section 3.4). In contrast to much of our previous parallax work (e.g., Harrison et al. 1999), for this project we estimate our reference-star absolute parallaxes using only color and proper-motion information.

Because the parallaxes determined for the binary systems will be measured with respect to reference-frame stars that have their own parallaxes, we must either apply a statistically derived correction from relative to absolute parallax (van Altena et al. 1995) or estimate the absolute parallaxes of the reference-frame stars. We choose the latter methodology for the FGS reference fields discussed here. The colors and luminosity class of a star can be used to estimate the absolute magnitude, M_V, and V-band absorption, A_V. The absolute parallax is then simply

$$\pi_{\mathrm{abs}} = 10^{\frac{-(V - M_V + 5 - A_V)}{5}}. \tag{1}$$

Given the galactic latitude of GJ 831 AB ($\ell^{II} = -40°$) and external estimates of low reddening (Schlafly & Finkbeiner

Table 5
GJ 831 AB Reference-star Characteristics and Final Parallaxes

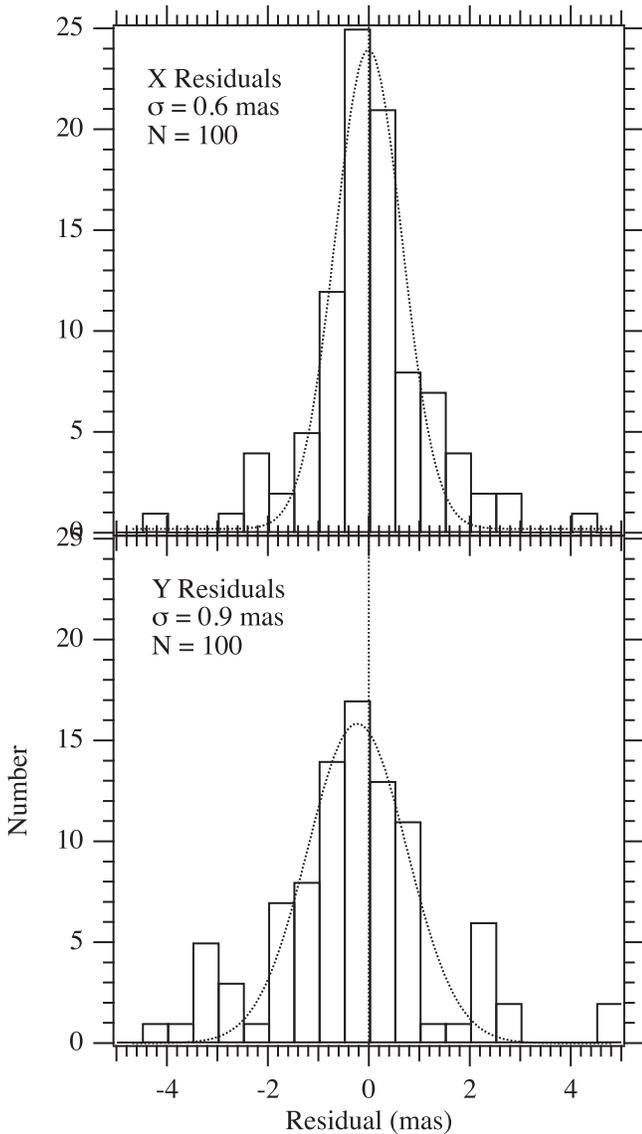| ID	V	$V-K$	$J-K$	Sp.T	M_V	π_{est} (mas)	π_{abs} (mas)
ref-2	13.41	1.38 ± 0.10	0.34 ± 0.03	G0V	4.4	1.6 ± 0.5	1.7 ± 0.2
ref-3	13.65	1.73 0.11	0.47 0.04	G7V	5.4	2.2 0.7	2.2 0.2
ref-4	13.02	1.62 0.10	0.42 0.04	G7V	5.4	3.0 1.0	3.0 0.3
ref-5	14.35	3.01 0.10	0.87 0.05	M1V	9.2	9.0 3.0	8.4 0.9
ref-10	14.67	1.58 0.11	0.45 0.04	G5IV	2.5	0.4 0.2	1.4 0.2

Figure 4. Histograms of GJ 831 AB and reference-star residuals resulting from the application of the model (Equations (5) and (6)) incorporating both astrometry and radial velocities.

2011), a $J-K$ versus $V-K$ color–color diagram (Figure 2) supports an initial assignment of spectral type and dwarf luminosity class to all but reference star ref-5 (with an initial estimate of K2III).

To confirm the reference-star spectral type and luminosity classes estimated from all available photometry, we employ the technique of reduced proper motions (Stromberg 1939; Gould & Morgan 2003; Gould 2004). We obtain proper motions from PPMXL and J and K photometry from 2MASS for sources in a

$2° \times 2°$ field centered on GJ 831 AB. Figure 3 shows a reduced proper motion diagram (RPM), $H_K = K + 5\log(\mu)$ plotted against the $J-K$ color index for that field, where μ is the proper-motion vector absolute value in arcsec yr^{-1}. If all stars had the same transverse velocities, Figure 3 would be equivalent to an HR diagram. GJ 831 AB and associated reference stars are plotted with ID numbers from Table 5. Comparing with our past RPM diagrams (Benedict et al. 2011, 2014; McArthur et al. 2011), all but ref-5 and ref-10 lie on or near the main sequence.

In a quasi-Bayesian approach, we input all priors as observations with associated errors, not as hardwired quantities known to infinite precision. Input proper-motion values have typical errors of 4–6 mas yr^{-1} for each coordinate. The lateral color and cross-filter calibrations and the $B-V$ color indices are also treated as observations with error. Where there is tension between the color–color and RPM diagrams, in this case for ref-5 and ref-10, we run the models with two sets of inputs and adopt the classification that produces the smaller χ^2. The best model results included ref-5 as an M dwarf and ref-10 as a G subgiant. Table 5 contains V magnitudes, colors, estimated spectral types, M_V, input prior parallaxes (estimated from photometry and proper motion), and final parallaxes (as final astrometric modeling results) for the five reference stars used in the GJ 831 AB field.

4.3.2. The M Dwarf Binaries

Parallax was not the primary goal of the FGS effort. Consequently, for the more reference-star-poor fields and those systems with very poor sampling of the parallactic ellipse, we introduce previously determined science target parallaxes as priors. While not included as a prior in the GJ 831 AB modeling, we will flag parallax prior inclusion in the modeling notes for other systems in Section 5. Ultimately, the *HST*/FGS does provide significantly improved parallaxes in most cases.

The derived orbital solutions benefit from a relationship between the two astrometric modes (POS and TRANS) and the RV measurements, which together are enforced by the constraint (Pourbaix & Jorissen 2000)

$$\frac{\alpha_A \sin i}{\pi_{abs}} = \frac{P K_A \sqrt{(1-e^2)}}{2\pi \times 4.7405}. \quad (2)$$

Quantities derived only from astrometry (parallax, π_{abs}, primary perturbation orbit size, α_A, and inclination, i) are on the left, and quantities derivable from both RVs and astrometry (the period P in years and eccentricity, e) or RVs only (the RV amplitude for the primary, K_A in km s^{-1}) are on the right. An object traveling 4.7405 km s^{-1} will move 1 au in 1 year. When RVs for both components exist, we employ an additional constraint, substituting K_B for K_A and the component-B orbit

Table 6
Astrometry Data Spans and Residuals[a]

ID	#ref	$\langle V \rangle$ ref	POS span (year)	POS[b] #obs	POS $\langle |res| \rangle$ (mas)	TRANS span (year)	TRANS #obs	TRANS $\langle |res| \rangle$ (mas)
GJ 1005 AB	2	14.5	4.36	12	1.2	4.36	17	1.4
GJ 22 AC	4	14.4	6.06	6	0.8	9.22	9	3.3
GJ 22 AC	⋯	⋯	⋯	⋯	⋯	15.04	23[c]	10.1
GJ 54 AB	3	13.22	4.56	6	0.9	9.15	9[c]	2.2
GJ 65 AB	⋯	⋯	⋯	⋯	⋯	1.47	13	3.5
GJ 65 AB	⋯	⋯	⋯	⋯	⋯	63.0	51[d]	81.4
GJ 1081 AB	6	14.05	4.00	5	0.7	10.47	11	2.1
GJ 234 AB	5	14.21	5.5	7	0.8	13.90	11	2.4
G 250-029 AB	3	15.27	7.65	7	2.6	12.08	14	1.9
G 193-027 AB	5	11.76	3.02	6	0.9	8.95	10[c]	1.3
GJ 469 AB	3	12.73	6.53	7	0.9	10.33	12	1.8
GJ 473 AB	⋯	⋯	⋯	⋯	⋯	10.46	11	2.5
GJ 473 AB	⋯	⋯	⋯	⋯	⋯	23.00	25[c]	11.3
GJ 623 AB	5	14.04	3.14	13	1.0	12.18	9[c]	4.5
GJ 748 AB	4	12.93	1.83	15	1.3	14.78	18	1.4
GJ 1245 AC	7	11.81	5.00	6	0.9	9.45	12[c]	3.7
GJ 791.2 AB	3	13.70	5.04	16	0.8	12.84	5	2.8
GJ 831 AB	5	13.85	4.07	10	1.4	6.61	17	1.8

Notes.
[a] #ref—number of astrometric reference stars; $\langle V \rangle$ref—average V magnitude of the reference stars; POS span—length of POS campaign; #POS—number of epochs of POS observation; POS $\langle |res| \rangle$—average absolute value of POS astrometric residuals; TRANS span—length of TRANS campaign; #TRANS—number of epochs of TRANS observation; TRANS $\langle |res| \rangle$—average absolute value of TRANS astrometric residuals, unless noted with other observations.
[b] For some orbit plots, the number of POS plotted appears less than listed here because of overplotting and plot resolution.
[c] Includes measurements in addition to *HST* TRANS.
[d] Ground-based astrometry only.

Table 7
Parallaxes and Proper Motions

ID	π_{abs} YPC/other (mas)	π_{abs} HIP[a] (mas)	π_{abs} HST (mas)	$\mu_{R.A.}$ HST (mas yr^{-1})	$\mu_{Decl.}$ HST (mas yr^{-1})
GJ 1005 AB[b]	182.1 ± 6.8	200.5 ± 9.4	166.6 ± 0.3	642.0 ± 0.3	−616.3 ± 0.4
GJ 22 AC	...	99.4 2.2	99.2 0.6	1749.7 0.3	−254.3 0.2
GJ 54 AB	...	122.0 2.4	126.9 0.4	386.2 0.2	579.7 0.1
GJ 65 AB	373.7 2.7	...	...	...	...
GJ 1081 AB	65.2 1.8	...	65.2 0.4	54.9 0.2	−365.2 0.2
GJ 234 AB	244.2 3.7	242.3 3.1	241.0 0.4	700.0 0.4	−675.0 0.3
G 250-029 AB	84.0 4.8	95.4 2.4	95.6 0.3	518.0 0.5	−995.4 0.2
G 193-027 AB[b]	108.8 1.9[c]	...	112.6 1.4	677.6 0.6	−914.5 0.4
GJ 469 AB	72.0 6.4	75.9 4.0	76.4 0.5	−634.3 0.2	−259.4 0.2
GJ 473 AB	235.5 2.9[d]	...	...	...	...
GJ 623 AB[b]	131.2 4.8	124.1 1.2	125.0 0.3	1145.2 0.3	−450.7 0.3
GJ 748 AB[b]	99.8 2.4	97.8 3.0	98.4 0.3	1783.5 0.5	−523.0 0.5
GJ 1245 AC	220.2 1.0	...	219.9 0.5	439.1 0.9	−537.9 0.4
GJ 791.2 AB[b]	113.8 1.9	...	113.4 0.2	673.1 0.2	122.0 0.2
GJ 831 AB[b]	...	120.5 6.0	125.3 0.3	1191.8 0.2	−61.4 0.2

Notes.
[a] From van Leeuwen (2007).
[b] No parallax prior in modeling.
[c] Relative parallax from Khrutskaya et al. (2010).
[d] Absolute parallax from RECONS astrometry program at CTIO/SMARTS 0.9 m (see Henry et al. 2006).

size, $\alpha_B = a - \alpha_A$, for α_A, where a is the orbital semimajor axis. Finally, given the simple orbital mechanics of these binary systems, we constrain the longitudes of periastron passage, ω_A and ω_B, to differ by 180°.

4.4. The Astrometric Model

From the astrometric data, we determine the scale, rotation, and offset "plate constants" relative to an arbitrarily adopted constraint epoch (the so-called "master plate") for each

Table 8
Component Position Angles, Separations, Residuals, and Sources[a]

ID	set	mJD	ρ (mas)	$\Delta \rho$ (mas)	θ (degree)	$\Delta \theta$ (degree)	$\rho \Delta \theta$ (mas)	Sources[a]
GJ 1005 AB								
	1	49208.5915	397.7	0.0	123.9	−0.2	−1.4	FGS 3
	2	49494.5823	286.6	2.7	159.8	0.5	2.4	FGS 3
	3	49579.3203	242.1	1.3	178.3	0.5	1.9	FGS 3
	4	49640.6823	213.8	−0.8	198.3	−1.2	−4.3	FGS 3
	5	49687.0690	194.1	1.4	213.4	0.9	3.1	FGS 3
	6	49893.4353	193.6	2.4	303.2	0.5	1.8	FGS 3
	7	49930.6908	198.3	0.8	318.3	0.1	0.5	FGS 3
	8	49971.2335	205.3	−2.8	333.7	0.2	0.8	FGS 3
	9	50020.1770	209.2	−0.5	351.8	0.1	0.3	FGS 3
	10	50062.1808	218.2	−1.0	6.1	0.1	0.4	FGS 3
	11	50236.7703	281.0	0.4	51.2	0.0	0.0	FGS 3
	12	50257.9548	290.5	0.0	54.7	0.5	2.7	FGS 3
	13	50292.6535	305.7	−0.1	61.3	0.0	−0.1	FGS 3
	14	50442.0408	364.0	−0.9	81.5	0.3	2.2	FGS 3
	15	50628.3183	406.2	−0.2	101.5	−0.5	−3.8	FGS 3
	16	50761.9998	410.6	0.6	112.6	0.6	4.0	FGS 3
	17	50800.3510	410.1	−1.5	116.8	−0.1	−0.8	FGS 3
GJ 22 AC								
	1	49935.7677	525.7	−0.6	156.2	0.2	1.8	FGS 3
	2	50268.9853	530.2	−6.0	170.9	−0.2	−2.3	FGS 3
	3	50606.5859	501.9	−5.3	185.6	0.1	0.6	FGS 3
	4	50955.6553	437.9	15.4	200.7	−2.0	−15.2	FGS 3
	5	51843.5050	321.5	0.3	290.9	0.1	0.7	FGS 1r
	6	52207.2940	390.2	−1.6	326.5	−0.7	−4.9	FGS 1r
	7	52572.5440	458.9	3.9	349.0	0.2	1.3	FGS 1r
	8	52937.7940	490.9	0.1	8.3	−0.2	−1.6	FGS 1r
	9	53303.4093	481.9	−0.3	26.6	0.2	1.7	FGS 1r
	10	47811.7546	451.0	9.1	42.7	6.3	49.7	SPK
	11	47870.7425	453.0	8.0	43.9	4.0	31.8	SPK
	12	48145.9949	405.0	38.4	57.1	−1.0	−7.4	SPK
	13	48520.2665	443.0	−58.8	71.6	−2.1	−16.0	SPK
	14	49260.7379	464.0	−10.4	122.5	1.6	13.1	SPK
	15	49381.0147	478.0	−4.9	129.3	1.4	11.8	SPK
	16	49611.0126	510.0	7.8	141.1	0.7	6.2	SPK
	17	49700.0240	532.0	21.7	145.2	0.0	−0.2	SPK
	18	49999.2368	526.0	6.8	157.5	1.3	12.2	SPK
	19	50355.5382	533.0	17.4	172.1	−0.3	−2.9	SPK
	20	50769.7682	460.0	26.9	190.2	0.8	6.4	SPK
	21	51949.7449	334.0	−3.0	302.3	0.0	0.2	SPK
	22	52216.7792	402.0	12.0	325.5	0.4	2.8	SPK
	23	52566.9809	463.0	9.5	348.2	−0.2	−1.5	SPK
GJ 54 AB								
	1	51126.8845	129.0	−2.1	284.9	1.1	−2.6	NIC
	2	51812.0935	110.6	−1.9	93.1	−0.6	−1.1	FGS 1r
	3	52803.7473	131.5	−2.5	282.5	0.4	−0.9	FGS 1r
	4	53149.2738	65.4	1.4	349.7	−0.9	1.1	FGS 1r
	5	53537.4249	69.9	3.8	48.1	−4.5	−5.5	FGS 1r
	6	53746.4575	112.6	−0.9	233.6	−0.4	−0.9	FGS 1r
	7	53885.6178	109.7	−0.5	105.5	−0.7	−1.4	FGS 1r
	8	54251.7904	88.2	−0.5	145.5	1.6	2.5	FGS 1r
	9	54470.0094	123.4	0.9	285.9	0.1	−0.3	FGS 1r
GJ 65 AB								
	1	32832.7425	1510.0	14.6	118.2	2.4	62.2	VIS
	2	33208.9500	1630.0	−24.4	104.2	4.5	127.4	VIS
	3	33581.5050	1730.0	−56.4	95.5	2.5	75.7	VIS
	4	33932.1450	1670.0	54.4	87.0	1.9	56.4	VIS
	5	34260.8700	1650.0	116.9	83.3	−3.2	−93.2	VIS
	6	34333.9200	1440.0	333.0	75.2	5.7	142.7	VIS
	7	34381.4025	1680.0	107.2	79.1	−1.7	−51.3	VIS
	8	34965.8025	1860.0	17.7	64.9	−0.8	−26.4	VIS
	9	35049.8100	1910.0	−20.7	64.4	−2.1	−69.5	VIS
	10	35396.7975	1880.0	69.1	56.8	−1.9	−63.4	VIS

Table 8
(Continued)

ID	set	mJD	ρ (mas)	$\Delta \rho$ (mas)	θ (degree)	$\Delta \theta$ (degree)	$\rho \Delta \theta$ (mas)	Sources[a]
	11	35762.0475	1950.0	64.5	49.2	−1.5	−49.9	VIS
	12	35776.6575	1870.0	145.2	45.4	2.5	82.2	VIS
	13	36167.4750	2120.0	−32.9	41.4	−1.0	−36.4	VIS
	14	36485.2425	2140.0	−0.9	37.1	−2.2	−82.5	VIS
	15	36561.9450	2180.0	−25.5	32.8	0.8	30.1	VIS
	16	36835.8825	2340.0	−144.4	31.0	−1.6	−67.2	VIS
	17	36867.6593	2180.0	22.5	28.9	−0.3	−10.3	VIS
	18	37412.9775	2300.0	−28.4	20.3	−0.1	−2.9	VIS
	19	37800.1425	2500.0	−198.6	13.1	1.2	52.6	VIS
	20	38037.5550	2530.0	−218.3	11.8	−0.6	−27.2	VIS
	21	38614.6500	2340.0	−46.8	3.5	−0.8	−31.5	VIS
	22	38724.9555	2180.0	101.9	1.5	−0.5	−18.0	VIS
	23	38793.6225	2370.0	−99.6	358.0	1.9	78.0	VIS
	24	39023.3648	2140.0	94.2	356.9	−0.4	−14.1	VIS
	25	39374.0048	2080.0	61.6	351.3	−0.4	−15.0	VIS
	26	39768.4748	1900.0	74.4	345.3	−1.7	−55.6	VIS
	27	40077.8415	1540.0	238.1	340.1	−4.2	−114.2	VIS
	28	40456.9710	1220.0	221.5	328.8	−4.3	−92.5	VIS
	29	40791.5400	1020.0	−15.1	316.6	−7.9	−141.0	VIS
	30	41653.5300	1020.0	−58.7	157.6	3.8	67.6	VIS
	31	42384.0300	1430.0	31.9	119.3	6.5	163.4	VIS
	32	42676.2300	1600.0	−40.6	111.8	3.8	105.6	VIS
	33	42705.4500	1430.0	113.8	107.3	9.0	227.1	VIS
	34	43060.4730	1550.0	80.3	99.3	5.5	150.4	VIS
	35	43411.8435	1640.0	51.1	91.4	3.3	95.5	VIS
	36	43784.7638	1710.0	35.4	82.8	2.1	62.3	VIS
	37	43801.2000	1900.0	−150.3	84.8	−0.4	−11.8	VIS
	38	44164.9890	1660.0	141.1	75.0	0.5	15.9	VIS
	39	44526.2213	1770.0	86.2	66.8	0.3	10.5	CCD
	40	44876.1308	1840.0	73.4	58.8	0.8	24.1	CCD
	41	45245.6907	1971.0	6.8	52.4	−0.5	−15.7	CCD
	42	45246.8595	1820.0	158.1	51.8	0.1	4.7	CCD
	43	45601.8825	2050.0	−17.6	41.3	3.8	135.4	CCD
	44	45605.9003	1930.0	112.0	44.6	0.5	17.2	CCD
	45	45789.6210	1940.0	134.1	40.7	1.2	39.0	CCD
	46	49902.3725	1686.6	−2.3	333.8	−0.1	−3.1	CCD
	47	49915.3754	1648.5	24.6	332.6	0.8	23.4	CCD
	48	49967.3505	1629.9	−1.5	332.0	−0.1	−2.2	CCD
	49	50033.4608	1569.3	−1.8	330.0	−0.1	−2.2	FGS 3
	50	50062.3155	1541.0	−1.4	329.0	−0.1	−1.7	FGS 3
	51	50089.4901	1508.2	4.4	327.9	0.1	3.6	FGS 3
	52	50124.5176	1478.3	−1.7	326.9	−0.1	−1.7	FGS 3
	53	50229.6000	1360.7	0.1	322.8	0.0	0.4	FGS 3
	54	50249.6157	1337.3	0.1	321.9	0.0	0.5	FGS 3
	55	50290.6333	1287.8	0.1	320.1	0.0	0.7	FGS 3
	56	50316.6756	1256.4	−0.9	318.9	0.0	0.0	FGS 3
	57	50316.6756	1255.5	0.0	318.8	0.0	0.8	FGS 3
	58	50437.7560	1095.1	−0.1	312.0	0.1	1.2	FGS 3
	59	52586.9285	1653.0	−19.00	103.3	0.6	17.0	WFPC2
	60	54341.3445	1930.0	−12.11	61.24	0.1	4.5	NACO
	61	54756.2139	1975.0	10.64	53.11	−0.1	−2.1	NACO
	62	54786.0393	1987.0	3.56	52.62	−0.1	−5.1	NACO
	63	55485.1899	2095.0	10.10	39.36	0.4	13.6	NACO
	64	55827.2696	2134.0	23.76	33.47	0.5	19.3	NACO
GJ 1081 AB								
	1	50183.9186	349.7	−0.1	46.4	−0.8	−4.8	FGS 3
	2	51406.9947	267.0	−1.5	40.5	0.2	0.8	FGS 1r
	3	51637.0292	230.1	−0.3	38.9	0.2	1.0	FGS 1r
	4	52000.4529	161.3	0.8	34.3	0.8	2.3	FGS 1r
	5	52366.5430	76.9	3.8	26.7	−3.2	−4.4	FGS 1r
	6	52731.7930	35.6	−4.2	285.0	−9.5	−5.9	FGS 1r
	7	53098.1388	98.1	−1.2	54.3	−0.3	−0.6	FGS 1r
	8	53460.6859	255.7	3.3	48.7	0.3	1.2	FGS 1r

Table 8
(Continued)

ID	set	mJD	ρ (mas)	Δρ (mas)	θ (degree)	Δθ (degree)	ρΔθ (mas)	Sources[a]
	9	54009.8028	340.8	−0.9	46.4	0.1	0.6	FGS 1r
GJ 234 AB								
	1	49944.9720	719.2	4.4	134.7	−0.1	−1.0	FGS 1r
	2	50174.0934	708.9	−1.3	152.5	0.0	0.4	FGS 1r
	3	50554.2456	745.0	−1.1	180.8	0.3	3.4	FGS 1r
	4	50936.8449	734.3	1.6	207.1	0.0	0.0	FGS 1r
	5	51416.9295	494.8	2.8	257.3	0.2	2.0	FGS 1r
	6	51623.1497	442.4	−5.8	294.8	0.4	3.3	FGS 1r
	7	51987.5961	664.0	−0.9	348.4	0.1	0.8	FGS 1r
	8	52718.6440	1198.8	−5.5	22.9	−0.1	−3.0	FGS 1r
	9	53084.9898	1336.1	−1.2	31.7	−0.2	−4.8	FGS 1r
	10	53449.1440	1392.4	2.0	39.4	−0.1	−1.6	FGS 1r
	11	53631.4038	1397.7	0.9	43.3	0.2	4.8	FGS 1r
G 250-029 AB								
	1	49940.9178	95.4	0.9	344.2	2.7	4.5	FGS 3
	2	50313.1075	324.1	−3.8	296.0	0.8	4.5	FGS 3
	3	50707.5775	460.8	−1.0	286.8	−0.6	−4.9	FGS 3
	4	50929.6860	501.4	4.0	283.2	−0.4	−3.4	FGS 3
	5	51549.8440	504.6	−4.1	272.2	0.5	4.6	FGS 1r
	6	51661.2818	489.0	2.1	271.0	0.1	1.3	FGS 1r
	7	52024.4864	428.6	0.1	263.6	0.0	0.0	FGS 1r
	8	52359.6033	357.6	−0.7	254.4	0.1	0.8	FGS 1r
	9	52722.6618	272.2	−1.5	238.0	−0.6	−2.8	FGS 1r
	10	53087.9118	205.5	0.5	210.0	−0.4	−1.4	FGS 1r
	11	53452.4313	198.8	−1.0	170.7	0.1	0.2	FGS 1r
	12	53623.3683	218.5	−1.4	153.9	0.3	1.3	FGS 1r
	13	53992.6360	281.6	1.3	128.8	0.1	0.7	FGS 1r
	14	54354.9640	285.1	0.4	111.2	−0.2	−1.1	FGS 1r
G 193-027 AB								
	1	51550.9398	146.3	−2.1	5.2	−0.4	−0.9	FGS 1r
	2	51651.7488	163.0	1.8	344.7	0.8	2.3	B04
	3	52711.7043	132.0	−0.8	14.0	−0.6	−1.4	NIC
	4	52942.9075	164.2	−0.6	329.7	−0.5	−1.4	FGS 1r
	5	53310.3490	129.8	−2.8	235.5	1.6	3.7	FGS 1r
	6	53673.4075	105.1	−1.2	140.6	0.5	0.8	FGS 1r
	7	53677.7467	102.3	−0.2	139.1	0.0	0.1	FGS 1r
	8	54046.8683	163.8	1.3	343.8	1.0	2.8	FGS 1r
	9	54592.1610	136.1	0.8	214.2	−0.4	−0.9	FGS 1r
	10	54819.3282	122.1	1.5	159.1	−0.1	−0.1	FGS 1r
GJ 469 AB								
	1	49927.2209	217.9	3.7	180.3	0.9	3.5	FGS 3
	2	50235.3823	83.6	−4.7	144.8	−0.5	−0.8	FGS 3
	3	50606.6954	171.0	0.3	28.0	0.0	0.1	FGS 3
	4	50936.9910	276.5	−2.6	12.9	0.6	2.8	FGS 3
	5	51680.4939	252.7	1.4	350.0	0.1	0.3	FGS 1r
	6	52043.9177	179.5	1.8	330.7	−0.4	−1.3	FGS 1r
	7	52436.6710	124.0	1.0	283.6	−0.2	−0.4	FGS 1r
	8	52774.8925	160.9	−0.7	238.1	0.5	1.3	FGS 1r
	9	53145.2560	237.7	0.3	213.1	−0.8	−3.5	FGS 1r
	10	53510.5060	291.7	−0.1	201.3	0.0	0.1	FGS 1r
	11	53700.4360	301.4	−4.1	196.7	0.0	0.0	FGS 1r
GJ 473 AB								
	1	46595.3260	1098.0	4.5	322.7	−2.9	−56.0	SPK
	2	47906.6100	220.0	−14.4	278.0	−13.0	−50.7	H93
	3	47958.1103	179.0	14.0	248.0	2.2	6.8	H93
	4	47958.8408	177.0	15.1	246.0	4.3	13.4	H93
	5	48023.1248	177.0	4.7	226.0	2.2	6.9	H93
	6	48052.6735	186.0	−3.6	210.5	7.3	23.9	H93
	7	48343.8143	430.0	−51.8	160.0	3.8	28.5	H93
	8	48374.1300	343.0	61.9	164.0	−2.1	−12.6	H93
	9	48375.2258	374.0	31.8	164.0	−1.8	−11.9	H93
	10	48411.3855	436.0	−1.4	161.6	−1.5	−11.2	H93
	11	49116.0989	602.0	−10.5	135.8	0.1	1.6	SPK

Table 8
(Continued)

ID	set	mJD	ρ (mas)	$\Delta \rho$ (mas)	θ (degree)	$\Delta \theta$ (degree)	$\rho \Delta \theta$ (mas)	Sources[a]
	12	49927.6478	236.1	−1.0	25.9	−0.2	−0.9	FGS 3
	13	50190.2626	416.0	2.6	353.2	0.6	4.3	FOS
	14	50251.7342	464.0	3.3	350.5	−0.4	−3.0	FGS 3
	15	50607.3050	734.4	0.7	338.5	−0.1	−0.8	FGS 3
	16	50905.6778	924.8	−3.5	333.4	−0.1	−1.2	FGS 3
	17	51679.6060	1177.8	1.6	325.7	−0.1	−1.5	FGS 1r
	18	52012.5679	1179.4	0.8	322.2	0.7	15.1	FGS 1r
	19	52438.9973	1081.2	−1.6	319.2	−0.1	−1.6	FGS 1r
	20	52792.1940	907.4	0.4	315.0	0.0	0.1	FGS 1r
	21	53157.3710	650.6	−0.7	308.1	0.0	−0.4	FGS 1r
	22	53521.9635	330.1	5.5	288.6	0.4	2.3	FGS 1r
	23	53748.0533	185.4	1.6	244.9	−1.4	−4.6	FGS 1r
	24	54638.7154	0.6	−4.4	141.8	1.5	17.0	H12
	25	54994.6880	0.6	−12.9	132.7	−0.5	−4.8	H12
GJ 623 AB								
	1	49514.6710	330.0	−20.0	7.0	1.9	11.0	FOC
	2	50308.4323	308.3	6.3	62.1	−1.5	−7.8	FGS 3
	3	50336.3374	314.5	8.2	60.3	−2.6	−14.2	FGS 3
	1	52896.1000	240.4	7.5	79.3	0.6	2.7	M07
	2	53163.3000	340.5	3.3	49.2	0.1	0.5	M07
	3	53401.6000	350.7	1.0	28.7	0.6	3.7	M07
	4	53779.5000	257.1	−8.8	−12.8	0.3	1.1	M07
	5	53909.0000	175.5	−0.2	318.2	−1.1	−3.4	M07
	6	53961.8000	138.4	−1.0	295.6	−1.2	−3.0	M07
GJ 748 AB								
	1	49534.7232	207.3	0.9	346.5	−0.1	−0.5	FGS 3
	2	49578.0784	202.2	−1.0	341.6	−0.1	−0.5	FGS 3
	3	49926.3808	92.0	−0.8	239.4	4.0	6.5	FGS 3
	4	49956.4409	87.6	0.4	216.0	0.3	0.4	FGS 3
	5	49970.3204	87.7	1.3	205.6	−0.6	−0.9	FGS 3
	6	49995.5957	88.1	1.3	188.3	−1.2	−1.8	FGS 3
	7	50030.9884	76.9	3.8	158.6	3.1	4.2	FGS 3
	8	50164.7795	111.7	−0.1	35.8	0.2	0.3	FGS 3
	9	50193.3055	131.5	1.8	24.9	−0.3	−0.6	FGS 3
	10	50230.7802	157.4	0.1	15.9	−0.5	−1.5	FGS 3
	11	50246.8877	164.1	2.6	12.2	−0.1	−0.3	FGS 3
	12	50351.3492	200.4	5.3	355.6	0.3	1.2	FGS 3
	13	50359.2751	202.0	−1.6	356.6	0.0	0.0	FGS 3
	14	50413.5878	205.9	0.2	349.3	0.3	1.0	FGS 3
	15	50529.1894	193.0	−0.4	335.1	−0.3	−1.1	FGS 3
	16	50554.1360	187.0	0.8	331.2	−0.3	−1.0	FGS 3
	17	50591.5376	174.9	0.6	325.8	−0.8	−2.4	FGS 3
	18	54931.8048	203.8	−1.3	348.2	0.8	2.7	FGS 1r
GJ 1245 AC								
	1	50224.6074	620.2	0.1	333.8	0.0	0.0	FGS 3
	2	50573.1655	606.0	0.0	308.6	−0.1	−1.0	FGS 3
	3	50624.2640	609.0	0.5	304.3	0.5	5.8	WFPC2
	4	50733.2546	604.0	−4.6	296.4	0.1	0.8	WFPC2
	5	50908.5015	596.8	6.0	285.1	−1.4	−14.4	FGS 3
	6	51651.7488	457.9	1.6	216.8	0.3	2.1	FGS 1r
	7	52015.1725	455.6	−6.2	166.9	−1.5	−11.6	FGS 1r
	8	52380.4225	599.2	4.0	127.5	−0.1	−0.9	FGS 1r
	9	52747.8640	777.6	0.6	105.8	0.3	4.1	FGS 1r
	10	53113.1140	908.2	−7.1	91.6	−0.3	−5.5	FGS 1r
	11	53478.3640	1004.6	5.9	81.8	0.1	1.7	FGS 1r
	12	53677.4253	1033.8	−0.9	76.2	0.0	0.1	FGS 1r
GJ 791.2 AB								
	1	50236.4474	169.2	−10.9	89.2	−1.1	−3.3	FGS 3
	2	50254.7418	153.3	2.1	84.6	−0.3	−0.8	FGS 3
	3	50338.2445	126.0	−1.1	62.9	0.9	2.0	FGS 3
	4	51789.4124	155.1	3.5	100.8	−0.9	−2.4	FGS 3
	5	54927.8947	127.8	0.0	120.7	0.8	1.8	FGS 1r
GJ 831 AB								

Table 8
(Continued)

ID	set	mJD	ρ (mas)	$\Delta \rho$ (mas)	θ (degree)	$\Delta \theta$ (degree)	$\rho \Delta \theta$ (mas)	Sources[a]
	1	49452.5055	190.2	−0.6	161.4	0.2	0.7	FGS 3
	2	49486.2911	177.8	−0.6	167.5	0.6	1.8	FGS 3
	3	49518.6522	158.7	2.6	175.4	−0.1	−0.4	FGS 3
	4	50011.4841	185.7	1.4	137.7	−0.3	−1.1	FGS 3
	5	50024.1582	191.3	−0.3	140.7	−1.1	−3.6	FGS 3
	6	50200.0261	173.6	−0.1	170.4	−0.7	−2.0	FGS 3
	7	50241.8107	146.2	5.0	179.1	0.8	2.1	FGS 3
	8	50370.5613	88.0	−8.1	254.2	0.4	0.7	FGS 3
	9	50592.1585	113.8	−2.0	102.3	−0.6	−1.2	FGS 3
	10	50614.2927	132.0	−3.1	111.1	0.3	0.8	FGS 3
	11	50776.6828	201.5	−2.0	147.4	0.0	0.0	FGS 3
	12	50966.4302	134.8	4.4	183.9	1.8	4.2	FGS 3
	13	51100.0386	82.5	−2.0	279.9	−1.0	−1.5	FGS 3
	14	51776.7738	79.3	1.4	250.4	−0.5	−0.7	FGS 1r
	15	51807.6740	82.6	−1.7	281.2	−0.3	−0.5	FGS 1r
	16	51836.7844	92.8	−6.0	305.7	1.4	2.2	FGS 1r
	17	51855.4852	86.7	2.0	323.3	−0.8	−1.2	FGS 1r
	18	51866.4427	88.5	−0.6	331.6	−0.1	−0.1	FGS 1r

Note.

[a] Non-FGS measurements: B04—Beuzit et al. (2004), adaptive optics; B87—Blazit et al. (1987), optical speckle; B94—Balega et al. (1994), optical speckle; FOC—Barbieri et al. (1996), *HST*/FOC; FOS—Schultz et al. (1998), *HST*/FOS; H12—Horch et al. (2012), optical speckle; H92—Henry et al. (1992), infrared speckle; M07—Martinache et al. (2007), aperture masking; M91—McCarthy et al. (1991), infrared speckle; NIC—Golimowski et al. (2004), *HST*/NICMOS; VIS/CCD—Geyer et al. (1988), visual, photographic, and CCD measurements; W03—Woitas et al. (2003), infrared speckle; WFPC2—Schroeder et al. (2000), Dieterich et al. (2012), *HST*/WFPC2; NACO—Kervella et al. (2016), VLT/NACO.

(This table is available in machine-readable form.)

observation set. The GJ 831 AB reference frame contains five stars, but only four were observed at each epoch. Hence, we constrain the scales along X and Y to equality and the two axes to orthogonality. The consequences of this choice are minimal. For example, imposing these constraints on the Barnard's star astrometry discussed in Benedict et al. (1999) results in an unchanged parallax and increases the error by 0.1 mas compared to a full six-parameter model (substituting D for $-B$ and E for A in Equation (6), below).

Our reference-frame model becomes, in terms of standard coordinates

$$x' = x + lc_x(B - V) \tag{3}$$

$$y' = y + lc_y(B - V) \tag{4}$$

$$\xi = Ax' + By' + C - \mu_\alpha \Delta t - P_\alpha \pi_\alpha - \text{ORBIT}_\alpha \tag{5}$$

$$\eta = -Bx' + Ay' + F - \mu_\delta \Delta t - P_\delta \pi_\delta - \text{ORBIT}_\delta \tag{6}$$

where x and y are the measured coordinates from *HST*, lc_x and lc_y are lateral color corrections (see Section 3.4 of Benedict et al. 1999), and $B - V$ represents the color of each star, either from the SIMBAD database or estimated from the spectral types suggested by Figure 2. Here, A and B are scale and rotation plate constants, C and F are offsets, μ_α and μ_δ are proper motions, Δt is the epoch difference from the mean epoch, P_α and P_δ are parallax factors, and π_α and π_δ are the parallaxes in R.A. and decl. The parameters ξ and η are relative positions that (once scale, rotation, parallax, the proper motions, and the ORBIT are determined) should not change with time. All Equation (5) and (6) subscripts are in R. A. and decl. because the master constraint plate was rolled into the R.A. decl. coordinate system before the analysis. We

obtain the parallax factors from a JPL Earth orbit predictor (Standish 1990), upgraded to version DE405. Orientation to the sky for the master plate is obtained from ground-based astrometry from the PPMXL (Roeser et al. 2010) with uncertainties in the field orientation of $\pm 0°.1$. This orientation also enters the modeling as an observation with error. Note that because we switched FGS units on *HST* during the sequence of GJ 831 AB observations, two different OFAD and lateral color calibrations entered the modeling. Finally, ORBIT is an offset term that is a function of the traditional astrometric and RV orbital elements listed in Table 9.

For the astrometric solution, we solve simultaneously for a position within our reference frame, a parallax, and a proper motion for the target GJ 831 AB and all reference stars. In addition, for GJ 831 AB, the orbital period (P), the epoch of passage through periastron in modified Julian days (T_0), the eccentricity (e), and the position angle of the line of nodes (Ω) are constrained to be equal in the RV and two modes of astrometry. We also constrain the angle (ω) in the plane of the true orbit between the line of nodes and the major axis to differ by 180° for the component A and B orbits. Only RV provides information with which to determine the velocity half-amplitudes (K_A, K_B) and γ, the systemic velocity. For systems with both RVs and astrometry, the constraint described in Section 4.3.2 ties POS, TRANS, and RVs together, yielding a single self-consistent description of the binary system.

4.5. Assessing Reference-frame Residuals

From histograms of the astrometric residuals for 71 reference-star and 29 GJ 831 AB position measurements (Figure 4), we conclude that we have obtained corrections at the ~1 mas level in

Table 9
Orbital Elements[a]

ID	a ($''$)	α_A ($''$)	inc (°)	Ω (°)	P (days)	T_0	ecc	ω_A (°)	ω_B (°)	f
GJ 1005 AB	0.3037	0.1169	146.1	62.8	1666.1	49850.4	0.364	166.6	−13.4	0.385
	0.0005	0.0004	0.2	0.4	2.5	0.8	0.001	0.5	0.5	0.002
GJ 22 AC	0.5106	0.1425	43.7	178.3	5694.2	51817.2	0.163	284.5	104.5	0.279
	0.0007	0.0011	0.2	0.2	14.9	5	0.002	0.5	0.5	0.002
GJ 54 AB	0.1264	0.0517	126.6	92.2	418.5	53944.6	0.174	46.8	226.8	0.410
	0.0007	0.0003	0.4	0.5	0.2	1.6	0.004	1.4	1.4	0.003
GJ 65 AB	2.0458	⋯	128.3	147.6	9612	41358.4	0.617	⋯	104.6	0.494
	0.0066	⋯	0.3	0.5	12	12	0.004	⋯	0.5	0.003
GJ 1081 AB	0.2712	0.104	97.1	231.5	4066.1	48919.1	0.848	51	231	0.386
	0.0027	0.0013	0.2	0.2	27.5	28.9	0.004	0.7	0.7	0.005
GJ 234 AB	1.0932	0.3537	53.2	210.6	6070.1	51277.1	0.382	220.4	40.4	0.324
	0.0007	0.0015	0.1	0.1	10.2	1.3	0.001	0.1	0.1	0.001
G 250-029 AB	0.4417	0.1539	109.7	107.8	4946.3	54696.1	0.482	238.9	58.9	0.348
	0.0009	0.0023	0.1	0.1	2.2	1.7	0.002	0.2	0.2	0.005
G 193-027 AB	0.1564	0.0773	130.8	173.6	1195.5	51340.5	0.236	72.9	252.9	0.495
	0.0008	0.0008	0.5	0.6	1.4	3.3	0.004	0.9	0.9	0.006
GJ 469 AB	0.3139	0.1131	107.6	190.4	4223	54548.2	0.302	−90.8	89.2	0.360
	0.0008	0.0009	0.1	0.2	2.9	3.2	0.003	0.2	0.2	0.003
GJ 473 AB	0.9167	⋯	103.3	143.5	5772.3	54554	0.301	⋯	350.7	0.477
	0.0017	⋯	0.7	0.1	9.4	8.7	0.002	⋯	0.5	0.008
GJ 623 AB	0.2397	0.0556	152.5	98.3	1367.4	45838.7	0.629	65.4	245.4	0.231
	0.0014	0.0003	0.2	0.5	0.6	2.8	0.004	0.5	0.5	0.002
GJ 748 AB	0.148	0.0503	131.6	−0.4	901.7	50033.2	0.45	27.3	207.3	0.340
	0.0004	0.0003	0.3	0.2	0.3	0.8	0.002	0.4	0.4	0.002
GJ 1245 AC	0.8267	0.336	135.7	261.2	6147	51506.8	0.334	216.1	36.1	0.406
	0.0008	0.0027	0.1	0.2	17	2.1	0.002	0.2	0.2	0.003
GJ 791.2 AB	0.1037	0.0336	145.4	102.2	538.6	51022.7	0.558	12.2	192.2	0.324
	0.0005	0.0003	0.6	1.1	0.1	0.9	0.005	1.5	1.5	0.003
GJ 831 AB	0.1448	0.0505	49.8	326.1	704.9	51164	0.39	190.6	10.6	0.349
	0.0005	0.0004	0.4	0.4	0.5	1.1	0.002	0.9	0.9	0.003

Note.
[a] a—semimajor axis of relative orbit; α—semimajor axis of perturbation of component A; ω_A—longitude of periastron passage of component A; f—mass fraction—$\mathcal{M}_{sec}/(\mathcal{M}_{pri}+\mathcal{M}_{sec})$.

the region available at all *HST* roll angles (an inscribed circle centered on the pickle-shaped FGS field of regard). The resulting reference-frame "catalog" in ξ and η standard coordinates (Equations (5) and (6)) was determined with median absolute errors of $\sigma_\xi = 0.6$ and $\sigma_\eta = 0.9$ mas in X and Y, respectively.

To determine if there might remain unmodeled—but possibly correctable—systematic effects at the 1 mas level, we plotted the GJ 831 AB reference-frame X and Y residuals against a number of spacecraft, instrumental, and astronomical parameters. These included X and Y positions within the pickle, radial distances from the pickle center, reference-star V magnitudes and $B-V$ colors, *HST* spacecraft roll angles, and epochs of observation. We saw no obvious trends, other than an expected increase in positional uncertainty with reference-star magnitude.

4.6. Results of GJ 831 AB Simultaneous Modeling

The results of this simultaneous solution are as follows. Average absolute-value residuals for the RV and POS/TRANS observations of GJ 831 AB are given in Tables 4 and 6, respectively. The absolute parallax and the proper motion are presented in Table 7 (errors are 1σ), where previous parallaxes are also listed. Compared to *Hipparcos*, our precision has improved knowledge of the parallax by a factor of 20. Residuals to the orbit fits for each astrometric measurement

are individually listed in Table 8, while Table 9 contains the orbital parameters with formal (1σ) uncertainties.

Figure 5, left, illustrates component A and B astrometric orbits. The POS-mode component-A residuals and the TRANS residuals (component A–B separations) are all smaller than the dots in Figure 5. Figure 5, right, shows all RV measurements, RV residuals, and the predicted velocity curve from the simultaneous solution, phased to the derived orbital period.

4.7. GJ 831 AB Component Masses

Our orbit solution and derived absolute parallax (Equation (2)) provide an orbital semimajor axis, a in astronomical units, from which we can determine the system mass through Kepler's third law. Given P and a, we solve the expression

$$a^3/P^2 = (\mathcal{M}_A + \mathcal{M}_B) = \mathcal{M}_{tot} \qquad (7)$$

to find (in solar units) $\mathcal{M}_{tot} = 0.414 \pm 0.006\ \mathcal{M}_\odot$. At each instant in the orbits of the two components around the common center of mass,

$$\mathcal{M}_A/\mathcal{M}_B = \alpha_B/\alpha_A, \qquad (8)$$

, a relationship that contains only one observable, α_A, the perturbation orbit size. Instead, we calculate the mass fraction

$$f = \mathcal{M}_B/(\mathcal{M}_A + \mathcal{M}_B) = \alpha_A/(\alpha_A + \alpha_B) = \alpha_A/a, \qquad (9)$$
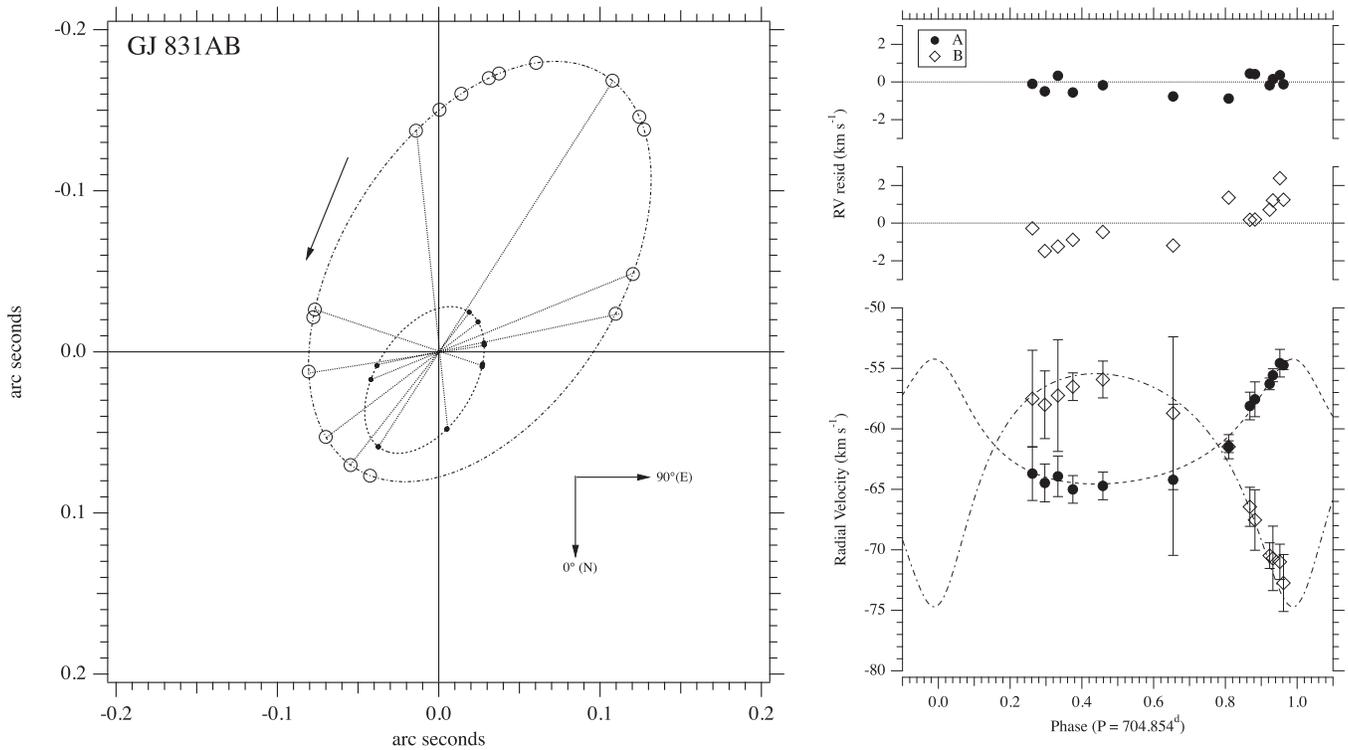
Figure 5. Left: GJ 831 A (dots, POS orbit predicted positions) and component B (open circles, TRANS orbit predicted positions). All observations, POS and TRANS and A and B component radial velocities, were used to derive the orbital elements listed in Table 9. POS and TRANS astrometric residuals (average absolute values for which are listed in Table 6) are smaller than the symbols. The POS mode points on either side of p.a. = 90° each represent two temporally close epochs. The arrow indicates the direction of orbital motion. Right: RV measurements (Table 3) using CE on the McDonald 2.1 m, phased to the orbital period determined from a combined solution including astrometry and RVs. The error bars are 1σ. The dashed lines are component velocities predicted from the orbital parameters derived in the combined solution. Middle and top panels illustrate component B and A RV residuals (average absolute value for which listed in Table 4) from the combined solution.

where $\alpha_B = a - \alpha_A$. This parameter, f (also given in Table 9), ratios the two quantities directly obtained from the observations: the perturbation orbit size (α_A from POS mode) and the relative orbit size (a from TRANS mode), both shown in Figure 5 and listed in Table 9. From these we derive a mass fraction of 0.3489 ± 0.0031. Equations (7)–(9) yield $\mathcal{M}_A = 0.270 \pm 0.004\ \mathcal{M}_\odot$ and $\mathcal{M}_B = 0.145 \pm 0.002\ \mathcal{M}_\odot$, indicating that both components are low-mass red dwarfs with mass errors of ~1.5%, a considerable improvement over the Ségransan et al. (2000) 4% determinations. We collect these component masses and those for the other systems discussed below in Table 10, which also includes V, K, the magnitude differences ΔV and ΔK, and the M_V and M_K values used to create the MLRs.

5. MODELING NOTES AND MASSES FOR OTHER SYSTEMS

The presentation order in this section for the other 14 systems observed with *HST*/FGS 3 and FGS 1r is dictated by dwindling observational resources. We first discuss component mass results for the six other systems with astrometric and RV measurements, then provide notes on the derivation of component masses for the remaining eight systems with astrometric measurements only. The final two systems discussed analyze only position angle and separation measurements (TRANS or ground-based). Among all 15 systems, we provide the first mass determinations for six binary pairs: GJ 54 AB, GJ 469 AB, GJ 831 AB (above), GJ 1081 AB, G

193-027 AB, and G 250-029 AB. For historical context, we provide comparisons with previous mass determinations.

In parallel with our detailed discussion of GJ 831 AB, RV measurements are listed in Table 3 for the first six systems, with RV results (component semiamplitudes, system center-of-mass velocities, number of observations, and residuals to the orbital fits) in Table 4. Astrometric results for all 15 systems are collected in Table 6 (reference-star information, study durations, and average absolute-value residuals to the orbital fits for POS and TRANS), Table 7 (previous parallaxes and derived *HST* parallaxes and proper motions), and Table 8 (observation dates, individual position angles, separations, residuals to the orbital fits, and measurement sources). All analyses yield the orbital elements in Table 9 and component masses in Table 10. All of these tables list the systems in R.A. order.

5.1. GJ 22 AC

The GJ 22 AC system is a triple, with the two close components known as A and C. Our modeling of GJ 22 AC included the four sources of position angle and separation measurements noted in Table 8. *HST* TRANS astrometric measurements came from FGS 3 and FGS 1r, while modeling included POS from only FGS 1r in a reference frame of four stars. We also utilized infrared speckle interferometry measurements from McCarthy et al. (1991) and Woitas et al. (2003). All but one of the POS mode epochs were secured at one-year intervals, very poorly sampling the parallactic ellipse. In this situation, simultaneous modeling including RVs and the Equation (2) constraint could push the parallax to unrealistic values. Therefore we modeled RVs (only for

Table 10
Masses, M_V, and M_K for Red Dwarfs Observed with HST/FGS[a]

ID	$\mathcal{M}_{pri}$	$\mathcal{M}_{sec}$	V[b]	ΔV	ref[c]	$M_V$pri	$M_V$sec	K[d]	ΔK	ref[e]	$M_K$pri	$M_K$sec
GJ 1005 AB	0.179 ± 0.002	0.112 ± 0.001	11.48 ± 0.01	2.39 ± 0.05	*	12.70 ± 0.01	15.12 ± 0.09	6.39 ± 0.02	1.23 ± 0.02	*	7.80 ± 0.02	9.03 ± 0.03
GJ 22 AC	0.405 0.008	0.157 0.003	10.28 0.03	3.08 0.10	H99	10.32 0.03	13.40 0.10	6.04 0.02	1.93 0.03	*	6.19 0.02	8.12 0.04
GJ 54 AB	0.432 0.008	0.301 0.006	9.82 0.02	1.04 0.05	*	10.70 0.03	11.70 0.04	5.13 0.02	...	...	...	...
GJ 65 AB	0.120 0.003	0.117 0.003	12.08 0.02	0.45 0.08	H99	15.49 0.04	15.94 0.05	5.33 0.02	0.16 0.02	*	8.87 0.03	9.03 0.03
GJ 1081 AB	0.325 0.010	0.205 0.007	12.21 0.03	1.67 0.10	H99	11.49 0.04	13.16 0.09	7.34 0.04	0.96 0.01	*	6.79 0.04	7.75 0.04
GJ 234 AB	0.223 0.002	0.109 0.001	11.14 0.03	3.08 0.05	H99	13.11 0.03	16.19 0.06	5.49 0.02	1.58 0.02	*	7.63 0.02	9.21 0.03
G 250-029 AB	0.350 0.005	0.187 0.004	10.95 0.03	1.61 0.08	H99	11.07 0.03	12.68 0.07	6.35 0.02	1.03 0.07	*	6.61 0.03	7.64 0.05
G 193-027 AB	0.126 0.005	0.124 0.005	13.29 0.03	0.30 0.05	*	14.16 0.05	14.46 0.05	7.78 0.02	0.10 0.02	*	8.74 0.03	8.84 0.04
GJ 469 AB	0.332 0.007	0.188 0.004	12.05 0.02	1.59 0.05	H99	11.69 0.03	13.28 0.05	6.96 0.04	1.01 0.02	*	6.74 0.04	7.75 0.04
GJ 473 AB	0.124 0.005	0.113 0.005	12.47 0.04	−0.01 0.05	H99	15.09 0.05	15.08 0.05	6.04 0.02	0.00 0.01	*	8.65 0.03	8.65 0.03
GJ 623 AB	0.379 0.007	0.114 0.002	10.28 0.03	5.28 0.10	B96	10.77 0.03	16.05 0.10	5.92 0.02	2.87 0.14	H93	6.48 0.02	9.35 0.13
GJ 748 AB	0.369 0.005	0.190 0.003	11.10 0.04	1.81 0.04	H99	11.25 0.04	13.06 0.05	6.29 0.02	1.09 0.07	*	6.59 0.03	7.68 0.06
GJ 1245 AC	0.111 0.001	0.076 0.001	13.41 0.03	3.29 0.05	H99	15.17 0.03	18.46 0.06	6.85 0.02	1.05 0.01	*	8.91 0.02	9.96 0.02
GJ 791.2 AB	0.237 0.004	0.114 0.002	13.13 0.04	3.27 0.10	B00	13.46 0.04	16.73 0.10	7.31 0.02	1.28 0.10	*	7.87 0.03	9.15 0.08
GJ 831 AB	0.270 0.004	0.145 0.002	12.02 0.02	2.10 0.06	H99	12.66 0.02	14.76 0.06	6.38 0.02	1.20 0.01	*	7.18 0.02	8.38 0.02

Notes.
[a] Masses ($\mathcal{M}$) in solar masses ($\mathcal{M}_\odot$). Components are Primary—pri, Secondary—sec.
[b] V values from references in Table 2.
[c] References for ΔV and ΔK: *—this paper, B96—Barbieri et al. (1996), B00—Benedict et al. (2000), H93—Henry & McCarthy (1993), H99—Henry et al. (1999).
[d] From 2MASS.
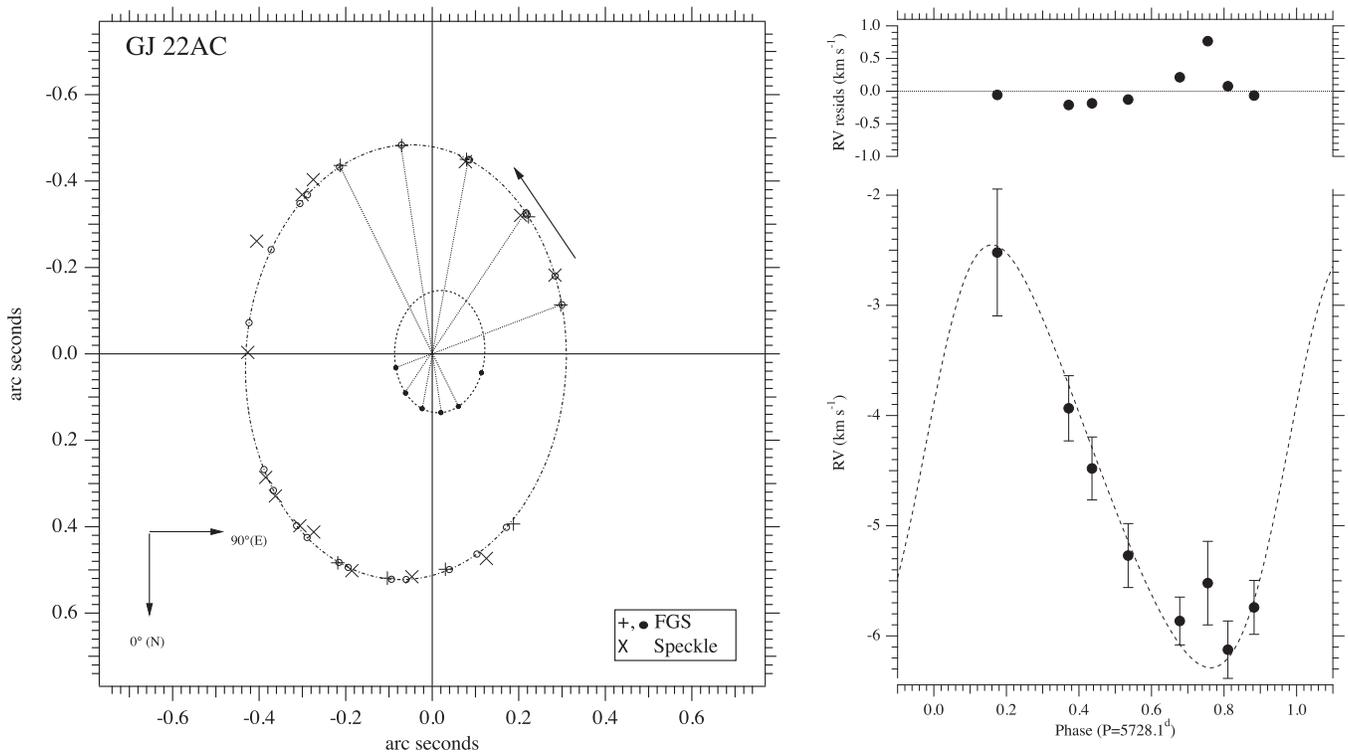
Figure 6. Left: GJ 22 A (dots) POS orbit predicted positions and component C (open circles) TRANS and speckle (McCarthy et al. 1991; Woitas et al. 2003) orbit predicted positions. All observations, POS, TRANS (+), and speckle (×), and component-A radial velocities were used to derive the orbital elements listed in Table 9. POS astrometric residuals (average absolute values for which are listed in Table 6) are smaller than the dot symbols. Right: component-A RV measurements from the present study using CE on the McDonald 2.1 m, phased to the orbital period determined from a combined solution including astrometry and RVs. The error bars are 1σ. The dashed line is the velocity predicted from the orbital parameters derived in the combined solution. Top panel: component-A RV residuals (average absolute values, listed in Table 4) from the combined solution.

GJ 22 A due to the large $\Delta V = 3.08$ value) in combination with the astrometry, with a parallax from *Hipparcos* (van Leeuwen et al. 2007) used as a prior.

Our derived parallax has a larger error (0.6 mas) than typical for an *HST* parallax (0.2–0.3 mas), due to the less-than-ideal sampling. Still, even though all epochs sampled nearly the same part of the parallactic ellipse, they serve to scale the size of that ellipse well enough to provide a useful parallax. We obtain a parallax similar to *Hipparcos* (van Leeuwen et al. 2007), but the precision has improved by a factor of four. The average absolute value of the residuals to the orbit fit (Table 6) for both the TRANS and speckle observations is $\langle|\mathrm{res}|\rangle = 10.1$ mas. For TRANS only, the average absolute-value residuals are $\langle|\mathrm{res}|\rangle = 3.3$ mas, and for speckle only, $\langle|\mathrm{res}|\rangle = 13.4$ mas.

Table 9 contains the GJ 22 AC orbital parameters with formal (1σ) uncertainties. The orbital semimajor axis is now extremely well determined, with an error approaching 0.1%. The orbital period is known to 0.3%, while the parallax error (0.6%) dominates the derived mass errors. The left panel of Figure 6 provides component A and B orbits and shows the observations that entered into the modeling. Component A–B separation residuals from TRANS-mode and speckle observations are illustrated by the offsets (+ and × next to o). Regarding the RV measurements (Figure 6, right), we note that GJ 22 AC has a companion, GJ 22 B, separated from GJ 22 AC by $4''$, with an orbital period on the order of 320 years (Hershey 1973). Figure 7 shows the RV orbit as a function of time, not phase. We may (at a low level of significance) be detecting the AC–B orbital motion as a slope in the RV residuals. We obtain component masses of $\mathcal{M}_A = 0.405 \pm 0.008 \, \mathcal{M}_\odot$ (2.0% error) and $\mathcal{M}_C =$

$0.157 \pm 0.003 \, \mathcal{M}_\odot$ (1.9%). These masses support the excellent early work on this system by Hershey (1973), who found $\mathcal{M}_A = 0.40 \, \mathcal{M}_\odot$ and $\mathcal{M}_C = 0.13 \, \mathcal{M}_\odot$, followed by McCarthy et al. (1991), who found $\mathcal{M}_A = 0.362 \pm 0.053 \, \mathcal{M}_\odot$ (15%) and $\mathcal{M}_C = 0.123 \pm 0.018 \, \mathcal{M}_\odot$ (15%).

5.2. GJ 234 AB

Our modeling of GJ 234 AB included astrometry measurements from both FGS 3 and FGS 1r. Treating GJ 234 AB as a single-lined spectroscopic binary (due to the large $\Delta V = 3.08$ value), we obtained velocities from the CE for component A at most orbital phases, as seen in Figure 8, right. Modeling included RVs for the A component and astrometry with five reference stars and only four plate parameters. Most of the POS mode observations were secured at one-year intervals, very poorly sampling the parallactic ellipse, with only one POS measurement at the other extreme of the parallactic ellipse, so we used a *Hipparcos* parallax as a prior. We obtained 11 TRANS observations of the separation and position angle for AB and seven POS observations of component A and the reference frame.

Our observations have reduced the parallax error by a factor of 7–10 compared to YPC and *Hipparcos*. Table 9 contains the GJ 234 AB orbital parameters with formal (1σ) uncertainties, with both a and P now known to better than 0.2%. The left panel of Figure 8 illustrates component A and B orbits with the observed positions indicated. The POS-mode component-A residuals and the TRANS residuals are all smaller than the dots and circles. We obtain masses of $\mathcal{M}_A = 0.223 \pm 0.002 \, \mathcal{M}_\odot$ (0.9% error) and
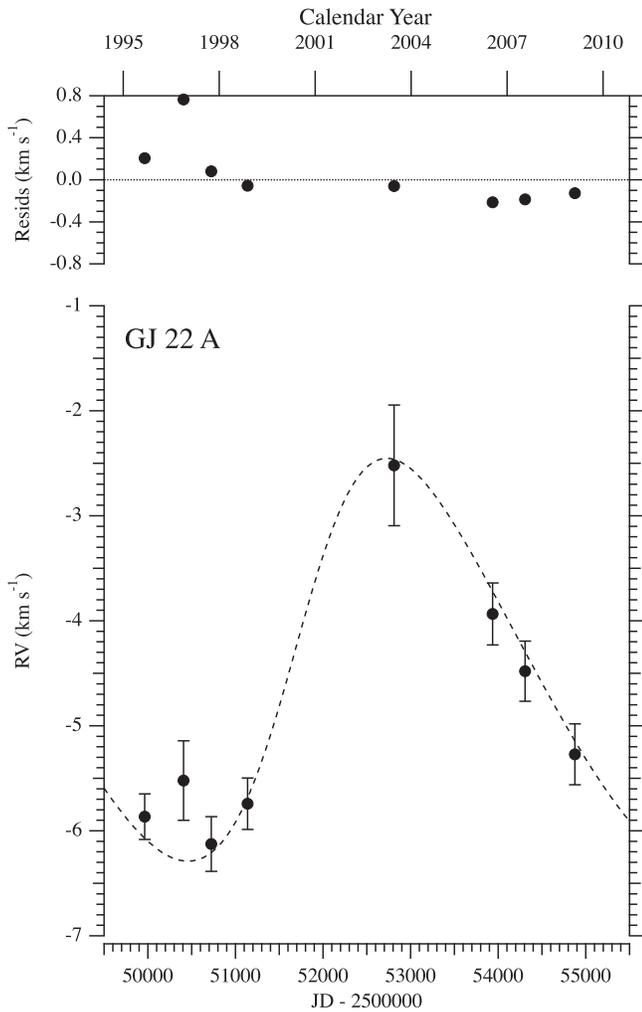
Figure 7. GJ 22 A radial velocities used to derive the orbital elements listed in Table 9 plotted against mJD rather than orbital phase. GJ 22 AC has a companion, GJ 22 B, separated by 4″, with a period $P \simeq 320$ years. We may be detecting that motion as a slope in the RV residuals (top panel).

$\mathcal{M}_B = 0.109 \pm 0.001\,\mathcal{M}_\odot$ (0.9%). These are among the best mass measurements known for red dwarfs, rivaling accuracies for components in eclipsing systems. These masses are larger than those reported by Probst (1977), $\mathcal{M}_A = 0.13 \pm 0.04\,\mathcal{M}_\odot$ (31%) and $\mathcal{M}_B = 0.07 \pm 0.02\,\mathcal{M}_\odot$ (29%), who summarized much of the early work on this important binary. Our new masses are larger than but consistent with those of Coppenbarger et al. (1994), who found $\mathcal{M}_A = 0.179 \pm 0.047\,\mathcal{M}_\odot$ (26%) and $\mathcal{M}_B = 0.083 \pm 0.023\,\mathcal{M}_\odot$ (28%).

5.3. GJ 469 AB

GJ 469 AB astrometric measurements came from FGS 3 and FGS 1r, and RVs came from the CE. Modeling was identical to that used for GJ 831 AB, although the astrometric reference frame included only three stars. Hence, we included a *Hipparcos* parallax (van Leeuwen et al. 2007) as a prior.

The FGS measurements have improved our knowledge of GJ 469 AB's absolute parallax by a factor of 8–13 compared to YPC and *Hipparcos*. Table 9 contains the system's orbital parameters and formal (1σ) uncertainties, with the largest error, 0.3%, in the semimajor axis. Figure 9, left, illustrates component A and B orbits, with effectively complete coverage

of the orbit for the TRANS observations. The POS-mode component-A residuals and the TRANS residuals (component A–B separations) are all smaller than the dots. Figure 9, right, shows the RV measurements, residuals, and velocity curves predicted from the simultaneous solution. We obtain component masses of $\mathcal{M}_A = 0.332 \pm 0.007\,\mathcal{M}_\odot$ (2.4% error) and $\mathcal{M}_B = 0.188 \pm 0.004\,\mathcal{M}_\odot$ (2.7%) listed in Table 10. These are the first mass determinations for this system.

5.4. GJ 623 AB

Our modeling of the challenging GJ 623 AB system included three sources of astrometry and two sources of RVs. With $\Delta V = 5.3$, GJ 623 AB is an extremely difficult system for *HST* TRANS-mode observations; our campaign yielded only two usable measurements. Fortunately, in addition to the *HST* POS and TRANS astrometric observations, there are six aperture masking observations from Martinache et al. (2007) and a single *HST*/FOS observation (Barbieri et al. 1996) available that were included in our modeling. Figure 10, left, illustrates the orbital phase coverage contributions of the three astrometric sources. The inclusion of ground-based relative orbit observations greatly increased the number of measurements of position angle and separation and the time span over which to establish orbital elements. Treating GJ 623 AB as a single-lined spectroscopic binary, we obtained from the CE and from the HET (Endl et al. 2006) velocities for component A at most orbital phases, as shown in the right panel of Figure 10. In addition to including velocities only for component A, we modeled GJ 623 AB (and five reference stars, all observed at each of the 13 POS mode epochs of observation) with six plate coefficients, replacing $-B$ with D and A with E in Equation (6), thereby allowing unequal scales along each axis. The addition of two additional coefficients reduced the ratio of χ^2 to degrees of freedom by 47%, to near unity.

We have improved our knowledge of the parallax of GJ 623 AB by a factor of four compared to *Hipparcos*, and by over a factor of 10 compared to the YPC. Table 9 contains the GJ 623 AB orbital parameters with formal (1σ) uncertainties, with the semimajor axis now known to 0.6%. We obtain component masses of $\mathcal{M}_A = 0.379 \pm 0.007\,\mathcal{M}_\odot$ (1.8% error) and $\mathcal{M}_B = 0.114 \pm 0.002\,\mathcal{M}_\odot$ (1.8%). We have improved upon the previous results of Martinache et al. (2007), who found $\mathcal{M}_A = 0.371 \pm 0.015\,\mathcal{M}_\odot$ (4.0%) and $\mathcal{M}_B = 0.115 \pm 0.002\,\mathcal{M}_\odot$ (1.7%), and the first masses measured by McCarthy & Henry (1987), $\mathcal{M}_A = 0.51 \pm 0.16\,\mathcal{M}_\odot$ (31%) and $\mathcal{M}_B = 0.11 \pm 0.029\,\mathcal{M}_\odot$ (26%), which provided a breakthrough in infrared speckle imaging sensitivity at the time.

5.5. GJ 748 AB

The binary GJ 748 AB was the first system with a relative orbit determined using the *HST* FGSs Franz et al. (1998). The system was subsequently analyzed for mass determinations in Benedict et al. (2001), and we revisit GJ 748 AB here for several reasons. We have an additional TRANS observation obtained with FGS 1r to add to the previous observations secured with FGS 3, extending our coverage by 12 years. This reduces the uncertainty in the orbital period modestly, from 0.5 to 0.3 day. The OFAD has improved from that applied in 2000, and we now use all reference-star POS measurements; the previous study discarded any reference star not observed at each epoch, while the present analysis averages four reference
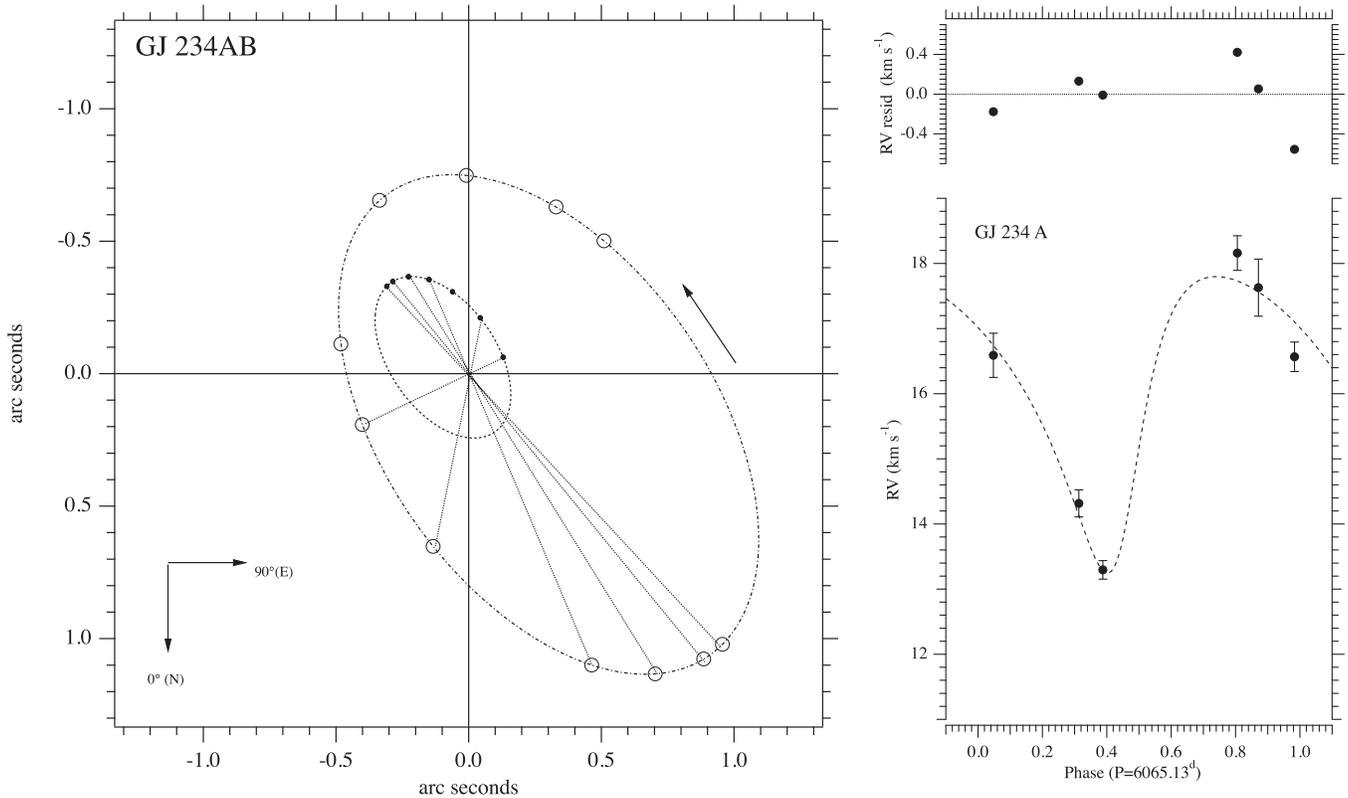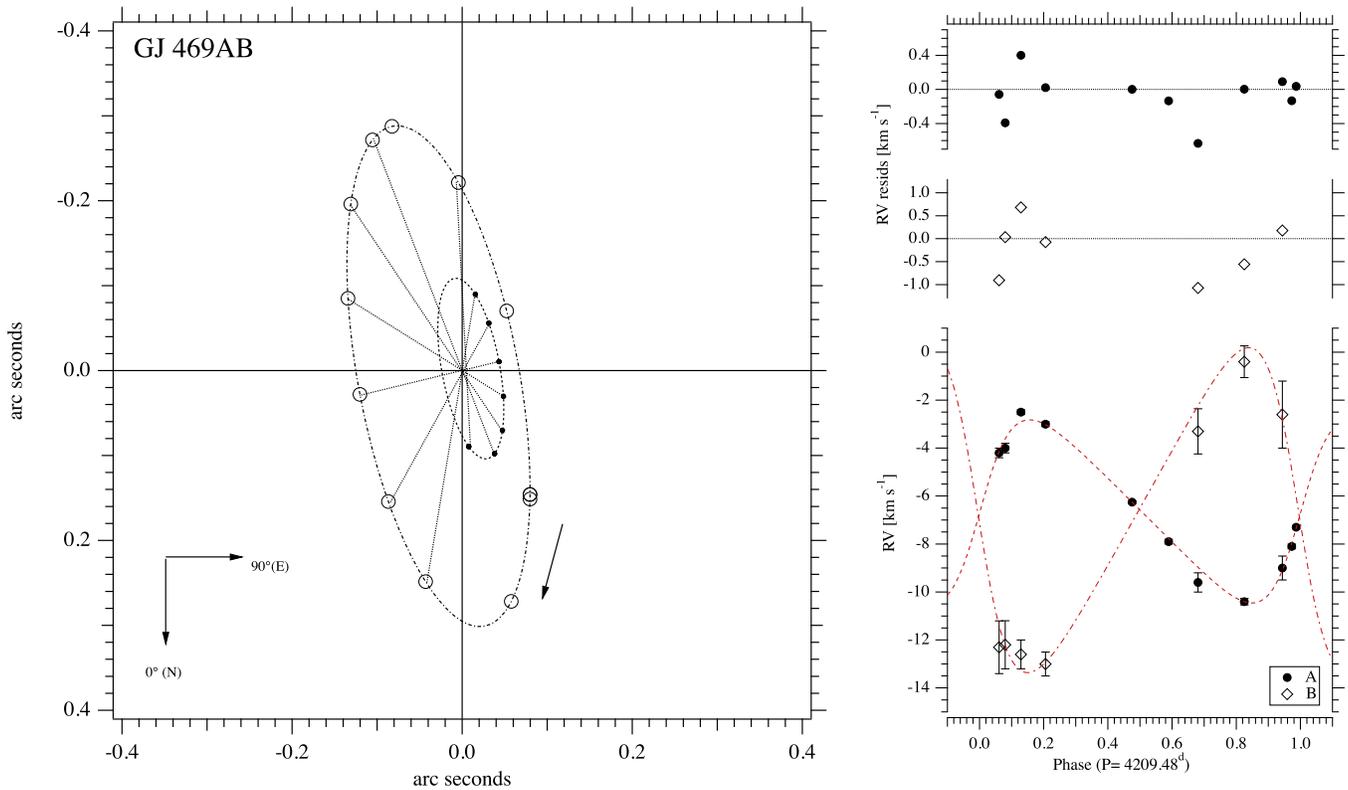
Figure 8. Left: GJ 234 A (dots) POS orbit predicted positions and component B (open circles) TRANS orbit predicted positions. All observations, POS, TRANS, and component-A radial velocities were used to derive the orbital elements listed in Table 9. POS and TRANS astrometric residuals are smaller than the symbols. Right: component-A RV measurements from the present study using CE on the McDonald 2.1 m, phased to the orbital period determined from a combined solution including astrometry and RV. The error bars are 1σ. The dashed line is the velocity predicted from the orbital parameters derived in the combined solution. Top panel: component-A RV residuals (average absolute values, listed in Table 4) from the combined solution.

stars per epoch. The primary RV source remains Benedict et al. (2001), although we add a single new epoch. Finally, we now apply our quasi-Bayesian modeling technique to these data.

We have improved our knowledge of the parallax by a factor of 8–10 compared to YPC and *Hipparcos*. We note that the revised proper motion now agrees more closely with *Hipparcos*. Table 9 contains the GJ 748 AB orbital parameters with formal (1σ) uncertainties, and we find that the parameters are consistent with the orbit in Benedict et al. (2001), as expected. Figure 11, left, provides the component A and B orbits, in which the POS-mode component-A residuals and the TRANS residuals (component A–B separations) are all smaller than the dots. Figure 11, right, contains all RV measurements, RV residuals, and velocity curves predicted from the simultaneous solution. We obtain component masses of $\mathcal{M}_A = 0.369 \pm 0.005\,\mathcal{M}_\odot$ (1.3% error) and $\mathcal{M}_B = 0.190 \pm 0.003\,\mathcal{M}_\odot$ (1.6%). The previous result (Benedict et al. 2001) had slightly higher masses and similar errors: $\mathcal{M}_A = 0.379 \pm 0.005\,\mathcal{M}_\odot$ and $\mathcal{M}_B = 0.192 \pm 0.003\,\mathcal{M}_\odot$.

5.6. GJ 791.2 AB

We also reanalyze GJ 791.2 AB, previously investigated in Benedict et al. (2000). Our motivations, similar to those for GJ 748 AB, now include a set of Hα RVs for both components. With system total magnitude $V = 13.06$ and $\Delta V = 3.27$, detecting both components of GJ 791.2 AB in both the RV data and with *HST*/FGS is difficult. In addition, GJ 791.2 AB is a rapid rotator (Delfosse et al. 1998), further hindering RV efforts. However, both components exhibit strong Hα emission, permitting RV

determination for each component, although with less precision ($0.7\,\mathrm{km\,s^{-1}}$) than for our other systems with RVs (typically $0.3\,\mathrm{km\,s^{-1}}$). We also now have two additional TRANS observations and an additional epoch of POS measurements. All but the last set of POS astrometric measurements came from FGS 3; the last is from FGS 1r. Modeling is exactly as for GJ 831 AB.

This reanalysis has improved our knowledge of the parallax of GJ 791.2 AB by 30% compared to our previous effort, and by a factor of 10 versus the YPC. The new analysis, incorporating priors rather than relying on a correction to absolute derived from a Galactic model, has increased the accuracy of the parallax. Table 9 contains the GJ 791.2 AB orbital parameters with formal (1σ) uncertainties with an error of 0.5% in the semimajor axis, which is 5 mas smaller than in Benedict et al. (2000). The derived orbital period is unchanged. Figure 12, left, provides the component A and B orbits, in which the POS-mode component-A residuals and the TRANS residuals (component A–B separations) are all smaller than the dots. Figure 12, right, contains all Hα RV measurements, RV residuals, and velocity curves predicted from the simultaneous solution. We obtain component masses of $\mathcal{M}_A = 0.237 \pm 0.004\,\mathcal{M}_\odot$ (1.7% error) and $\mathcal{M}_B = 0.114 \pm 0.002\,\mathcal{M}_\odot$ (1.8%). The previous analysis (Benedict et al. 2000) yielded significantly higher masses, $\mathcal{M}_A = 0.286 \pm 0.006\,\mathcal{M}_\odot$ and $\mathcal{M}_B = 0.126 \pm 0.003\,\mathcal{M}_\odot$, which placed both components far from other stars in the MLR. The new masses, due to a smaller orbital semimajor axis, bring the components of GJ 791.2 closer to the MLR defined by the ensemble of system components (Section 8, below).
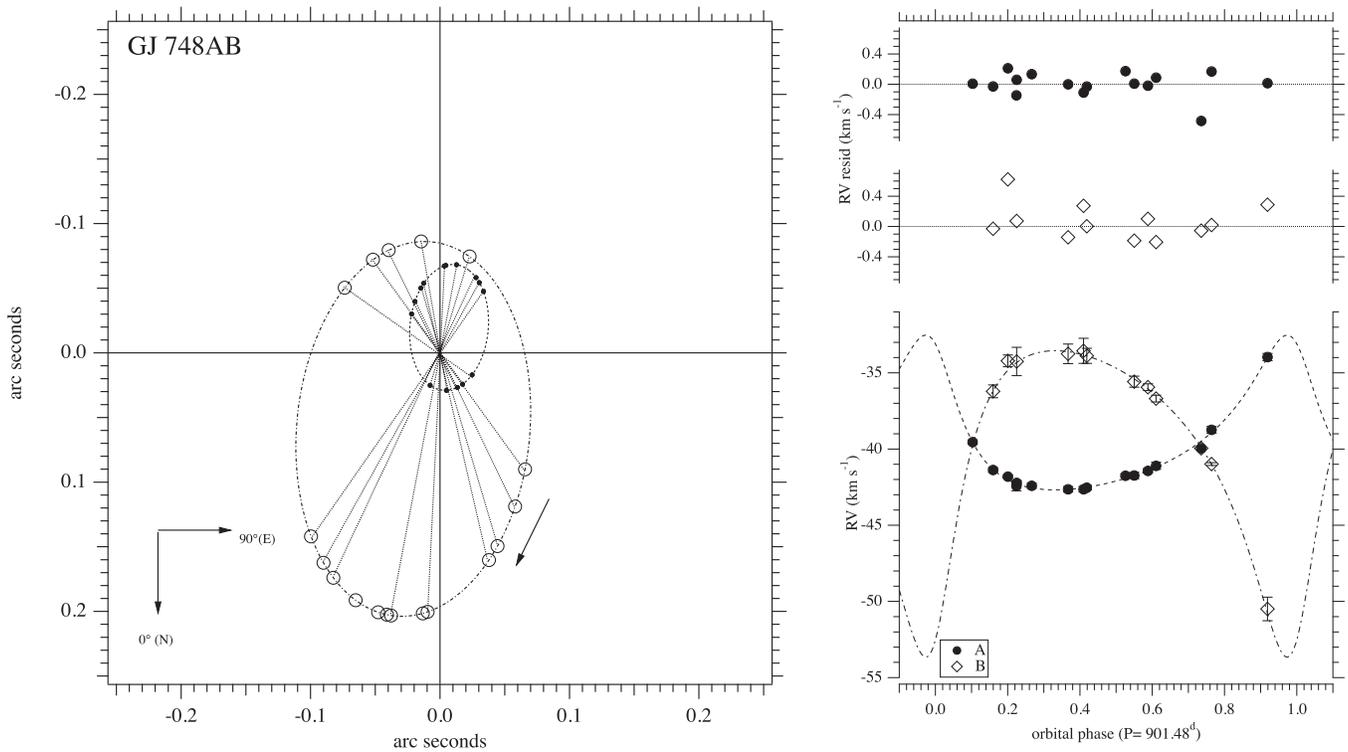
Figure 9. Left: GJ 469 A (dots) POS orbit predicted positions and component B (open circles) TRANS orbit predicted positions. All observations, POS and TRANS and A and B component radial velocities, were used to derive the orbital elements listed in Table 9. POS and TRANS astrometric residuals (average absolute values listed in Table 6) are smaller than the symbols. Right: RV measurements from the present study using CE on the McDonald 2.1 m, phased to the orbital period determined from a combined solution including astrometry and RVs. The error bars are 1σ. The dashed lines are velocities predicted from the orbital parameters derived in the combined solution. Middle and top panels: Component B and A RV residuals (average absolute values listed in Table 4) from the combined solution.

5.7. GJ 1005 AB

We have chosen to reanalyze these data, originally collected and analyzed by Hershey & Taff (1998), with the hope that our Bayesian approach might offer some small improvement. Hershey & Taff (1998) obtained component masses of $\mathcal{M}_A = 0.179 \pm 0.003\,\mathcal{M}_\odot$ and $\mathcal{M}_B = 0.112 \pm 0.002\,\mathcal{M}_\odot$, a precision difficult to improve upon.

We have no RVs for this system, nor for any of the remaining systems discussed below. All *HST* astrometric observations, POS and TRANS, were made using FGS 3. The parallactic ellipse is well sampled, as is the component A–B separation with 17 TRANS observations. The component-A orbit is somewhat less well sampled, but better than, for example, GJ 22 AC. The major difference in modeling, compared to GJ 831 AB, involves the number of plate coefficients. The reference frame consists of only two stars. Consequently, we replace the coefficients A and B in Equations (5) and (6) with $\cos(A)$ and $\sin(A)$, where A is a rotation angle. In essence we assume the scale given by our improved OFAD, just as done by Hershey & Taff (1998) with an older OFAD. The average absolute-value residuals for the POS and TRANS observations of GJ 1005 AB given in Table 6 are ∼1 mas, indicating adequate astrometry even with only three coefficients.

Our parallax agrees almost perfectly with the Hershey & Taff (1998) value, but our approach has improved the precision by a factor of four and represents a vast improvement by factors of ∼20–30 over the YPC and *Hipparcos* values. Table 9 contains the GJ 1005 AB orbital parameters with formal (1σ)

uncertainties, with both a and P now known to 0.2%. Figure 13 provides component A and B orbits with the observed positions indicated. The POS-mode component-A residuals and the TRANS residuals (component A–B separations) are all smaller than the dots and circles in Figure 13. We obtain masses of $\mathcal{M}_A = 0.179 \pm 0.002\,\mathcal{M}_\odot$ (1.1% error) and $\mathcal{M}_B = 0.112 \pm 0.001\,\mathcal{M}_\odot$ (0.9%), values that are virtually identical to and with errors slightly smaller than reported in Hershey & Taff (1998).

5.8. GJ 1245 AC

The GJ 1245 system is a triple, consisting of components A, B, and C, with three components near the end of the stellar main sequence. Our modeling of GJ 1245 AC included six *HST* POS and 10 TRANS astrometric measurements from FGS 3 and FGS 1r and two observations from WFPC2 (Schultz et al. 1998). The POS-mode epochs of observations included seven reference stars and were secured at one-year intervals, again very poorly sampling the parallactic ellipse and sampling less than half the component-A orbit (Figure 14). Consequently, we included a YPC parallax as a prior. Note that the parallax error (0.5 mas, Table 7) is larger than for a typical *HST* parallax, due to the less-than-ideal sampling. Even though all epochs sampled almost exactly the same part of the parallactic ellipse, they serve to scale the size of that ellipse well enough to provide a parallax whose error does not adversely affect the determination of the final masses. In our final solution, we obtain a parallax error that is half as large as the YPC parallax used as a prior.
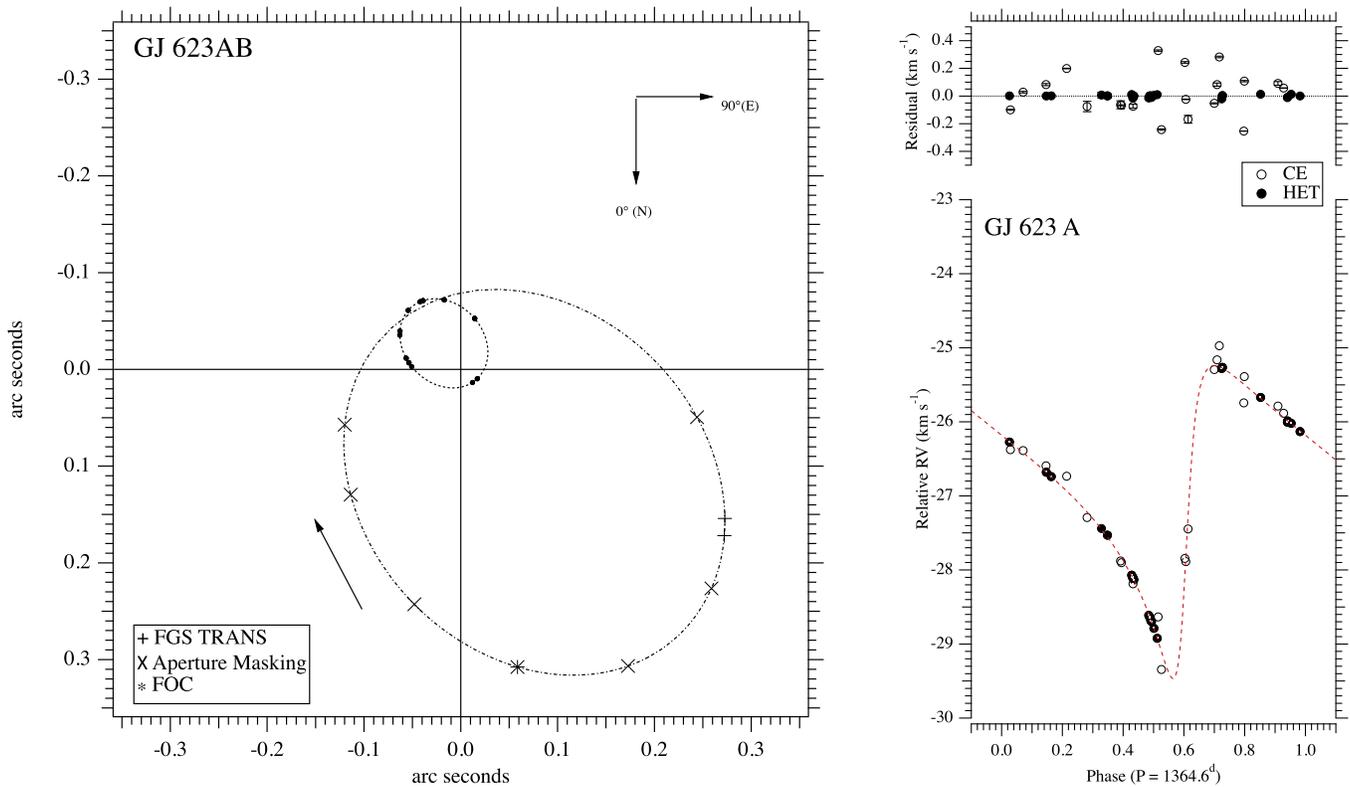
Figure 10. Left: GJ 623 A (dots) POS orbit predicted positions and component B (+) TRANS, FOC (*) (Barbieri et al. 1996), and ($\times$) aperture masking (Martinache et al. 2007) orbit predicted positions. All observations, POS, TRANS, FOC, aperture masking, and component-A radial velocities, were used to derive the orbital elements listed in Table 9. POS, TRANS, FOC, and aperture masking astrometric residuals (rms for which are listed in Table 6) are smaller than the symbols. Right: component-A RV measurements from the present study using CE on the McDonald 2.1 m and the Tull Spectrograph on HET, phased to the orbital period determined from a combined solution including astrometry and RVs. The dashed lines are velocities predicted from the orbital parameters derived in the combined solution. Top panel: component-A RV residuals (average absolute values, CE and HET, listed in Table 4) from the combined solution. We plot 1σ error bars in this case on the residuals. They are smaller than the points in the lower panel.

The 10 TRANS-mode data points sample three-quarters of the relative orbit and nicely map the component A–C separations and position angles over time, as shown in Figure 14. The POS-mode component-A residuals and the TRANS residuals (component A–C separations) are all smaller than the dots and circles. We obtain masses of $\mathcal{M}_A = 0.111 \pm 0.001\,\mathcal{M}_\odot$ (0.9% error) and $\mathcal{M}_C = 0.076 \pm 0.001\,\mathcal{M}_\odot$ (1.3%). These masses are consistent with the first detailed study of the system by McCarthy et al. (1988), who found $\mathcal{M}_A = 0.14 \pm 0.03\,\mathcal{M}_\odot$ (21%) and $\mathcal{M}_C = 0.10 \pm 0.02\,\mathcal{M}_\odot$ (20%).

These are among the best red dwarf masses yet determined, which is important because component C has the lowest mass of any object in this study. Its mass corresponds to $79.8 \pm 1.0\,\mathcal{M}_{\rm Jup}$, placing it at the generally accepted main-sequence hydrogen-burning demarcation boundary of $\sim$80 $\mathcal{M}_{\rm Jup}$ (Dieterich et al. 2014 and references therein). In addition, *Kepler* has collected extensive photometric data. Astrometry carried out with these data (Lurie et al. 2015) is consistent with our GJ 1245 AC orbit and may have detected AC–B motion.

5.9. G 250-029 AB

All astrometric measurements came from *HST*/FGS 3 and FGS 1r. The eight POS measurements contain only three reference stars but sample the parallactic ellipse better than for GJ 1245 AC, although not well enough to preclude the introduction of a lower-precision parallax prior from *Hipparcos* as a

prior. Fourteen TRANS observations of the component A–B separations sample nearly the entire orbit (Figure 15).

Our parallax agrees with the *Hipparcos* value but has reduced the error by a factor of eight, and it represents a factor of 16 improvement over the value in YPC. Figure 15 provides component A and B orbits with the observed positions indicated. Again, the POS-mode component-A residuals and the TRANS residuals (component A–B separations) are all smaller than the dots and circles in the figure. We obtain masses of $\mathcal{M}_A = 0.350 \pm 0.005\,\mathcal{M}_\odot$ (1.7% error) and $\mathcal{M}_B = 0.187 \pm 0.004\,\mathcal{M}_\odot$ (2.2%). These are the first mass determinations for this system.

5.10. GJ 1081 AB

Our modeling of GJ 1081 AB included only *HST* POS and TRANS astrometric observations made using FGS 1r. The five epochs of POS-mode observations had six reference stars and were secured at one-year intervals, very poorly sampling the parallactic ellipse. Hence, we included a parallax from the YPC as a prior. The POS observations sparsely sample the perturbation of the primary, while the 11 TRANS observations nicely map the entire relative orbit (Figure 16).

Our parallax agrees with the YPC value, but our precision has reduced the parallax error of GJ 1081 AB by a factor of four. Figure 16 provides component A and B orbits with the observed positions indicated, where the POS and TRANS residuals are smaller than the dots and circles in the figure. Because of the
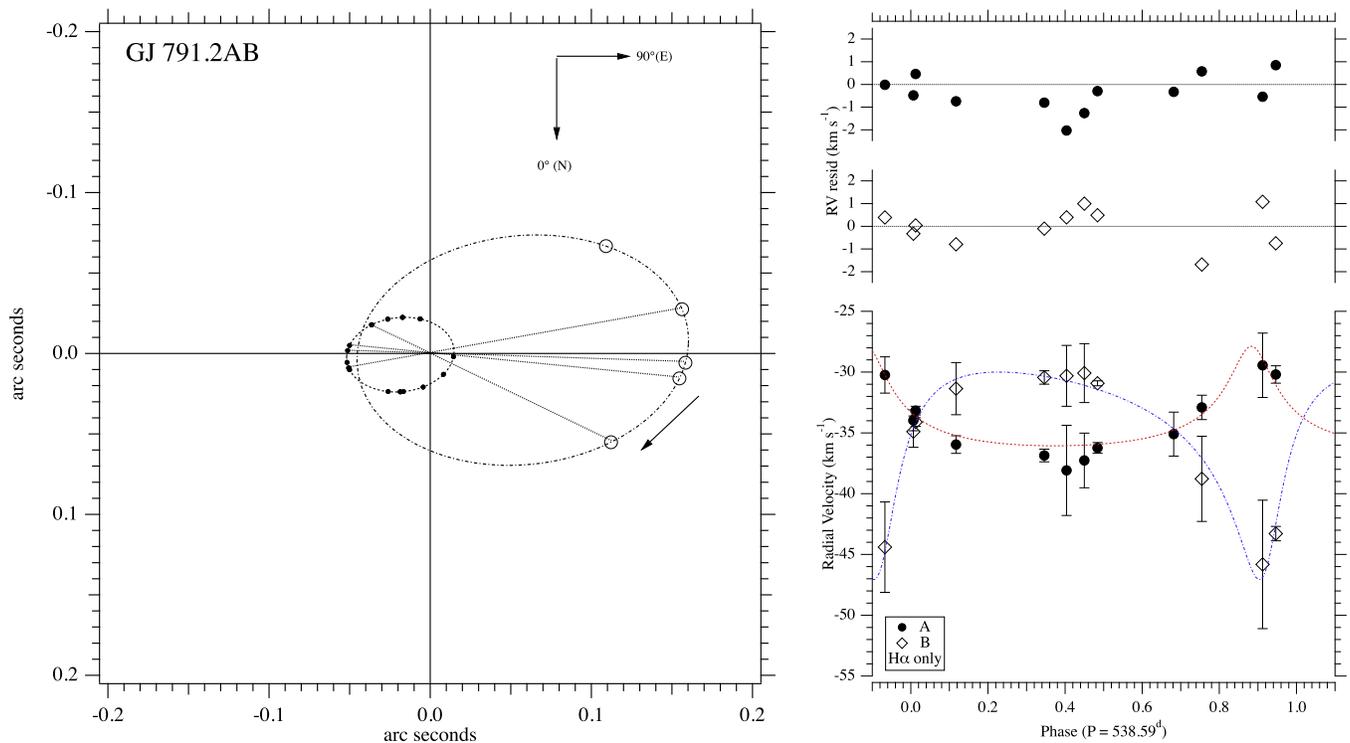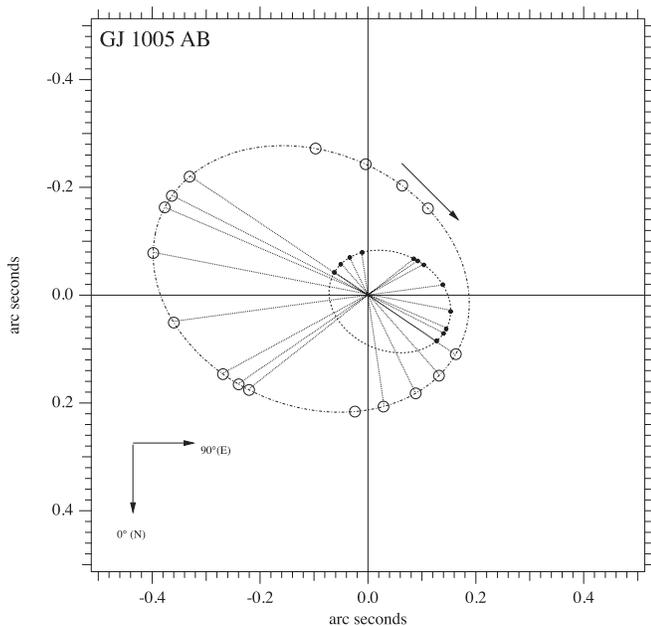
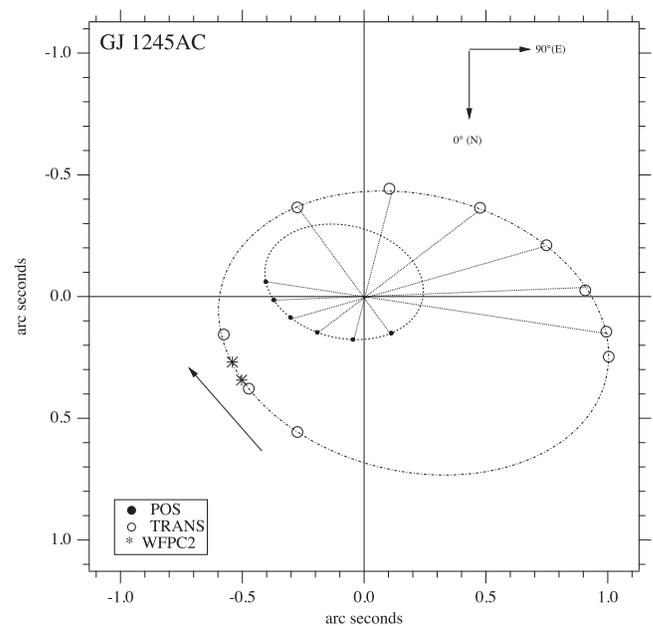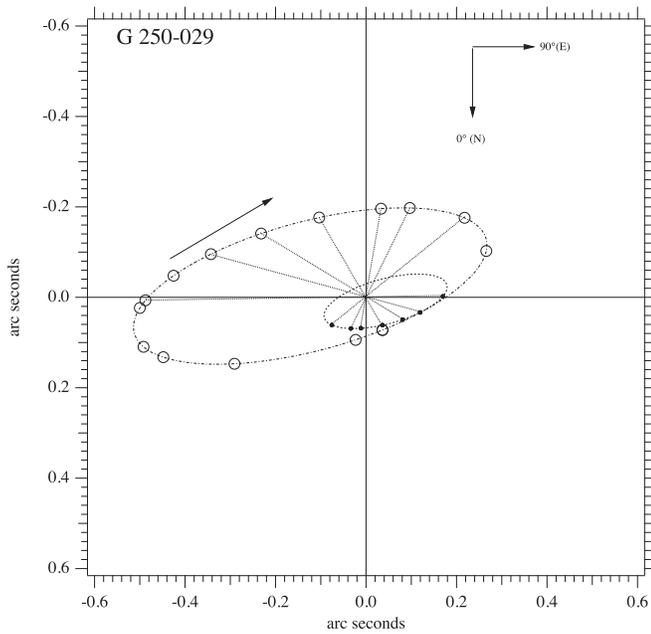**Figure 11.** Left: GJ 748 A (dots) POS orbit predicted positions and component B (open circles) TRANS orbit predicted positions. All observations, POS and TRANS and A and B component radial velocities, were used to derive the orbital elements listed in Table 9. POS and TRANS astrometric residuals (average absolute values for which are listed in Table 6) are smaller than the symbols. Right: RV measurements from the present study using CE on the McDonald 2.1 m, phased to the orbital period determined from a combined solution including astrometry and RVs. The error bars are 1σ. The dashed lines are velocities predicted from the orbital parameters derived in the combined solution. Middle and top panels: component B and A RV residuals (average absolute values for which are listed in Table 4) from the combined solution. The four component-B velocities with errors larger than 0.5 km s^{-1} come from Marcy & Benitz (1989).

high orbital inclination and paucity of POS observations, we obtain relatively poor mass precision for this system. We find component masses of $\mathcal{M}_A = 0.325 \pm 0.010\ \mathcal{M}_\odot$ (3.2% error) and $\mathcal{M}_B = 0.205 \pm 0.007\ \mathcal{M}_\odot$ (3.4%). These are the first mass determinations for this system.

5.11. GJ 54 AB

GJ 54 AB has the shortest orbital period in our sample, with a period of 1.15 year. Our modeling of GJ 54 AB included *HST* POS (with three reference stars) and TRANS from FGS 1r and one NICMOS astrometric measurement (Golimowski et al. 2004). Again, the timing of the six epochs of POS-mode observations sparsely sampled the parallactic ellipse, so we included a *Hipparcos* parallax prior. The eight TRANS observations sample the entire relative orbit (Figure 17), and the NICMOS measurement falls squarely between the two TRANS observations on the orbit, although it occurs nearly two years before the first FGS 1r observation.

Our derived parallax is larger than the *Hipparcos* value and has an error six times smaller. *Hipparcos* likely struggled to measure an accurate value because the orbital period is so close to the 1.00 year periodicity of the tracing of the parallax ellipse; without knowledge of the resolved positions of the two stars in the binary, an accurate parallax determination is a challenge. Figure 17 provides the component A and B orbits with the observed positions indicated. The model yields component masses of $\mathcal{M}_A = 0.432 \pm 0.008\ \mathcal{M}_\odot$ (2.0% error) and $\mathcal{M}_B = 0.301 \pm 0.006\ \mathcal{M}_\odot$ (2.0%). These are the first mass determinations for this system.

5.12. G 193-027 AB

Our modeling of G 193-027 AB included *HST* POS and TRANS from FGS 1r, one AO observation (Beuzit et al. 2004), and one NICMOS astrometric measurement (Golimowski et al. 2004). The POS-mode observations included five reference stars, and most of the six epochs were secured at one-year intervals, very poorly sampling the parallactic ellipse. Hence, we initially included a parallax from Khrutskaya et al. (2010) as a prior, although that parallax had no correction from relative to absolute parallax. Ultimately, the χ^2 markedly decreased when we removed that low-precision and perhaps inaccurate prior.

Because of the typical large component separation (100–170 mas) and small $\Delta V = 0.30$, the POS observations half the time locked on component B instead of component A. We modified our model to deal with this complication by constraining the parallax of component A to equal the parallax of B and by solving for two POS-mode orbits. In Figure 18 we plot observation-set numbers on the component-A orbit that should have been established for the six sets of POS measurements; the POS observations sparsely sample the perturbation of the primary because they locked on component B for sets 2, 3, and 4. The relatively large parallax error of 1.4 mas (Table 7) reflects the paucity of POS-mode observations.

Table 9 contains the G 193-027 AB orbital parameters from a model not including the Khrutskaya et al. (2010) parallax prior. Figure 18 provides component A and B orbits with the observed positions indicated. Because we had relatively few component-A POS observations, we obtain somewhat poorer mass precision
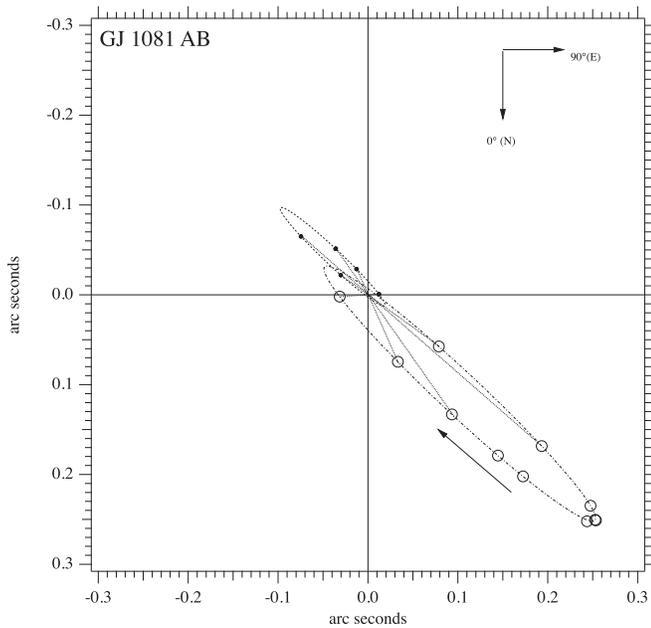
Figure 12. Left: GJ 791.2 A (dots) POS orbit predicted positions and component B (open circles) TRANS orbit predicted positions. All observations, POS and TRANS and A and B component radial velocities (from Hα emission lines only), were used to derive the orbital elements listed in Table 9. POS and TRANS astrometric residuals (average absolute values for which are listed in Table 6) are smaller than the symbols. Right: RV measurements of the Hα emission lines from the present study using CE on the McDonald 2.1 m, phased to the orbital period determined from a combined solution including astrometry and RVs. The error bars are 1σ. The dashed lines are velocities predicted from the orbital parameters derived in the combined solution. Middle and top panels: component B and A RV residuals (average absolute values for which are listed in Table 4) from the combined solution. Note that the less massive component B has stronger Hα emission, resulting in slightly smaller RV residuals for B (0.66 km s^{-1}) than for component A (0.70 km s^{-1}).

Figure 13. GJ 1005 A (dots) POS orbit predicted positions and component B (open circles) TRANS orbit predicted positions. All observations were used to derive the orbital elements listed in Table 9. Component B TRANS and component A POS astrometric residuals (average absolute values for which are listed in Table 6) are smaller than their symbols.

Figure 14. GJ 1245 A (dots), POS orbit predicted positions; WFPC2 (*) and component C (open circles) TRANS orbit predicted positions. All observations were used to derive the orbital elements listed in Table 9. Component-C TRANS and component-A POS astrometric residuals (average absolute values for which are listed in Table 6) are smaller than their symbols.

Figure 15. G 250-029 A (dots) POS orbit predicted positions and component B (open circles) TRANS orbit predicted positions. All observations were used to derive the orbital elements listed in Table 9. Component-B TRANS and component-A POS astrometric residuals (average absolute values for which are listed in Table 6) are smaller than their symbols.
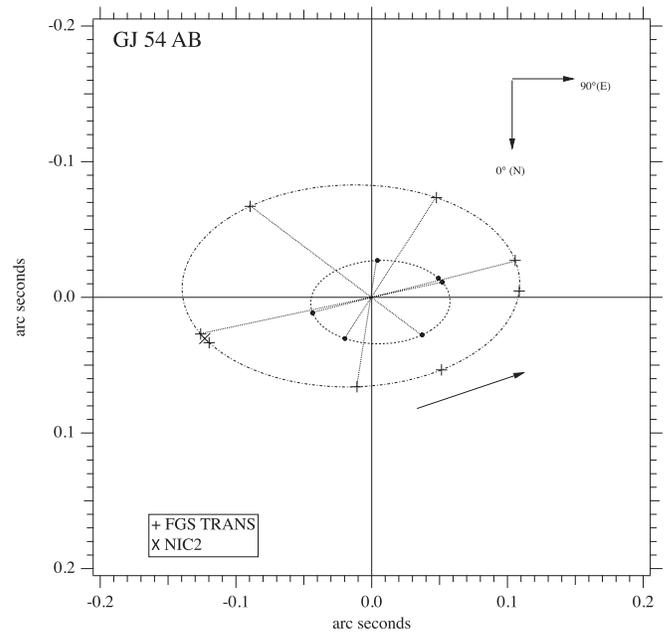
Figure 17. GJ 54 A (dots) POS orbit predicted positions and component B (+) TRANS orbit predicted positions. The solution included one *HST* NICMOS observation (×). All observations were used to derive the orbital elements listed in Table 9. Component-B (TRANS and NICMOS) and component-A POS astrometric residuals (average absolute values for which are listed in Table 6) are smaller than their symbols.

Figure 16. GJ 1081 A (dots) POS orbit predicted positions and component B (open circles) TRANS orbit predicted positions. All observations were used to derive the orbital elements listed in Table 9. Component-B TRANS and component-A POS astrometric residuals (average absolute values for which are listed in Table 6) are smaller than their symbols.
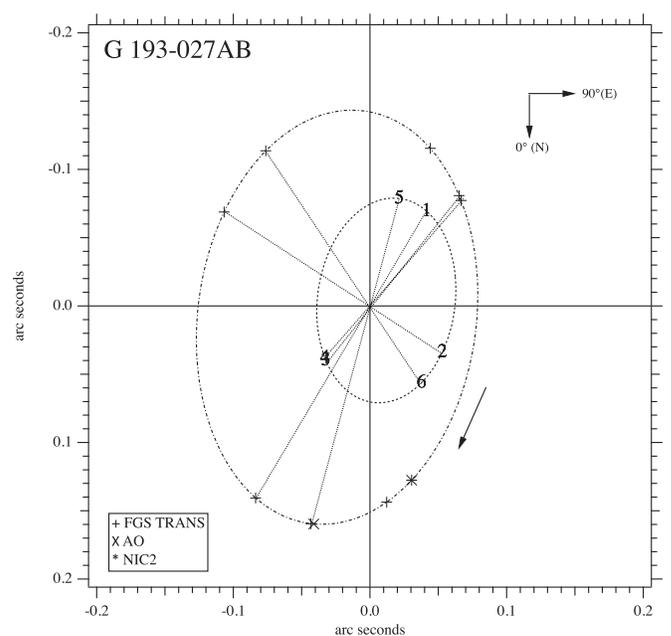
Figure 18. G 193-027 A (numbers) POS orbit predicted positions and component B TRANS (+), AO (×), and NICMOS (*) orbit predicted positions. POS, which normally provides astrometry for component A, locked onto component B for sets 2, 3, and 4. All observations were used to derive the orbital elements listed in Table 9. Component B (TRANS, AO, and NICMOS) and component A and B POS astrometric residuals (average absolute values for which are listed in Table 6) are smaller than their symbols.

for this system, finding $\mathcal{M}_A = 0.126 \pm 0.005 \, \mathcal{M}_\odot$ (4.0% error) and $\mathcal{M}_B = 0.124 \pm 0.005 \, \mathcal{M}_\odot$ (4.0%), with the errors driven almost entirely by the parallax error. The two components are of nearly equal mass, consistent with their low ΔV. These are the first mass determinations for this system.

5.13. GJ 65 AB

The 10 *HST* TRANS-only observations were made using FGS 3, covering only 18° of orbital position angle during
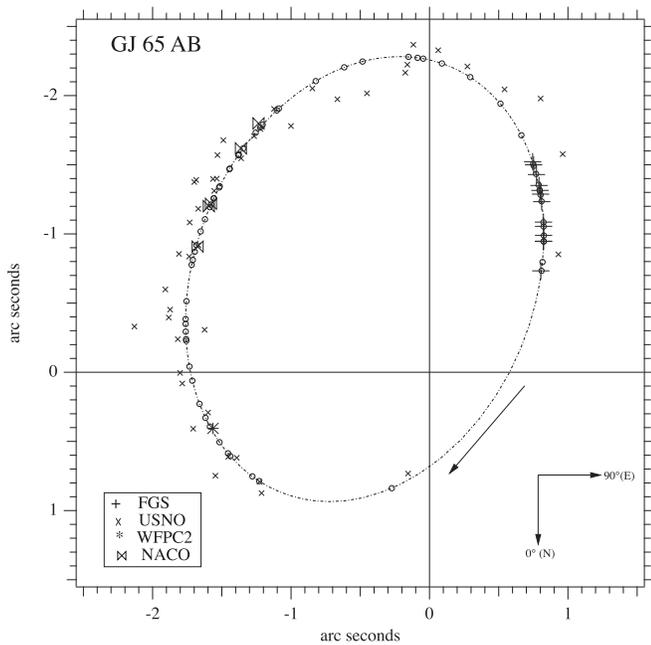
Figure 19. GJ 65 component-B orbit predicted (open circles) and measured positions (identified in the legend) with sizes proportional to the average measurement error. All A–B position angle and separation observations (sources identified in Table 8) were used to derive the orbital elements listed in Table 9. No POS-mode observations entered into the modeling, due to a paucity of reference stars.
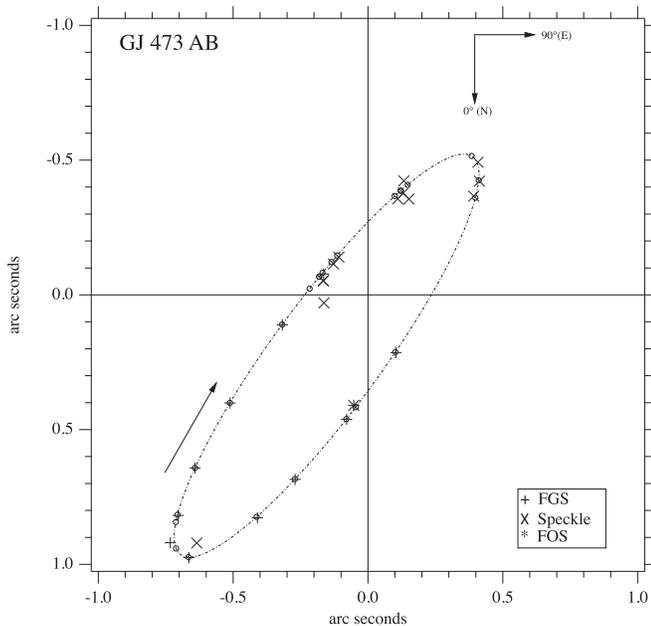
Figure 20. GJ 473 AB relative orbit. Calculated positions are plotted on the orbit as open circles. Measurements from TRANS (+), speckle (×), and HST FOS (*) illustrate the residuals. All observations were used to derive the orbital elements listed in Table 9. No POS-mode observations entered into the modeling.

1.1 year. Seven POS-mode observations exist for component A (shown as dots in Figure 19), but the reference frame consisted of a single star at each epoch, and not always the same single star. Consequently, we model only the relative orbit. We

included a large sample of valuable visual, photographic, and CCD observations of separation and position angle (Geyer et al. 1988) for our analysis of GJ 65 AB. These low-precision (relative to HST) measurements came primarily from the USNO 61 in reflector and span 48 years. Even though of lower precision, they are extremely useful for this system, which has an orbital period of 26.5 years, the longest among the 15 systems we observed with HST/FGS. Also useful for extending the orbit sampling are five VLT/NACO (Kervella et al. 2016) measures and one HST/WFPC2 (Dieterich et al. 2012) measure of position angle and separation.

Modeling only relative position angle and separation measurements yields a, P, T_0, e, i, Ω, and ω_B. Figure 19 provides the component-AB relative orbit with the observed positions indicated. The USNO residuals are obviously not smaller than the circles in the figure. The average absolute-value residual for the HST TRANS observations is $\langle |res| \rangle = 3.5$ mas, considerably smaller than the corresponding 81 mas value for the USNO and 9.6 mas for the VLT/NACO measurements. By adopting a mass fraction ($f = 0.494 \pm 0.004$, Geyer et al. 1988) and absolute parallax ($\pi_{abs} = 373.7 \pm 2.7$ mas) from the YPC, we obtain component masses of $\mathcal{M}_A = 0.120 \pm 0.003 \ \mathcal{M}_\odot$ (2.5% error) and $\mathcal{M}_B = 0.117 \pm 0.003 \ \mathcal{M}_\odot$ (2.5%), agreeing with the recent Kervella et al. (2016) values of $\mathcal{M}_A = 0.123 \pm 0.004 \ \mathcal{M}_\odot$ (3.5% error) and $\mathcal{M}_B = 0.120 \pm 0.004 \ \mathcal{M}_\odot$ (3.6%).

5.14. GJ 473 AB

The sky within the FGS FOV near GJ 473 AB contains no usable POS-mode reference stars. Hence, as with GJ 65 AB, we again model only the relative orbit with astrometry, using several sources: HST (TRANS-only) from FGS 3 and FGS 1r, a single HST FOS measurement (Schultz et al. 1998), and optical (Blazit et al. 1987; Balega et al. 1994; Horch et al. 2012) and near-infrared speckle (Henry et al. 1992 and Torres et al. 1999) observations. These lower-precision (relative to HST) measurements are extremely useful for this long-period (15.8 year) system.

Figure 20 provides the component-AB relative orbit with the observed positions indicated. The speckle residuals are generally not smaller than the circles in the figure. The mean absolute-value residual for the HST TRANS observations is 2.5 mas, considerably smaller than the corresponding 17 mas value for the speckle measurements. By adopting a mass fraction of $f = 0.477 \pm 0.008$ from Torres et al. (1999) and an absolute parallax of $\pi_{abs} = 235.5 \pm 2.9$ mas from the RECONS astrometry program at the CTIO/SMARTS 0.9 m (Henry et al. 2006), we obtain component masses of $\mathcal{M}_A = 0.124 \pm 0.005 \mathcal{M}_\odot$ (4.0% error) and $\mathcal{M}_B = 0.113 \pm 0.005 \ \mathcal{M}_\odot$ (4.1%). The relatively large mass errors are driven almost entirely by the parallax error. These masses are somewhat lower than those reported by Torres et al. (1999), $\mathcal{M}_A = 0.143 \pm 0.011 \ \mathcal{M}_\odot$ (7.7% error) and $\mathcal{M}_B = 0.131 \pm 0.010 \ \mathcal{M}_\odot$ (7.6%), who used 56 astrometry observations taken between 1938 and 1998; however, only four high-quality FGS observations were available then, compared to the 11 FGS observations used here.

6. ABSOLUTE MAGNITUDES

The orbital elements summarized for the 15 systems in Table 9 are used to derive the component masses given in Table 10. To place these stars on an empirical MLR, we also

Table 11
Other Mass Determinations

ID	SpT	π_{abs} [mas]	ref[a]	M_V	M_K	ref[a]	$\mathcal{M}_{\odot}$	ref[a]
GJ 166 C	M4.0V	200.7 ± 0.2	H12	12.68 ± 0.03	7.45 ± 0.03	H12	0.177 ± 0.029	H99
GJ 278 C	M1 V	66.9 0.6	T02	9.01 0.33	5.32 0.01	T10	0.599 0.005	T02
GJ 278 D	⋯	⋯	⋯	9.01 0.33	5.32 0.01	⋯	0.599 0.005	⋯
GJ 570 B	M1.5V	169.8 0.9	F99	9.45 0.05	5.40 0.03	D00	0.586 0.007	F99
GJ 570 C	⋯	⋯	⋯	11.09 0.17	6.58 0.04	F99	0.390 0.005	⋯
GJ 630.1 A	M5 V	69.2 2.5	YPC	12.72 0.02	7.64 0.03	M09	0.231 0.001	M09
GJ 630.1 B	⋯	⋯	⋯	12.86 0.03	7.78 0.03	⋯	0.214 0.001	⋯
GJ 747 A	M3 V	120.2 0.2	S00	12.30 0.06	7.53 0.04	D00	0.214 0.001	S00
GJ 747 B	⋯	⋯	⋯	12.52 0.06	7.63 0.04	⋯	0.200 0.001	⋯
GJ 860 A	M3.0V	249.5 3.0	H99	11.78 0.01	7.03 0.04	H99	0.268 0.020	T06
GJ 860 B	M4.0V	⋯	⋯	13.39 0.01	8.40 0.07	⋯	0.172 0.008	H99
GJ 2005 B	M8.5V	128.49 1.50	C05, *	19.24 0.07	10.48 0.05	L00	0.079 0.020	⋯
GJ 2005 C	M9.0V	⋯	⋯	19.63 0.08	10.83 0.05	⋯	0.079 0.020	⋯
GJ 2069 A	M3.5V	64.80 1.43	*	11.49 0.02	6.29 0.03	R03	0.433 0.002	R03
GJ 2069 C	⋯	⋯	⋯	11.76 0.03	6.55 0.03	⋯	0.398 0.001	⋯
GU Boo A	M0 V	7.5 1.0	L05	8.60 0.17	5.29 0.15	L05	0.616 0.006	L05
GU Boo B	M1.5V	⋯	⋯	8.89 0.18	5.42 0.15	⋯	0.600 0.006	⋯

Note.
[a] Sources: *—this paper, C05—Costa et al. (2005), D00—Delfosse et al. (2000), D15—S. Dieterich (2015, in preparation), F99—Forveille et al. (1999), H12—Holberg et al. (2012), H99—Henry et al. (1999), L00—Leinert et al. (2000), L05—López-Morales & Ribas (2005), M09—Morales et al. (2009), P97—Perryman et al. (1997), R03—Ribas (2003), S00—Ségransan et al. (2000), S08—Seifahrt et al. (2008), T02—Torres & Ribas (2002), T06—Tamazian et al. (2006), YPC—van Altena et al. (1995).

require the component absolute magnitudes. For the MLR at optical wavelengths, we use V photometry from Weis (1984, 1996) and the RECONS program at the CTIO/SMARTS 0.9 m (see Winters et al. 2015). For ΔV, we use values in our earlier work (Henry et al. 1999) as well as results from the FGS observations presented here to derive component magnitudes. The Δm measurements from the FGS TRANS observations using F583W have been transformed to ΔV, as described in Henry et al. (1999).

At infrared wavelengths, we use 2MASS K_s photometry (Skrutskie et al. 2006) for the combined light of all 15 systems in Table 10. The ΔK values have been adopted from infrared speckle measurements previously reported in Henry & McCarthy (1993), *HST*/NICMOS measurements reported in Dieterich et al. (2012), and new Gemini-N observations using the Near InfraRed Imager with the ALTAIR facility level adaptive optics system (S. Dieterich, 2015, in preparation). We have not made any transformations between the infrared K-band filters given that the ΔK measurement errors tend to be larger than the slight adjustments due to differences in the various K filters.

Using our parallaxes in Table 7 and the ΔV and ΔK values, we find the component absolute magnitudes presented in Table 10. For these very nearby systems, we have assumed no absorption ($A_V = 0$). Parallaxes of this precision do not require correction for Lutz–Kelker–Hanson bias (Lutz & Kelker 1973; Hanson 1979) in the derived absolute magnitudes.

7. ADDITIONAL LOW-MASS BINARY SYSTEMS

To boost the number of stars used in the MLRs at both optical and infrared wavelengths, we augment our sample of 15 binaries with red dwarfs in nine additional systems having high-quality mass, M_V, and M_K measurements. In Table 11, we list their parallaxes, V- and K-band absolute magnitudes, and

masses computed by other investigators. Ground-based astrometry has been used for all systems, except the eclipsing binaries GJ 278 CD (YY Gem), GJ 630.1 AB (CM Dra), GJ 2069 AC (CU Cnc), and GU Boo. A few systems are particularly worthy of note:

GJ 166C is a tertiary in the 40 Eri system in a ~250 year orbit with the white dwarf GJ 166B. Hence, the mass error of $0.029\,\mathcal{M}_{\odot}$ is the largest for any star in the sample.

GJ 2005 ABC is an important triple with components near the end of the stellar main sequence. Only a small portion of the A–BC orbit has been observed, so the resulting mass determinations for A are not of sufficiently high quality to be included in this paper; here we concentrate on the BC pair. The three stars have combined $V = 15.28 \pm 0.02$ from our CTIO/SMARTS 0.9 m photometry, and individual ABC magnitudes of $V = 15.35 \pm 0.04$, 18.68 ± 0.06, and 19.07 ± 0.07 from Leinert et al. (2000). In the infrared, $K = 8.24 \pm 0.03$ for ABC from 2MASS. Using $\Delta K_{AB} = 1.20 \pm 0.03$ and $\Delta K_{AC} = 1.55 \pm 0.09$ from Leinert et al. (1994), the components have individual magnitudes of $K_A = 8.73 \pm 0.03$, $K_B = 9.93 \pm 0.04$, and $K_C = 10.28 \pm 0.04$. The weighted mean parallax of 128.49 ± 1.50 mas is from the RECONS astrometry program at the CTIO/SMARTS 1.5 m (129.47 ± 2.48 mas, Costa et al. 2005) and a new value from the CTIO/SMARTS 0.9 m program (127.93 ± 1.88 mas). We adopt the BC orbit and fractional mass (0.48 ± 0.01) from Köhler et al. (2012), with the new parallax to obtain masses of $M_B = 0.079 \pm 0.003\,\mathcal{M}_{\odot}$ and $M_c = 0.073 \pm 0.003\,\mathcal{M}_{\odot}$.

GJ 2069 AC is an eclipsing binary that is part of the quintuple red dwarf system known as CU Cnc (components A, C, and E) and CV Cnc (components B and D). There was no parallax in YPC, and the various parallaxes derived using *Hipparcos* data are of poor quality, with values of 78.05 ± 5.69 (original reduction), 85.16 ± 6.42 mas (Pourbaix et al. 2003), and 90.37 ± 8.22 mas (van Leeuwen et al. 2007). The first parallax
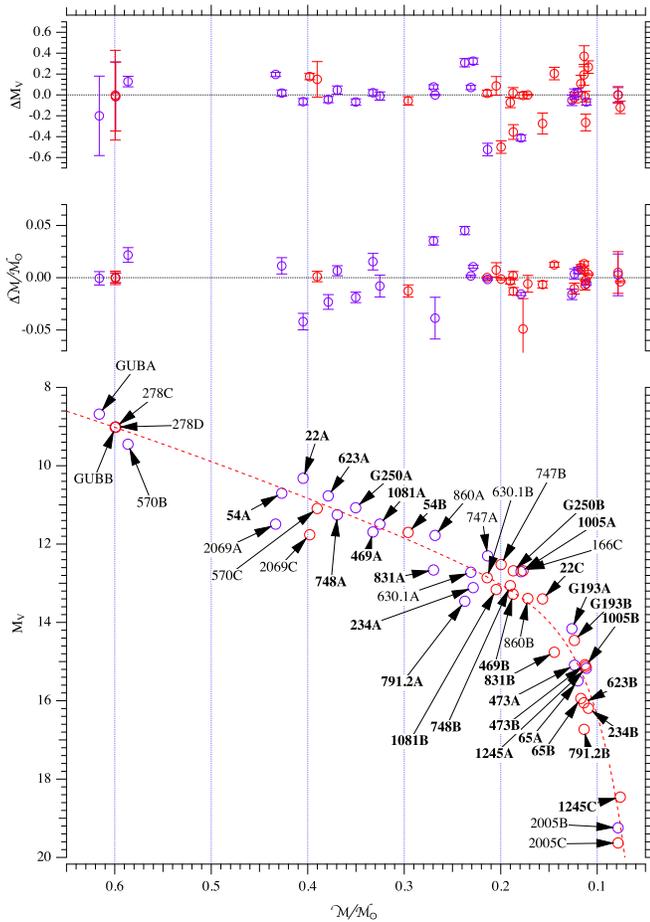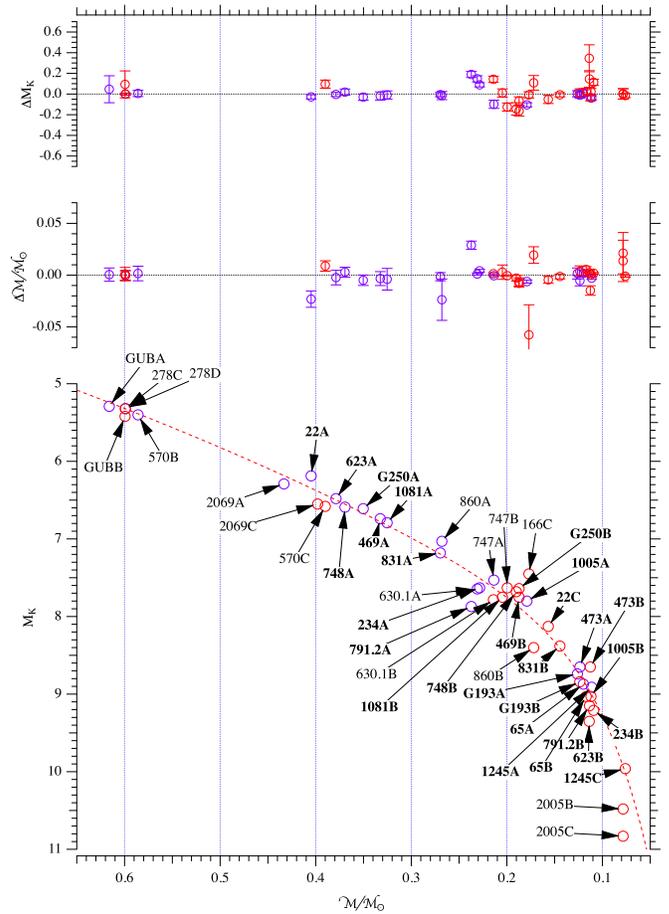
Figure 21. *V*-band MLR. The dashed line is a double exponential function fit (Equation (10)) to masses and M_V. Primaries are in blue; secondaries are in red. M_V and $\mathcal{M}$ residuals show differences between observed values and a fit to Equation (10) using GaussFit. We list fit coefficients and M_V, $\mathcal{M}$ residual rms in Table 12. Errors for M_V and mass are plotted on their respective residual points. Points are GJ numbers without the GJ prefix, except for GU Boo (GUB), G250-029 (G250), and G193-027 (G193). Boldface denotes new or improved masses and absolute magnitudes from this work.

Figure 22. *K*-band MLR. The dashed line is a double exponential function fit (Equation (10)) to masses and M_K. Primaries are in blue; secondaries are in red. M_K and $\mathcal{M}$ residuals show differences between observed values and a fit to Equation (10) using GaussFit. We list fit coefficients and M_K, $\mathcal{M}$ residual rms in Table 12. Errors for M_V and mass are plotted on their respective residual points. Note the marked decrease in residual size. Same point labeling as Figure 21. GJ 54, lacking *K*-band photometry, is not included.

value was used by Delfosse et al. (1999), which led them to conclude that the eclipsing components were subluminous. Here we provide a much better value of 64.80 ± 1.43 mas from the RECONS astrometry program at the CTIO/SMARTS 0.9 m that utilizes 11 years of astrometry data. This represents the weighted mean of values determined for ACE (63.59 ± 1.92 mas) and BD (66.32 ± 2.15 mas); the system is observed as two sources at the resolution of the 0.9 m. With this parallax, the components of the eclipsing pair AC now fall closer to other stars in the MLR, particularly in the *K* band.

8. THE MLR

We plot all 47 stars with their masses, $\mathcal{M}$, and absolute magnitudes, M_V, from Tables 10 and 11 on the *V*- and *K*-band MLR shown in Figures 21 and 22. For the MLR at *K*, only the GJ 54 AB system is missing, lacking individual M_K values. The object identifications in bold denote new or improved absolute magnitudes and masses derived for this paper using the *HST*/ FGS and RV data presented here. The primaries are plotted in blue; the secondaries are in red.

Table 12
MLR Fits and Residuals[a]

Param	M_V	M_K
y_0	−2.59	−11.41
A_1	4.77	1.64
τ_1	0.03	0.05
A_2	16.98	19.81
τ_2	1.38	3.10
x_0	0.076	0.076
rms[b] M	0.19	0.09
rms[b] $\mathcal{M}_\odot$	0.023	0.014
χ^2	1331	384
dof[c]	42	40

Notes.
[a] Parameters in the Equation (10) double exponential.
[b] rms of absolute magnitude, M, and mass, $\mathcal{M}$, residuals.
[c] dof: degrees of freedom for each fit.

With the caveat that we are mixing stars of various ages, metallicities, and magnetic properties, we fit the *V* and *K* mass–absolute magnitude distribution with a double exponent (with
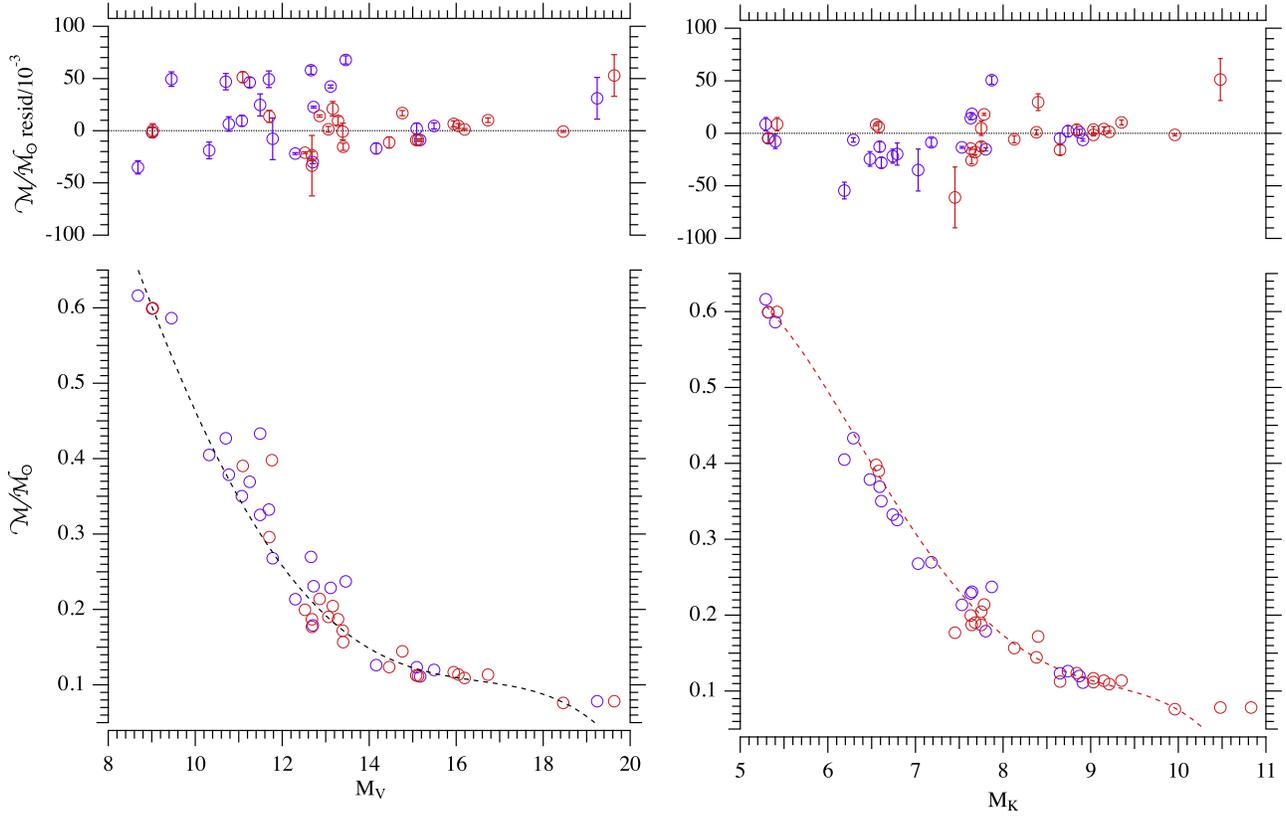
Figure 23. V- and K-band luminosity–mass relations. The dashed lines are fifth-order polynomial function fits (Equation (11)) to masses and absolute magnitudes. Primaries are in blue; secondaries are in red. Residuals are tagged with mass errors from Tables 10 and 11. We list fit coefficients in Table 13. The relations lose predictive utility for $M_V > 19$ and $M_K > 10$.

Table 13
Polynomial Fits for Mass as a Function of Absolute Magnitude[a]

Param	M_V	M_K
C0	0.19226 ± 0.000424	0.2311 ± 0.0004
C1	$-0.050737\ 0.000582$	$-0.1352\ 0.0007$
C2	$0.010137\ 0.00021$	$0.0400\ 0.0005$
C3	$-0.00075399\ 4.57\text{e}{-}05$	$0.0038\ 0.0002$
C4	$-1.9858\text{e}{-}05\ 1.09\text{e}{-}05$	$-0.0032\ 0.0001$
x_0	13.0	7.5

Note.
[a] Parameters in the Equation (11) polynomial.

offset) to provide an empirical MLR for the full range of M dwarf masses from $0.6\,\mathcal{M}_\odot$ to the end of the stellar main sequence at $0.08\,\mathcal{M}_\odot$. The form of the fitted equation is

$$M_V = y_0 + A_1 \exp\left\{\frac{-(\mathcal{M} - x_0)}{\tau_1}\right\}$$
$$+ A_2 \exp\left\{\frac{-(\mathcal{M} - x_0)}{\tau_2}\right\} \quad (10)$$

where the coefficients are in Table 12.

This function serves as a smoothing tool. We chose the double exponent because it yielded a lower χ^2 and smaller rms residuals than, for example, a single exponential with offset (χ^2 10 times larger, rms residuals four times larger). Because both absolute magnitudes and masses have errors, we fit

Equation (10) to the points using GaussFit (Jefferys et al. 1988), a modeling tool that fairly assesses errors in both variable sets. The top panels of Figures 21 and 22 display residuals to the fit for both absolute magnitude (M_V and M_K) and mass. The rms values are 0.19 mag in M_V and 0.023 $\mathcal{M}_\odot$ in mass. The rms values to the fit are 0.09 mag in M_K and 0.014 $\mathcal{M}_\odot$ in mass for the MLR at K. The coefficients for the MLR at K are also given in Table 12, along with the rms values for both MLRs.

Rather than knowing the mass of an object and needing to derive its luminosity, astronomers more typically want to estimate a mass from an absolute magnitude. Therefore, in the two panels of Figure 23 we plot mass against M_V and M_K and provide a method to estimate a mass given an absolute magnitude in a fundamental band at either optical or near-infrared wavelengths. Fit with fifth-order polynomials with magnitude offsets, x_0, we obtain expressions that can be used to estimate masses, $\mathcal{M}$, as functions of M_V or M_K (for $M_V \leqslant 19$, $M_K \leqslant 10$):

$$\mathcal{M} = C_0 + C_1(M_V - x_0) + C_2(M_V - x_0)^2$$
$$+ C_3(M_V - x_0)^3 + C_4(M_V - x_0)^4 \quad (11)$$

where V can be replaced with K. Table 13 contains coefficient and offset values for the M_V and M_K relations. As examples, a measured $M_V = 14$ would yield $\mathcal{M} = 0.15 \pm 0.03\,\mathcal{M}_\odot$, while $M_K = 9$ would yield $\mathcal{M} = 0.12 \pm 0.02\,\mathcal{M}_\odot$, where the errors are simply the rms scatter about the polynomial fits.

In Figure 24 we compare the V- and K-band MLRs with recent models from Baraffe et al. (2015) and Dotter (2016). Note that
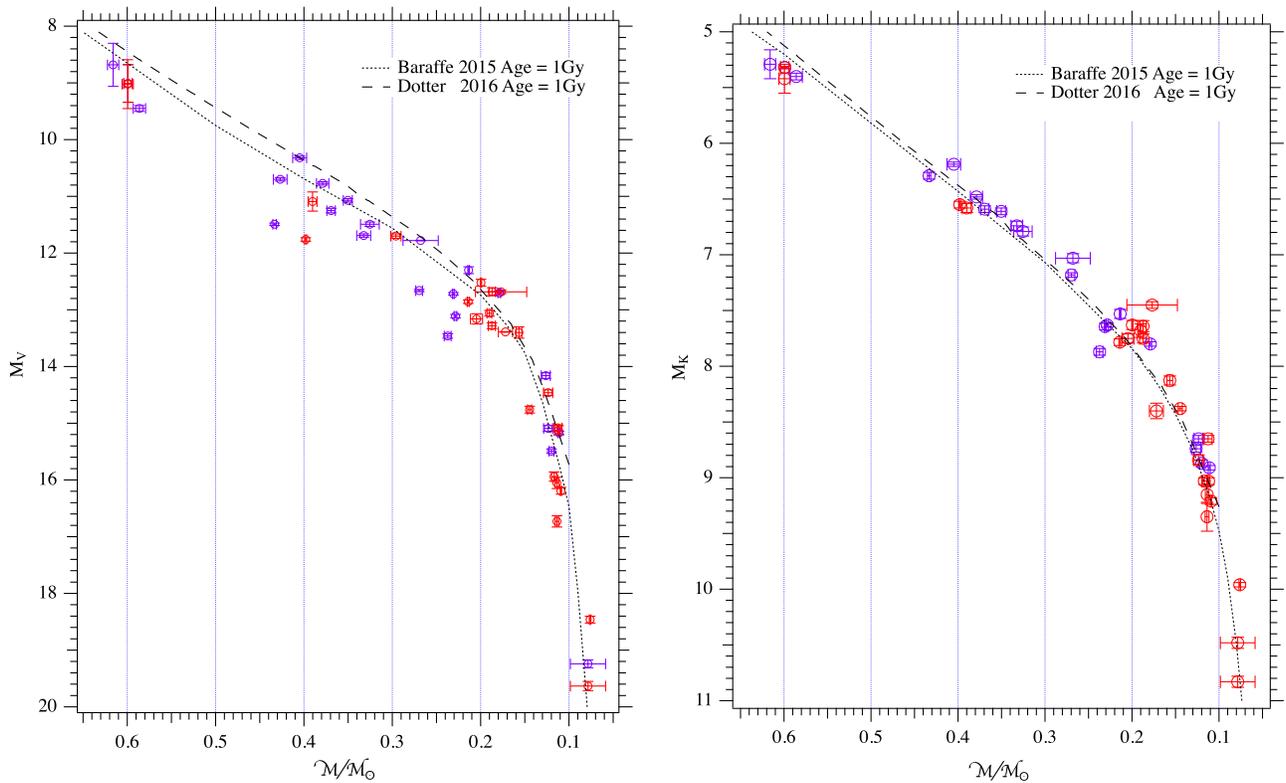
Figure 24. V- and K-band mass–luminosity relations from Baraffe et al. (2015) and Dotter (2016) along with actual measured absolute magnitudes and masses. Primaries are in blue; secondaries are in red. Models agree in some mass ranges better than in others, with K-band models having the overall best agreement.

the models agree with the K-band MLR better than with the V-band MLR. Thus, the K-band fluxes are modeled better than the V-band fluxes, which show twice the residual offsets to the Equation (10) fits. These results confirm and extend the results of Henry & McCarthy (1993) and Delfosse et al. (2000). We shall return to the larger V-band scatter in Section 9. These MLRs are the most robust ever established for M dwarfs, yet they could be improved with additional mass measurements around $\sim 0.5\,\mathcal{M}_\odot$, $\sim 0.3\;\mathcal{M}_\odot$, and below $\sim 0.1\,\mathcal{M}_\odot$.

9. DISCUSSION

Why is the scatter in the V-band MLR twice that of the corresponding K-band MLR? To reiterate, age, chemical composition, and magnetic properties can all affect the luminosities and temperatures of stars, as well as rotation, mixing length, and other properties. Here we address the first three properties.

Age attributes are particularly complicated because the MLR at low masses is a mapping that is complicated by both relative age and absolute age. Regarding relative age, once formed, M stars descend slowly to the main sequence along a nearly vertical Hayashi track (Palla 2012), so young stars have higher luminosities than stars on the main sequence. In fact, because, in the age of the universe, none of the low-mass stars investigated here have left the main sequence through evolution, the 24 systems in this sample are a heterogeneous mix of stars with ages potentially spanning ~ 10 Gyr, although for a roughly uniform star-formation rate, only a few percent might lie above the main sequence. Determining the age of an M dwarf is notoriously difficult and usually based on circumstantial evidence such as X-ray emission and flare rates, unless it is associated with a more massive star of known age (e.g., Mamajek et al. 2013) or a

particular cluster or moving group (e.g., Riedel et al. 2011). As for absolute age, an M star's luminosity is affected by its composition (metallicity), which is a function of birth date within the Galaxy. More metal-rich M dwarfs, generally formed later in the history of the Galaxy, can appear fainter due to line blocking. Absolute ages might be established through gyrochronology; see, for example, Cargile et al. (2014) and Meibom et al. (2015). A more rapidly rotating M dwarf would presumably be younger than one rotating more slowly, although a reliable relation for M dwarfs remains elusive.

Chemical composition (metallicity) is, in principle, a more directly measurable quantity than age. In the past, accurate M dwarf metallicities were difficult to quantify. Relative metallicities could be inferred from single project efforts (Bean 2007; Jenkins et al. 2009) despite their lack of agreement, and such comparisons clearly indicated that some stars possess fewer metals than others. For M dwarfs observed at optical wavelengths, the CaH bands are typically used, although these features are confounded by the interplay of effects due to both metallicity and gravity (Jao et al. 2008). There has been considerable work on M dwarf metallicities in recent years (Önehag et al. 2012; Rojas-Ayala et al. 2012; Terrien et al. 2012; Mann et al. 2014, 2015; Neves et al. 2014; Lindgren & Heiter 2015; Newton et al. 2015). While there are subtle effects that remain challenging (including the effect of low log g for young M dwarfs that have not yet contracted to their main-sequence radii), the broad consistency in most of this work suggests that accurate metallicities (perhaps at least as accurate as ± 0.1 dex) are no longer out of reach.

Magnetic properties are generally explored via measurements of chromospheric activity (flaring, X-ray emission, spots) and are correlated with rapid rotation (Wright et al. 2011; Stelzer et al.

Table 14
Factors Potentially Influencing Deviations from MLR

ID	[Fe/H]	$V \sin i$ (km s^{-1})	$R/R_\odot$	$\log(L_X/L_{\mathrm{bol}})$	Refs[a]
GJ 1005 AB	−0.47	<3	0.23	−4.97	G14, S13, F13
GJ 22 AC	−0.28	…	0.47	…	NC15, R12, P01
GJ 54 AB	…	…	0.37	−4.78	G14, S13
GJ 65 A	−0.42	32	0.165	…	K12, G05, J09, K16
GJ 65 B	…	30	0.159	…	G05, J09, K16
GJ 1081 AB	…	…	0.4	…	G14
GJ 234 AB	0.18	6	0.26	−3.65	NC15, G05, P01, S13
G 250-029 AB	…	…	0.35	…	G14
G 193-027 AB	−0.46	4.7	…	−3.67	R12, J09, S13
GJ 469 AB	0.14	…	0.38	…	G14, P01
GJ 473 AB	0.10	…	…	−3.27	NC15, S13
GJ 623 AB	−0.24	1	0.42	−4.97	NB14, G05, P01, S13
GJ 748 AB	−0.04	4.6	0.40	…	J09, P01
GJ 1245 AC	−0.04	22.5	…	−3.30	NC15, J09, S13
GJ 791.2 AB	0.07	32	…	−3.1	NC15, J09, S13
GJ 831 AB	0.3	10	0.3	−3.52	T15, G05, P01, S13
GJ 166 C	−0.17	5	…	−3.36	NC15, J09, W11
GJ 278 C	0.1	36.4	0.62	…	F13, T10, P01
GJ 278 D	0.1	37.8	0.62	…	F13, T10
GU Boo A	…	65	0.627	…	T10
GU Boo B	…	58	0.624	…	T10
GJ 570 BC	0.1[b]	2.9	0.59	−5.40	E13, J09, P01, S13
GJ 630.1 A	−0.53	9.5	0.253	…	NC15, T10
GJ 630.1 B	…	10	0.24	…	T10
GJ 747 AB	−0.19	…	0.31	−4.34	NC15, G14, S13
GJ 860 A	−0.04	<3	…	…	NC15, J09
GJ 860 B	0.03	4.7	0.32	−4.33	NB14, J09, G14, W11
GJ 2005 ABC	…	9	…	…	J09
GJ 2069 ACE	0.19	6.5	0.29	…	T15, J09, G14

Note.

[a] F13—Feiden & Chaboyer (2013), G05—Glebocki & Gnacinski (2005), I11—Irwin et al. (2011), J09—Jenkins et al. (2009), NB14—Neves et al. (2014), NC15—Newton et al. (2015), P01—Pasinetti Fracassini et al. (2001), R12—Rojas-Ayala et al. (2012), E13—Eiroa et al. (2013), S13—Stelzer et al. (2013), W11—Wright et al. (2011), T15—Terrien et al. (2015), G14—Gaidos et al. (2014), K12—Koleva & Vazdekis (2012), K16—Kervella et al. (2016).

[b] Assumes same [Fe/H] as GJ 570 A, a K5V star.

2013), attributes that are all typically seen in young M dwarfs. Photometric studies of M dwarfs at various timescales have shown that these small stars exhibit wide ranges in variability. For periods of minutes to hours, some stars flare often (Kowalski et al. 2013), while others are quiescent for long periods of time (Jao et al. 2011). Spots on the surfaces of M dwarfs reveal the presence of magnetic fields and can be used to measure rotation periods of days to months (Benedict et al. 1998; Irwin et al. 2011). Recent work has shown that, like the Sun, M dwarfs also undergo long-period photometric changes lasting several years, presumably connected to magnetic cycles in the stars (Hosey et al. 2015). Variations in magnitude could change a derived absolute magnitude, adding scatter to the MLR.

The formal errors in Table 10 effectively eliminate mass and absolute-magnitude errors as explanations for the offsets of most of the stars in the MLRs, although errors in luminosity may be invoked for GU Boo A and B, as well as errors in mass for GJ 166 C and GJ 860 A. Some combination of the three factors outlined above can explain the remaining scatter we see in Figures 21 and 22. Table 14 collects the presently available metallicity, rotation velocity, radius, and X-ray emission information for the systems considered in this paper. Here we attempt to explain a few of the significant departures in the V- and K-band MLR using these data.

The components of GJ 1005 are elevated above the MLR at V. The [Fe/H] = −0.47 value for this system is among the lowest in the sample, as are the rotation velocity and X-ray flux. This system is likely older than most others in the sample, but absorption that affects the V band is muted in K, so the components fall on the infrared MLR.

Similar to GJ 1005, both components of G 193-027 are elevated above the MLR at V. The [Fe/H] = −0.46 value is virtually identical to GJ 1005, although G 193-027's rotation velocity and X-ray luminosity fall in the middle of the sample distribution. We suspect that this is a mildly metal-poor system, again causing it to be elevated in the MLR at V but not at K.

Both components of GJ 791.2 lie below the MLRs. The stars exhibit rapid rotation and relatively large X-ray emission compared to the other stars in the sample, which suggest relative youth. This, in turn, suggests that they are metal-rich and consequently have lower than expected luminosities.

Both components of GJ 831 lie below the MLR at V, yet fall squarely on the MLR at K. This is the most metal-rich [Fe/H] = +0.3 measurement available for the 24 systems, which may reduce the flux at V but not at K and lead to the seemingly discordant locations on the two MLRs.

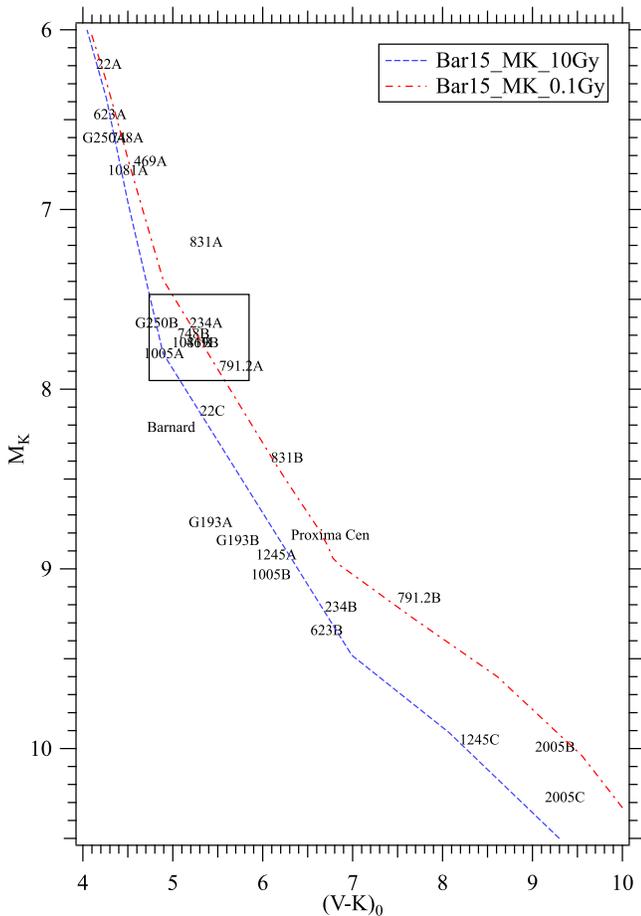The GJ 1245 ABC triple is in the original Kepler FOV, and both the AC and B components have been found to rotate

Figure 25. M_K $(V - K)_0$ Hertzsprung–Russell diagram for all systems with K magnitudes (Tables 10, 11). We derive absolute magnitudes from *HST* parallaxes (Table 7). Also plotted are stellar models for 0.1 and 10 Gy from Baraffe et al. (2015) and the single M dwarfs Proxima Cen and Barnard's star. The box contains a clump consisting of GJ 234 A, G 250-029 B, GJ 748 B, GJ 469 B, GJ 1081 B, GJ 791.2 A, and GJ 1005 A. An age spread can explain some of the scatter. As expected, most components lie close to the same age track.

rapidly and exhibit significant X-ray emission (Lurie et al. 2015). X-ray emission is an age proxy. Youth can be correlated with metallicity, which can affect absolute magnitude. In contrast to GJ 791.2, the puzzle is that neither A nor C strays far from the MLR at V or K. We note that at the very lowest masses in the MLRs presented there are very few points with empirically determined masses to constrain the fits.

Two remaining systems worthy of note are GJ 747 and G 250-029. All four components in these systems are elevated in the MLR at V. There is nothing unusual about the available data for GJ 747, while G 250-029 lacks (Table 14) any additional knowledge to which we might appeal for explanation.

The eclipsing system GJ 2069 yielded (Ribas 2003) an extremely high mass precision, but the absolute magnitudes would place these components about 0.5 mag below the MLR smoothing functions in M_V. The system has one of the highest metallicities in Table 14, perhaps partially explaining this deviation. Given that the Figure 21 smoothing fits depend on the measured mass and luminosity errors, we chose to exclude this system from the V-band fitting.

Turning the question about scatter in the MLRs around, one might ask why both components of the GJ 65 system, which have high rotational $v \sin i$, perhaps indicative of youth (and

presumably higher metallicity), are not farther from other objects with similar masses on any MLR? Clearly, work remains to be done to understand the complex interplay of the effects that set locations on the MLRs.

Ultimately, the predictive utility of an MLR depends on the scatter about any smoothing function. In the absence of physically based corrections to absolute magnitude, even the lower-scatter K-band MLR (Figure 22) exhibits deviations about the smoothing function that at some mass levels exceeds 15%. For example, at $M_K = 7.8$ the scatter is ± 0.035 $\mathcal{M}_\odot$, or 18% at the corresponding mass location of $\mathcal{M} = 0.2$ $\mathcal{M}_\odot$. This particular mass region, exhibiting the highest scatter, may signal the onset of full convection (see Houdebine & Mullan 2015).

Finally, Figure 25 presents an M_K versus $(V - K)$ HR diagram for all systems with ΔK measurements (Table 10) and masses determined using FGS data. We derive absolute magnitudes using our relatively precise *HST* parallaxes (Table 7). Also plotted are stellar models for 0.1 and 10 Gy from Baraffe et al. (2015) and the single M dwarfs Proxima Centauri and Barnard's star, using *HST* parallaxes from Benedict et al. (1999) to derive absolute magnitudes. As expected, the presumably co-eval components in systems usually lie close to the same age track. We note that the components of GJ 791.2 lie close to the Baraffe et al. (2015) 0.1 Gyr model, supporting a young age. Note also that GJ 1245 A and C lie close to the 10 Gyr model trace, even though their rapid rotation and X-ray flux (Table 14) suggest youth. Late-type stars like GJ 1245 AC can remain active on a timescale of $\sim$8 Gyr (see West et al. 2008), so it is perhaps not surprising that the stars might be quite old but still active. Apparently, this particular bandpass HR diagram is not an infallible indicator of youth, nor are the adopted markers for youth foolproof.

10. CONCLUSIONS

1. With *HST* FGS we obtained fringe tracking (POS) observations with either FGS 3 or FGS 1r of 13 low-mass binary systems, each with 6–16 epochs of observations typically spanning 5 years. These yielded absolute parallaxes with an external error better than 1% and proper motions with average errors of 0.3 mas yr^{-1} in R.A. and decl.

2. Fringe tracking (POS) observations of the primary, including photocenter corrections where required, provide a perturbation orbit.

3. Fringe scans (TRANS) combined with POS observations provide a mass fraction relative to an astrometric reference frame. TRANS observations also provide ΔV measurements (Henry et al. 1999). For two systems we acquired only TRANS measurements, requiring external determinations of the mass fractions.

4. RVs, primarily from the McDonald Observatory 2.1 m telescope and Cassegrain Echelle spectrograph, were combined with astrometry for seven systems, increasing the accuracy of their final mass results.

5. We derive 30 component masses in 15 binary red dwarf systems with a median precision 1.8% and an average precision of 2.1%. These are the first mass determinations for 12 stars in six systems. These masses are augmented with additional red dwarfs with high-quality masses in nine additional systems.

6. We provide system magnitudes at *UBVRIJHK* and component magnitude differences, ΔV and ΔK, many

reported for the first time here. New trigonometric parallaxes from both *HST* and the RECONS astrometry program at CTIO, as well as literature values, are used with the photometry to obtain accurate component M_V and M_K values.

7. This study provides high-quality data for 47 red dwarfs with masses between 0.616 $\mathcal{M}_\odot$ and 0.076 $\mathcal{M}_\odot$, M_V = 8.68–19.63, and M_K = 5.29–10.27. Many of the secondaries lie below 0.2 $\mathcal{M}_\odot$, the crucial region where age begins to play a significant role in the luminosities of stars. With these data, we establish MLRs in both the optical *V* and near-infrared *K* bands.

8. The *V* and *K* MLRs are fit with double exponentials to provide empirical conversions of masses to absolute magnitudes, and vice versa. We find that the *K*-band MLR exhibits a scatter in mass half that of the corresponding *V*-band relation.

9. The predictive capability of even the smaller-scatter *K*-band MLR appears to be limited by age, composition, and magnetic differences between low-mass stars. At M_K = 7.8 the scatter is 0.035 $\mathcal{M}_\odot$, or 18% at the corresponding mass location of $\mathcal{M} = 0.2\,\mathcal{M}_\odot$.

10. Future work will disentangle the effects of age, metallicity, and magnetic properties on luminosity and enable us to construct MLRs that consider additional factors that affect low-mass stars.

REFERENCES

Allard, F., Hauschildt, P. H., & Schweitzer, A. 2000, ApJ, 539, 366
Andersen, J. 1991, A&ARv, 3, 91
Balega, I. I., Balega, Y. Y., Belkin, I. N., et al. 1994, A&AS, 105, 503
Baraffe, I., Homeier, D., Allard, F., et al. 2015, A&A, 577, A42
Barbieri, C., De Marchi, G., Nota, A., et al. 1996, A&A, 315, 418
Bean, J. L. 2007, PhD thesis, Univ. Texas
Benedict, G. F., McArthur, B., Chappell, D. W., et al. 1999, AJ, 118, 1086
Benedict, G. F., McArthur, B., Nelan, E. P., et al. 1998, Proc. SPIE, 3350, 229
Benedict, G. F., McArthur, B. E., Feast, M. W., et al. 2007, AJ, 133, 1810
Benedict, G. F., McArthur, B. E., Feast, M. W., et al. 2011, AJ, 142, 187
Benedict, G. F., McArthur, B. E., Franz, O. G., et al. 2000, AJ, 120, 1106
Benedict, G. F., McArthur, B. E., Franz, O. G., et al. 2001, AJ, 121, 1607
Benedict, G. F., McArthur, B. E., Napiwotzki, R., et al. 2009, AJ, 138, 1969
Benedict, G. F., Tanner, A. M., Cargile, P. A., et al. 2014, AJ, 148, 108
Bessell, M. S. 1990, PASP, 102, 1181
Beuzit, J. L., Ségransan, D., Forveille, T., et al. 2004, A&A, 425, 997
Blazit, A., Bonneau, D., & Foy, R. 1987, A&AS, 71, 57
Cargile, P. A., James, D. J., Pepper, J., et al. 2014, ApJ, 782, 29
Coppenbarger, D. S., Henry, T. J., & McCarthy, D. W., Jr. 1994, AJ, 107, 1551
Costa, E., Méndez, R. A., Jao, W. C., et al. 2005, AJ, 130, 337
Cox, A. N. 2000, Allen's Astrophysical Quantities (New York: AIP Press)
Dahn, C. C., Harrington, R. S., Kallarakal, V. V., et al. 1988, AJ, 95, 237
Dahn, C. C., Harrington, R. S., Riepe, B. Y., et al. 1982, AJ, 87, 419
Delfosse, X., Forveille, T., Mayor, M., et al. 1999, A&A, 341, L63
Delfosse, X., Forveille, T., Perrier, C., et al. 1998, A&A, 331, 581
Delfosse, X., Forveille, T., Ségransan, D., et al. 2000, A&A, 364, 217
Dieterich, S. B., Henry, T. J., Golimowski, D. A., et al. 2012, AJ, 144, 64
Dieterich, S. B., Henry, T. J., Jao, W. C., et al. 2014, AJ, 147, 94
Dotter, A. 2016, ApJS, 222, 8
Eiroa, C., Marshall, J. P., Mora, A., et al. 2013, A&A, 555, A11
Endl, M., Cochran, W. D., Kürster, M., et al. 2006, ApJ, 649, 436
Feiden, G. A., & Chaboyer, B. 2013, ApJ, 779, 183
Forveille, T., Beuzit, J. L., Delfosse, X., et al. 1999, A&A, 351, 619
Franz, O. G., Henry, T. J., Wasserman, L. H., et al. 1998, AJ, 116, 1432
Franz, O. G., Kreidl, T. J. N., Wasserman, L. W., et al. 1991, ApJL, 377, L17
Gaidos, E., Mann, A. W., Lépine, S., et al. 2014, MNRAS, 443, 2561
Geyer, D. W., Harrington, R. S., & Worley, C. E. 1988, AJ, 95, 1841
Glebocki, R., & Gnacinski, P. 2005, yCat, 3244, 0
Golimowski, D. A., Henry, T. J., Krist, J. E., et al. 2004, AJ, 128, 1733
Gould, A. 2004, arXiv:astro-ph/0403506
Gould, A., & Morgan, C. W. 2003, ApJ, 585, 1056
Hanson, R. B. 1979, MNRAS, 186, 875
Harrison, T. E., McNamara, B. J., Szkody, P., et al. 1999, ApJL, 515, L93
Henry, T. J., Franz, O. G., Wasserman, L. H., et al. 1999, ApJ, 512, 864
Henry, T. J., Jao, W. C., Subasavage, J. P., et al. 2006, AJ, 132, 2360
Henry, T. J., & McCarthy, D. W., Jr. 1993, AJ, 106, 773
Henry, T. J., McCarthy, D. W., Jr., Freeman, J., et al. 1992, AJ, 103, 1369
Hershey, J. L. 1973, AJ, 78, 935
Hershey, J. L., & Taff, L. G. 1998, AJ, 116, 1440
Holberg, J. B., Oswalt, T. D., & Barstow, M. A. 2012, AJ, 143, 68
Horch, E. P., Bahi, L. A. P., Gaulin, J. R., et al. 2012, AJ, 143, 10
Hosey, A. D., Henry, T. J., Jao, W. C., et al. 2015, AJ, 150, 6
Houdebine, E. R., & Mullan, D. J. 2015, ApJ, 801, 106
Irwin, J., Berta, Z. K., Burke, C. J., et al. 2011, ApJ, 727, 56
Jao, W. C., Henry, T. J., Beaulieu, T. D., et al. 2008, AJ, 136, 840
Jao, W. C., Henry, T. J., Subasavage, J. P., et al. 2011, AJ, 141, 117
Jefferys, W. H., Fitzpatrick, M. J., & McArthur, B. E. 1988, CeMec, 41, 39
Jenkins, J. S., Ramsey, L. W., Jones, H. R. A., et al. 2009, ApJ, 704, 975
Kervella, P., Mérand, A., Ledoux, C., et al. 2016, arXiv:1607.04351
Khrutskaya, E. V., Izmailov, I. S., & Khovrichev, M. Y. 2010, AstL, 36, 576
Kilkenny, D., Koen, C., van Wyk, F., et al. 2007, MNRAS, 380, 1261
Koen, C., Kilkenny, D., van Wyk, F., et al. 2010, MNRAS, 403, 1949
Köhler, R., Ratzka, T., & Leinert, C. 2012, A&A, 541, A29
Koleva, M., & Vazdekis, A. 2012, A&A, 538, A143
Kowalski, A. F., Hawley, S. L., Wisniewski, J. P., et al. 2013, ApJS, 207, 15
Leinert, C., Allard, F., Richichi, A., et al. 2000, A&A, 353, 691
Leinert, C., Weitzel, N., Richichi, A., et al. 1994, A&A, 291, L47
Lindgren, S., & Heiter, U. 2015, in AAS/Division for Extreme Solar Systems Abstracts 3, 115.04

López-Morales, M., & Ribas, I. 2005, ApJ, 631, 1120
Lurie, J. C., Davenport, J. R. A., Hawley, S. L., et al. 2015, ApJ, 800, 95
Lurie, J. C., Henry, T. J., Jao, W. C., et al. 2014, AJ, 148, 91
Lutz, T. E., & Kelker, D. H. 1973, PASP, 85, 573
Mamajek, E. E., Bartlett, J. L., Seifahrt, A., et al. 2013, AJ, 146, 154
Mann, A. W., Deacon, N. R., Gaidos, E., et al. 2014, AJ, 147, 160
Mann, A. W., Feiden, G. A., Gaidos, E., et al. 2015, ApJ, 804, 64
Marcy, G. W., & Benitz, K. J. 1989, ApJ, 344, 441
Martinache, F., Lloyd, J. P., Ireland, M. J., et al. 2007, ApJ, 661, 496
McArthur, B., Benedict, G. F., Jefferys, W. H., et al. 2002, in The 2002 HST
    Calibration Workshop: Hubble after the Installation of the ACS and the
    NICMOS Cooling System, ed. S. Arribas, A. Koekemoer, & B. Whitmore
    373
McArthur, B. E., Benedict, G. F., Harrison, T. E., et al. 2011, AJ, 141, 172
McArthur, B. E., Benedict, G. F., Jefferys, W. J., et al. 2006, in The 2005 HST
    Calibration Workshop: Hubble After the Transition to Two-Gyro Mode, ed.
    A. M. Koekemoer, P. Goudfrooij, & L. L. Dressel 396
McCarthy, D. W., Jr., & Henry, T. J. 1987, ApJ, 319, 93
McCarthy, D. W., Jr., Henry, T. J., Fleming, T. A., et al. 1988, ApJ, 333, 943
McCarthy, D. W., Jr., Henry, T. J., McLeod, B., et al. 1991, AJ, 101, 214
McCarthy, J. K., Sandiford, B. A., Boyd, D., et al. 1993, PASP, 105, 881
Meibom, S., Barnes, S. A., Platais, I., et al. 2015, Natur, 517, 589
Morales, J. C., Ribas, I., Jordi, C., et al. 2009, ApJ, 691, 1400
Nelan, E. e. 2012, Fine Guidance Sensor Instrument Handbook for Cycle 21
    v.20.0 (Baltimore, MD: STScI)
Neves, V., Bonfils, X., Santos, N. C., et al. 2014, A&A, 568, A121
Newton, E. R., Charbonneau, D., Irwin, J., et al. 2015, ApJ, 800, 85
Önehag, A., Heiter, U., Gustafsson, B., et al. 2012, A&A, 542, A33
Palla, F. 2012, in AIP Conf. Ser. 1480, ed. M. Umemura & K. Omukai
    (Melville, NY: AIP), 22
Pasinetti Fracassini, L. E., Pastori, L., Covino, S., et al. 2001, A&A, 367, 521
Perryman, M. A. C., Lindegren, L., Kovalevsky, J., et al. 1997, A&A, 323, L49
Pourbaix, D., & Jorissen, A. 2000, A&AS, 145, 161
Pourbaix, D., Platais, I., Detournay, S., et al. 2003, A&A, 399, 1167
Probst, R. G. 1977, AJ, 82, 656
Ribas, I. 2003, A&A, 398, 239
Riedel, A. R., Finch, C. T., Henry, T. J., et al. 2014, AJ, 147, 85

Riedel, A. R., Murphy, S. J., Henry, T. J., et al. 2011, AJ, 142, 104
Roeser, S., Demleitner, M., & Schilbach, E. 2010, AJ, 139, 2440
Rojas-Ayala, B., Covey, K. R., Muirhead, P. S., et al. 2012, ApJ, 748, 93
Schlafly, E. F., & Finkbeiner, D. P. 2011, ApJ, 737, 103
Schroeder, D. J., Golimowski, D. A., Brukardt, R. A., et al. 2000, AJ, 119, 906
Schultz, A. B., Hart, H. M., Hershey, J. L., et al. 1998, PASP, 110, 31
Ségransan, D., Delfosse, X., Forveille, T., et al. 2000, A&A, 364, 665
Seifahrt, A., Röll, T., Neuhäuser, R., et al. 2008, A&A, 484, 429
Skrutskie, M. F., Cutri, R. M., Stiening, R., et al. 2006, AJ, 131, 1163
Sneden, C., Lawler, J. E., & Cowan, J. J. 2002, PhST, 100, 15
Standish, E. M., Jr. 1990, A&A, 233, 252
Stelzer, B., Marino, A., Micela, G., et al. 2013, MNRAS, 431, 2063
Stromberg, G. 1939, ApJ, 89, 10
Tamazian, V. S., Docobo, J. A., Melikian, N. D., et al. 2006, PASP, 118,
    814
Terrien, R. C., Fleming, S. W., Mahadevan, S., et al. 2012, ApJL, 760, L9
Terrien, R. C., Mahadevan, S., Deshpande, R., et al. 2015, ApJS, 220, 16
Tody, D. 1993, in ASP Conf. Ser. 52, Astronomical Data Analysis Software
    and Systems II, ed. R. J. Hanisch, R. J. V. Brissenden, & J. Barnes (San
    Francisco, CA: ASP), 173
Torres, G., Andersen, J., & Giménez, A. 2010, A&ARv, 18, 67
Torres, G., Henry, T. J., Franz, O. G., et al. 1999, AJ, 117, 562
Torres, G., & Ribas, I. 2002, ApJ, 567, 1140
van Altena, W. F., Lee, J. T., & Hoffleit, E. D. 1995, The General Catalogue of
    Trigonometric [Stellar] Parallaxes (4th ed.; New Haven, CT: Yale
    University Observatory) (YPC95)
van de Kamp, P. 1967, Principles of Astrometry (San Francisco: Freeman)
van Leeuwen, F. 2007, Hipparcos, the New Reduction of the Raw Data, Vol.
    350 (Berlin: Springer)
van Leeuwen, F., Feast, M. W., Whitelock, P. A., et al. 2007, MNRAS,
    379, 723
Weis, E. W. 1984, ApJS, 55, 289
Weis, E. W. 1996, AJ, 112, 2300
West, A. A., Hawley, S. L., Bochanski, J. J., et al. 2008, AJ, 135, 785
Winters, J. G., Henry, T. J., Lurie, J. C., et al. 2015, AJ, 149, 5
Woitas, J., Tamazian, V. S., Docobo, J. A., et al. 2003, A&A, 406, 293
Wright, N. J., Drake, J. J., Mamajek, E. E., et al. 2011, ApJ, 743, 48